DOCTORAL THESIS

Population and evolutionary dynamics in spatial systems.

Daniel Rodríguez Amor

2013

PROGRAMA DE DOCTORAT EN CIÈNCIES EXPERIMENTALS I SOSTENIBILITAT

Supervisor:
Joaquim Fort Viader

This memory has been presented to obtain the degree of international doctor by the Universitat de Girona

This Ph.D. thesis has been prepared as a collection of papers, in agreement with the regulations of the University of Girona. This thesis includes three original papers that have been published in a peer-reviewed journal, and a paper that has not been yet published at the moment of preparing this thesis. The four papers have been published in (or submitted to) journals with impact factors within the first quartile, according to the 2011 Journal Citation Reports (JCR), for the subject category *Physics, Mathematical*.

The complete references of the papers comprised in this thesis and the impact factor of the journals are

Amor, D. R. & Fort, J. 2009 Fronts from two-dimensional dispersal kernels: Beyond the nonoverlapping-generations model. *Phys. Rev. E* 80, 051918. (Impact Factor 2.26, journal 6 of 55, Quartile 1, category *Physics, Mathematical*)

Amor, D. R. & Fort, J. 2010 Virus infection speeds: Theory versus experiment. *Phys. Rev. E* 82, 061905. (Impact Factor 2.26, journal 6 of 55, Quartile 1, category *Physics, Mathematical*)

Amor, D. R. & Fort, J. 2011 Effects of punishment in a mobile population playing the prisoner's dilemma game. *Phys. Rev. E* 84, 066115. (Impact Factor 2.26, journal 6 of 55, Quartile 1, category *Physics, Mathematical*)

Amor, D. R. & Fort, J. 2013 Lag-driven motion in front propagation. *J Stat Mech - Theor Exp* Submitted. (Impact Factor 2.00, journal 13 of 55, Quartile 1, category *Physics, Mathematical*)

Abstract

Physical and mathematical models are extremely useful to understand key processes in population and evolutionary dynamics. Such models allow the study of many diverse features in spatial systems such as front propagation, the evolution of the population number density, interactions between species (or individuals), the evolution of strategies, etc. This thesis is devoted to several physical models describing spatial systems.

The first model in this thesis (chapter 4) focuses on the effects of the population structure in two-dimensional invasive fronts. An expression for the front speed is derived from the equations for structured populations. When comparing its results with the front speed of non-structured populations, the structured-population model displays more reasonable results. Moreover, the model is applied to postglacial tree recolonization fronts, for which the importance of the overlapping-generation effect is analyzed.

Reaction-diffusion equations are used in chapter 5 to describe Vesicular Stomatitis Virus infections. A several-species model is developed which describes the interactions between uninfected cells, infected cells and virus populations. Moreover, the delay time that the virus needs to reproduce inside the host cell is considered by the model. Such a delay time is shown critically important in order to predict infection speeds that agree with experimental data.

Chapter 6 derives an approximate front speed from the equations of several biophysical systems presenting lag (delay) times. Remarkably, if high reproduction rates are considered, the same approximate expression is attained for both non-structured and structured populations. The approximate speed is extremely simple, and it agrees with an approximate expression presented in chapter 5 for virus infections speeds. The approximate speed is able to explain observed spread rates of several virus species, tree species as well as the Neolithic transition.

The Prisoner's Dilemma game is used in chapter 7 to study the evolution of cooperation and defection strategies. Punishment is introduced in virtual populations as an action which follows, with a certain probability, the Prisoner's Dilemma game interactions. Furthermore, the model considers that agents undergo continuous motion, instead of jumping on the nodes of a grid. Simulations show that low doses of mobility and social punishment (i.e., the possibility for cooperators to punish those who free ride) are specially effective to enhance cooperation.

Resum

Els models físics i matemàtics són de gran utilitat a l'hora d'entendre processos clau en la dinàmica poblacional i evolutiva. Aquests models permeten l'estudi de característiques molt diverses dels sistemes espacials, com són la propagació de fronts, l'evolució de la densitat de població, les interaccions entre espècies (o individus), l'evolució d'estratègies, etc. Aquesta tesi presenta diversos models físics que descriuen sistemes espacials.

El primer model d'aquesta tesi (capítol 4) estudia els efectes de l'estructura de la població en fronts invasius bidimensionals. Una expressió per la velocitat del front és derivada de les equacions per a poblacions estructurades. Quan es comparen els seus resultats amb la velocitat de fronts de poblacions no estructurades, el model de poblacions estructurades presenta resultats més raonables. A més, el model s'aplica a fronts arboris de recolonitzacions postglacials, en el marc dels quals s'analitza la importància de les generacions solapades d'arbres.

Al capítol 5 s'utilitzen equacions de reacció-difusió per descriure infeccions del Vesicular Stomatitis Virus. A aquest efecte, es desenvolupa un model per a múltiples espècies que descriu les interaccions entre les poblacions de cèl·lules no infectades, cèl·lules infectades i virus. A més, el temps de retard que el virus requereix per reproduir-se a dins de la cèl·lula hoste és considerat pel model. S'observa que aquest temps de retard té una importància crítica per tal de predir velocitats d'infecció que concordin amb les dades experimentals.

Al capítol 6 es deriva una velocitat de front aproximada a partir de les equacions per diversos sistemes biofísics que presenten temps de demora (retard). Notablement, si es consideren taxes de reproducció elevades, s'obté la mateixa expressió tant a partir de l'assumpció de poblacions no estructurades com la de poblacions estructurades. La velocitat de front aproximada és extremadament simple, i coincideix amb una expressió aproximada per velocitats d'infeccions víriques al capítol 5. L'expressió aproximada és capaç d'explicar velocitats de propagació observades de diverses espècies de virus, espècies d'arbres i la transició del Neolític.

El joc del Dilema del Presoner s'utilitza al capítol 7 per estudiar l'evolució d'estratègies de cooperació i deserció. El càstig és introduït a poblacions virtuals com a una acció que segueix, amb una certa probabilitat, les interaccions del joc del Dilema del Presoner. Més encara, el model considera que els agents experimenten una mobilitat continua, en comptes de moure's sobre vèrtex d'una xarxa. Les simulacions mostren que dosis reduïdes de mobilitat i càstig social (és a dir, la possibilitat que els cooperadors castiguin als desertors) són especialment efectives per incentivar la cooperació.

Resumen

Los modelos físicos y matemáticos son de gran utilidad a la hora de entender procesos clave en la dinámica poblacional y evolutiva. Estos modelos permiten el estudio de muy diversas características de los sistemas espaciales, como son la propagación de frentes, la evolución de la densidad de población, las interacciones entre especies (o individuos), la evolución de estrategias, etc. Esta tesis presenta varios modelos físicos que describen sistemas espaciales.

El primer modelo de esta tesis (capítulo 4) estudia los efectos de la estructura de la población en frentes invasivos bidimensionales. Una expresión para la velocidad del frente es derivada de las ecuaciones para poblaciones estructuradas. Cuando se comparan sus resultados con la velocidad de frentes de poblaciones no estructuradas, el modelo de poblaciones estructuradas presenta resultados más razonables. Además, el modelo se aplica a frentes de recolonizaciones posglaciales, en el marco de los cuales se analiza la importancia de las generaciones solapadas de árboles.

En el capítulo 5 se utilizan ecuaciones de reacción-difusión para describir infecciones del Vesicular Stomatitis Virus. A este efecto, se desarrolla un modelo para múltiples especies que describe las interacciones entre las poblaciones de células no infectadas, células infectadas y virus. Además, el tiempo de retraso que el virus requiere para reproducirse dentro de la célula huésped es considerado por el modelo. Se observa que dicho tiempo de retraso tiene una importancia crítica a la hora de predecir velocidades de infección que concuerden con los datos experimentales.

En el capítulo 6 se deriva una velocidad aproximada del frente a partir de las ecuaciones para diversos sistemas biofísicos que presentan tiempo de demora (retraso). Notablemente, si se consideran tasas de reproducción elevadas, se obtiene la misma expresión tanto a partir de la conjetura de poblaciones no estructuradas como de la de poblaciones estructuradas. La velocidad aproximada del frente es extremadamente simple, y coincide con una expresión aproximada para velocidades de infecciones víricas en el capítulo 5. La expresión aproximada es capaz de explicar velocidades de propagación observadas de diversas especies de virus, especies de árboles y la transición del Neolítico.

El juego del Dilema del Prisionero se utiliza en el capítulo 7 para estudiar la evolución de estrategias de cooperación y deserción. El castigo es introducido en poblaciones virtuales como una acción que sigue, con una cierta probabilidad, a las interacciones del juego del Dilema del Prisionero. Adicionalmente, el modelo considera que los agentes experimentan una movilidad continua, en lugar de moverse sobre los vértices de una malla. Las simulaciones muestran que dosis reducidas de movilidad y castigo social (es decir, la posibilidad de que los cooperadores castiguen a los desertores) son especialmente efectivas para incentivar la cooperación.

Acknowledgements

I would like to express my deep gratitude to my supervisor, Prof. Joaquim Fort, for his confidence and support during these last five years. I owe him the discovery of the research career, in which I initially engaged quite unaware about, and that I presently find amongst the most exciting jobs.

This PhD thesis has been possible thanks to the FPU (Formación de Profesorado Universitario) fellowship program funded by the Ministerio de Educación y Ciencia (currently, Ministerio de Educación, Cultura y Deporte). I am also grateful to the European Commission Fepre project (which supported my first months of research at the University of Girona), the Generalitat project 2009-SGR-374 (which supported my last months of research at Girona), and the projects Consolider SimulPast CSD-2010-00034, FIS-2006-12296-C02-02, FIS-2009-13050 and FIS-2012-31307 funded by the Ministerio de Ciencia e Innovación (currently, Ministerio de Economía y Competitividad).

I would like thank the professors and my PhD fellows at the Physics Department for the friendly times at the University of Girona. My special gratitude to Neus (who was always a step beyond me in the PhD path) and Iós (with whom I started the path) for their willing to help at any moment.

I am sincerely grateful for the unconditional support from my charming family, specially my parents Mercedes and Miguel, my sister Raquel, my grandparents Natalia and José, uncle Albert, and my marvelous girlfriend Eva. Many thanks to the formidable freaks Rafa, Marc, David, Anna, Marta, Natalia, Ana, Imanol, Cris, Marta, Nati and Fernando. I cannot miss to acknowledge the warm company of my mate Bolt, who patiently lays close to me when I work at home.

With the Universe came Physics,
Physics led to Life,
then Life spread and brought Cooperation.
One day Cooperation shaped humans,
and ever since we try to solve this Puzzle.

Contents

List of Figures

List of Tables

Chapter 1

Introduction

This thesis is devoted to a variety of population dynamics phenomena, including ecological populations (chapter 4), microbiological ones (chapter 5), an approximate front speed for populations displaying lag-driven migrations (chapter 6) and the evolution of cooperation under dispersal (chapter 7). In all of these works, the dynamics of biological populations is studied, first focusing on the evolution of the population density (chapters 4-6) and then extending our scope to tackle the evolution of cooperation (chapter 7). Although all chapters can be potentially applied to many different biological species, for the sake of definiteness and clarity we consider specific examples, namely trees in chapter 4, viruses in chapter 5, and humans in chapter 7. Moreover, these three species are considered in the analysis of an approximate expression for the spread rate in chapter 6.

The first section in this chapter aims to provide a brief overview on previous population dynamics models, specially focusing on those works which particularly inspired the models in chapters 4-6. A second section is devoted to an introduction to the exciting, non-solved, interdisciplinary problem of cooperation, which has motivated the work in chapter 7. Finally, the last section summarizes the population dynamics models in this thesis.

1.1 Previous biological populations dynamics models

In the last century, reaction-diffusion models were applied to model many biological and cross-disciplinary complex systems [1]. One of the first remarkable works focusing on biological fronts was performed by R. A. Fisher in 1937. With the aim of modelling the wave front speed of advantageous genes, Fisher used the following simple, differential equation [2]:

$$\frac{\partial p}{\partial t} = D\frac{\partial^2 p}{\partial x^2} + mp(1-p) \tag{1.1}$$

where $p = p(x,t)$ is the frequency of the mutant gene at position x and time t, D the diffusion coefficient of the gene in the considered linear habitat, and m the intensity

of selection in favour of the mutant with respect to the standard gene [which exhibits the frequency $(1-p)$]. From the above equation (1.1) Fisher derived the front speed $c = 2\sqrt{Dm}$ (which is presently known as Fisher's speed).

Some years later, in 1951, J. G. Skellman applied the two-dimensional (2D) version of Fisher's equation to biological invasions in general [3], using $p(x, y, t)$ for a population density rather than a gene frequency. In the following decades, similar models were applied to rather different spreading systems such as human population fronts [4], viral infections [5], tumor growth [6], combustion fronts [7], superconductors [8], etc.

In 1999, Fort and Méndez published a seminal paper in which the critical importance of a delay time elapsed between successive migrations was shown in the context of front propagation [9]. With this purpose, Fort and Méndez presented the following Hyperbolic Reaction-Diffusion (HRD) equation:

$$\frac{\partial p}{\partial t} + \frac{T}{2}\frac{\partial^2 p}{\partial t^2} = D\left(\frac{\partial^2 p}{\partial x^2} + \frac{\partial^2 p}{\partial y^2}\right) + F + \frac{T}{2}\frac{\partial F}{\partial t}, \tag{1.2}$$

which contains second-order terms in order to account for the delay time T. In Eq. (1.2), F corresponds to the population growth function, and the population density is computed in two dimensions (i.e., $p = p(x, y, t)$). Note that, if no delay time is considered (i.e., $T = 0$), then the 2D version of Fisher's equation (1.1) is recovered (F would correspond to the term $mp(1-p)$ in the above case).

The original work in Ref. [9] applied the HRD equation (1.2) to the Neolithic population front. However, in more recent works the HRD equation has been used to model the spread of multiple systems, such as virus infections [10] or cancer spread [11].

The HRD equation is a differential equation that receives special attention in this thesis, since it is used to model the spread of several species in chapters 5 and 6. In addition to this equation, in the next chapters several reaction-diffusion and reaction-dispersal equations are used to describe biological populations dynamics. The following three subsections aim to introduce the biological systems (as well as the corresponding theoretical framework) we study in this thesis.

1.1.1 Postglacial tree recolonizations

The transition from the Pleistocene to the warmer Holocene series took place about $12,000$ years ago. The end of the last Ice Age was followed by global-scale plant migrations, and thus high-latitude territories were colonized by trees. However, classical models cannot explain the tree rapid spread ($10^2 - 10^3$ m/yr) estimated from the paleorecord [12]. This problem is known as the Reid's Paradox [13] in honor of Clement Reid's, who in 1899 calculated the apparently unrealistic dispersal distances that were required to predict observed postglacial recolonization speeds [14].

In 2007, J. Fort [15] developed a 2D model for tree populations based on the integrodifference equation:

$$p(x, y, t+T) = R_0 \int_{-\infty}^{+\infty}\int_{-\infty}^{+\infty} p(x+\triangle_x, y+\triangle_y, t) \\ \phi(\triangle_x, \triangle_y) d\triangle_x \, d\triangle_y, \tag{1.3}$$

where $p(x, y, t)$ stands for the tree population density per unit area, and R_0 is the net reproductive rate of seeds per parent tree and year. The dispersal kernel $\phi(\triangle_x, \triangle_y)$ is the probability per unit area that a seed falling from a parent tree at $(x+\triangle_x, y+\triangle_y, t)$ reaches the ground at $(x, y, t+T)$, where T is the time interval between two subsequent jumps. Fort's model is remarkably simple because it assumes non-overlapping generations (i.e., every tree reproduces only once and then dies). Thus, the interval time T considered in Eq. (1.3) corresponds to one generation (i.e., the mean maturation time) of the tree species. In Ref. [15], Fort showed that long-distance dispersals (see below) lead the nonoverlapping model to predict notably high spread rates.

Long-distance dispersals are the consequence of rare events (e.g., heavy storms, tornados, transport by migratory animals [16]) which can disperse seeds to distances in the range $10^3 - 10^4$m, and even farther. Although long-distance dispersals are very infrequent (they usually affect less than 1% of the seeds), they embrace notably higher distances than those considered by short dispersal kernels (i.e., the range $10^1 - 10^2$m) [16, 17]. In Ref. [15], Fort considered long-distance dispersal data (which had been recently published by Nathan et al. [18]) affecting the yellow poplar species. This led to front speed solutions which could explain the rapid tree migration at the end of the Pleistocene.

The question arises of how overlapping generations of individuals (or, more generally, the population's structure) can affect the dynamics of the population. In the context of biological invasions (such as postglacial recolonizations), it is sensible to think that individuals taking part in multiple reproduction events can directly affect the front speed. In 2000, Neubert and Caswell [19] published the first attempt to derive an expression for the invasion speed of structured populations. However, the authors considered the specific and limiting case of 1D invasions [19]. Although 1D habitats have classically been considered when studying structured populations, this case is certainly not applicable to the majority of biological invasions.

1.1.2 Virus infection fronts

The interaction between a virus and its corresponding host cell is a very relevant issue which goes beyond biological or medical interest. Indeed, from the physical perspective, the understanding of the processes governing this multiple-species system becomes an intriguing challenge. Rather surprisingly, few models have focused on the dynamics and the spread of several generations of viruses infecting a population of cells.

Focal infection experiments permit an in-deep analysis of this system in the laboratory. In focal infections, a certain concentration of virus is inoculated into a very small region ($r = 0$) in a layer of immobilized host cells. Virions are able both to diffuse in the extracellular medium and to infect the cells. When a cell is infected, the virus reproduces inside it until the cell dies, thus releasing a new progeny that will bear new infection cycles. As a result, an approximately circular region of dead cells (i.e., a plaque) is observable in focal infection experiments. Moreover, the bound of the plaque advances at an approximately constant speed which depends on specific features of the virions, the host cells and the extracellular medium, as we shall see below.

In a growing plaque, the interactions between uninfected cells, infected cells and virions can be summarized by the reactions [10, 20, 21]:

$$V + C \xrightarrow{k_1} I \xrightarrow{k_2} YV, \tag{1.4}$$

where k_1 is the adsorption rate of viruses V into uninfected cells C, k_2 is the rate constant for the death of infected cells I, and the yield Y is the number of new viruses produced per infected cell.

In 1992, Yin and McCaskill [22] proposed a reaction-diffusion model to describe the dynamics of bacteriophages (viruses that infect bacteria). The evolution of the system was governed by the reaction-diffusion equations:

$$\frac{\partial[V]}{\partial t} = D\frac{\partial^2[V]}{\partial r^2} - k_1[C][V] + Yk_2I, \tag{1.5}$$

$$\frac{\partial[C]}{\partial t} = -k_1[C][V], \tag{1.6}$$

$$\frac{\partial[I]}{\partial t} = k_1[V][C] - k_2[I], \tag{1.7}$$

where the symbols [...] denote concentration, and D is the diffusivity of the virions in the extracellular medium [1]. Note that in Eq. (1.5) the limit $r \to 0$ has been considered, so that the Laplacian is $\nabla^2[V] = \frac{\partial^2[V]}{\partial x^2} + \frac{\partial^2[V]}{\partial y^2} = \frac{\partial^2[V]}{\partial r^2} + \frac{1}{r}\frac{\partial[V]}{\partial r} \simeq \frac{\partial^2[V]}{\partial r^2}$, where we have assumed that $[V]$ depends only on r but not on the polar angle.

In 2002, Fort and Méndez [10] developed a model that improved previous works (such as the above model by Yin and McCaskill [22]), as it took into account the actual delayed diffusion affecting the virus population. Noticing that the virus spends some time into the host cell before yielding the new progeny, Fort and Méndez used the HRD equation (1.2) to describe virus spread. This leaded to predicted front speeds showing perfect agreement with experimental results, in contrast with the spread rates obtained from the non-delayed theory [Eqs. (1.5)-(1.7)]. Moreover, the authors introduced additional important terms in their equations, thus modelling relevant features of the system such as hindered diffusion (due to the presence of cells in the medium) and a more realistic logistic growth for infected cells.

1.1.3 The Neolithic transition

The first Eurasian agricultural civilizations appeared about 10,000 years ago in the Near East, and spread gradually across Europe. The resulting transition from hunter-gathering (Mesolithic) to farmer (Neolithic) economics is known as the Neolithic trans-

[1] The original equations for the virus-host system in Ref. [22] contain an additional term for the desorption of virions from their host. However, the desorption rate constant k_{-1} is generally not significant in comparison with k_1. As a result, the desorption rate does not appear in more recent models of the same authors [23]. Accordingly, the original terms containing k_{-1} have been omitted in Eqs. (1.5)-(1.7).

ition. The expansion process lasted about 5000 years until farming reached the western European coasts.

The idea of an expansion of migratory farmers (called demic diffusion) coming from the Near East and colonizing Europe was first introduced by Childe in 1925 [24, 25]. However, the first population dynamics model for the Neolithic would not appear until 1973. Noticing that radiocarbon dates revealed an approximately steady rate of spread [26], Ammerman and Cavalli-Sforza applied the wave of advance model (i.e., the same model used by Fisher and also by Skellman some decades before, see Sec. 1.1) to the Neolithic transition [27, 28].

Following this first model by Ammerman and Cavalli Sforza, the Neolithic transition has been widely studied using physical and mathematical models (for a recent review, see [4]). Some of the different approaches used to describe the Neolithic expansion include age-structured population models [29], realistic dispersal kernels [30] and settlement formation [31]. In 2005, Pinhasi et al. [32] improved previous data analysis by studying a database of 735 early Neolithic sites from Europe and the Near East. This permitted the authors to derive a range for the spread of farming in Europe of $0.6 - 1.1$ km/yr [2].

Recently, N. Isern devoted her PhD thesis [33] to model the Neolithic transition. Her work not only shaded some light on fundamental questions of the Neolithic transition, but also led to remarkable advances in front spreading. For example, Isern and her collaborators explored the effects on the Neolithic front speed when considering complex dispersal kernels, took proper care of reactive terms in the HRD equation (1.2), and developed models which could explain the slowdown of the Neolithic transition at high latitudes.

1.2 Evolution of cooperation

> Creatures of every persuasion and level of complexity cooperate to live.
> *Martin A. Nowak*

The revolutionary masterpiece *On the Origin of Species by Means of Natural Selection, or the preservation of Favoured Races in the Struggle for Life*, published in 1859 by Charles Darwin, laid the foundations for the contemporary theoretical framework of evolution. Though his book inspired uncountable powerful advances (and it still does), Darwin himself thought that cooperation had escaped from his pioneering vision of the struggle for existence. Apparently, only selfish individuals could live in a world ruled by competition and natural selection.

From cellular cooperation (which permits multicellular life) to social establishment (not necessarily human), cooperation in nature presents manifold faces. In 1902, Pyotr A. Kropotkin proposed the first solid interpretation that suited cooperative behavior to evolution [34]. Many leading-edge ideas on the subject were shaped in the 20th century, such as inclusive fitness theory by W. D. Hamilton in 1964 [35]. In his seminal work,

[2] This observed range for the spread of the Neolithic population is discussed in section 3.1.3.

Hamilton proposed that natural selection acts towards genes, rather than individuals. This could lead individuals sharing specific genes to cooperate with each other. In 1973, J. Maynard Smith and G. R. Price tackled the question of cooperation from the innovative perspective of evolutionary game theory [36]. This new vision remarkably promoted the mathematical analysis of cooperation. A few years later, R. Axelrod and W. D. Hamilton organized a computer tournament [37] in which several strategies (proposed by many scientists around the world) were challenged in a repeated version of the Prisoner's Dilemma (PD) game (which will be introduced in chapter 7). In the last four decades, a huge amount of seminal works have established evolutionary game theory as the major tool for the study of cooperation (for a recent review, see Ref. [38]).

The main idea on evolutionary game theory lays in playing multiple rounds of a game. In such game, individuals can reach different payoffs (or fitness, in the case of biological studies) depending on the strategy they play. One of the most commonly used games is the Public Goods (PG) game. Let us present this game with a classical one-shoot experiment. Initially, n players (let us consider, e.g., $n = 6$) are given \$10 each. They will be asked to make a choice between whether investing their money in a common pool or not. They know that the experimenter will triple the amount accumulated in the common pool at the end of the round, then divide the resulting amount between the six players (irrespective of wether they contributed or not). Provided all the players contribute, the game ends with \$30 in each player's pocket. However, a rational player is tempted to free ride, contributing nothing to the common pool but, nevertheless, receiving the benefits produced by contributors. For example, if only one player chooses to free-ride (defect), the common pool will accumulate \$50 (i.e., \$150 after the experimenter triples the investments). Hence the defector would end the game with \$35 (i.e., \$25 plus the original \$10), which is more than he/she can achieve by contributing (cooperating). Indeed, a selfish player will always defect, independently of the strategies his/her coplayers play. This leads rational players to engage in the worst scenario in which no one contributes, producing no benefits at all. In the case of playing multiple rounds, this outcome would last until the game was ended. This situation is known as the tragedy of the commons[3], and it is useful to describe relevant problems such as global warming or recycling. In both cases, the contribution from cooperators (e.g., countries contributing to reduce the CO_2 emissions) will benefit the whole population (including free-rider countries).

Fortunately, in human societies (and in biological populations in general) cooperation is present, indicating cooperative behavior is worth at least in some special situations. In the last years, a large number of studies have focused on several key mechanisms for the evolution of cooperation, such as kin selection [35], spatial structure [39], group selection [40], reciprocity [37, 41] or punishment [42]. The last one (as well as the indirect kind of reciprocity [41]) is inherent to humans because it requires complex cognitive abilities.

[3]This deplorable outcome of selfish motives is also known as social dilemma, free-rider problem or market failure.

1.3 Population dynamics models in this thesis

1.3.1 Overlapping-generations model

The previous nonstructured-populations model for postglacial recolonization fronts introduced in section 1.1.1 naturally suggests a rigorous analysis beyond the nonoverlapping-generations assumption. Chapter 4 presents a structured-population model in which the effects of overlapping-generations are studied. In contrast to previous 1D studies on structured-populations (which consider linear habitats), an expression for the front speed of 2D biological invasions is derived. For this purpose, the paper in chapter 4 improves the matrix notation by Neubert and Caswell [19] in order to describe both reaction and dispersal processes affecting populations in two dimensions. Analytical results are obtained from both continuous-space and discrete-space random-walk theories and verified with reactive random-walk simulations (see chapter 3). Chapter 4 also compares the speed of 2D fronts with the results from the 1D theory.

Finally, the overlapping-generations model is applied to the yellow poplar species. This allows a comparison with the nonoverlapping-generations model in the context of postglacial recolonizations fronts. The discussion in chapter 4 reveals that theoretical front speeds from both models could solve the Reid's paradox if long-distance dispersal events are considered. However, the overlapping-generations assumption is a more realistic approach, since it better describes the population dynamics in a wide range of situations (e.g., considering low reproduction rates).

1.3.2 Virus infection speeds

Chapter 5 presents a time-delayed model for the Vesicular Stomatitis Virus (VSV), which infects mammalian cells. In this work, the model for virus infections in Ref. [10] is improved in order to properly compute the time partial derivative of the growth function in the HRD equation, as it was recently proposed by Isern and Fort for single-species systems [43]. The front speed of VSV infections is computed from reaction-diffusion differential equations (see chapter 3). Moreover, theoretical front speeds are conveniently checked with results from numerical integration (see chapter 3), which additionally permit to study the evolution of the concentration profiles. Both theoretical results and simulations yield front speeds which are in perfect agreement with observed data on VSV infections. Remarkably, chapter 5 proposes an extremely simple, approximate expression for the spread rate of viruses (see also the following subsection). The approximate front speed is extraordinarily helpful in order not only to simplify the exact theoretical results from the complex equations of the system, but also to understand the critical importance of the delay time in VSV infections.

Finally, the work in chapter 5 aims to avoid the use of adjusted parameters. Remarkably, the only two nonmeasured parameters in the model are shown to be not crucial for the main conclusions in that chapter.

1.3.3 Lag-driven motion in front propagation

When considering the limit of high reproduction rates, the same approximate front speed is obtained from several models of populations showing time-delayed migrations. This approximate speed simply reads:

$$c = \sqrt{\frac{2D}{T}}. \tag{1.8}$$

In chapter 6, the above approximate front speed is derived from three reaction-diffusion models, namely, the HRD equation (1.2) for one species systems, the structured populations model in chapter 4 and the multiple species model for virus infections in chapter 5. Moreover, the approximate speed (1.8) is compared with both analytical exact solutions and numerical simulations results for several biological population fronts described by the three models. Observed spread rates on specific biological populations (namely, the Neolithic transition, postglacial recolonization fronts and several virus infections) are compared to theoretical solutions for the front speed. For all the cases analyzed, the approximate front speed (1.8) lies within the corresponding observed range.

1.3.4 Probabilistic punishment in mobile populations of Prisoner's Dilemma players

Chapter 7 focuses on the spread and success of cooperative strategies when mobile players are able to punish their partners. Among the wide list of recent studies on cooperation, two recent papers specially inspired the paper in chapter 7. On the one hand, Meloni et al. noticed that continuous motion of players is a seldom studied scenario [44]. In fact, player's mobility has been traditionally restricted to the vertexes of grids (or networks). On the other hand, an innovative experiment by Herrmann et al. [45] showed that human players punish not only defector partners with notable frequency, but also cooperators.

The model in chapter 7 considers players engaging continuous motion within a 2D square. The usual scenario where selfish motives are favoured is evidenced through the Prisoner's Dilemma (PD) game (which can be seen as the two-persons version of the PG game explained in section 1.2). The model presents an innovative way to introduce punishment by means of a probability to punish the coplayer that is directly assigned to interactions. More specifically, two types of punishment are considered. While the social punishment probability determines the frequency of cooperator against defector punishments, the nonsocial punishment probability rules for the rest of the interactions.

Extensive simulations in chapter 7 analyze the effects of all the relevant parameters (namely, the temptation to defect, the mobility and the probabilities of both social and nonsocial punishment) of the model. Modest doses of mobility or punishment are shown to enhance the fraction of cooperators in the system. Noticeably, these results resist a moderate practice of non-social punishment (which directly acts towards cooperation) in the system.

Chapter 2

Objectives

The main aim of this thesis is to study several spatial systems from a biophysical perspective. The work that has yielded the papers in the next chapters has been motivated by the following main objectives:

- Studying the effects of the overlapping-generations in 2D population fronts. The front speed from the 2D structured populations theory will be compared to observed spread rates of postglacial forest recolonizations, and to previous nonoverlapping 2D and overlapping 1D models.

- Developing a model for VSV focal infections using realistic time-delayed reaction-diffusion equations. Assessing the role that the delay (or lag) time has in VSV infections. This aim will be accomplished by comparing the front speed from the time-delayed model with observed front speeds and the results from previous non-delayed models.

- Analyzing the validity of a new approximate front speed, namely $c = (2D/T)^{1/2}$, in the context of several time-delayed, biological population fronts. Checking its results by comparing to exact theoretical results and observed spread rates of three different biological systems (namely, virus focal infections, the Neolithic transition, and postglacial forest recolonizations).

- Studying the evolution of cooperation in spatial systems where agents can both move continuously and punish. Considering both social and nonsocial practices of punishment with the aim to check their effects in virtual populations playing the PD game.

Chapter 3

Materials and Methods

This chapter provides an in-deep discussion on some empirical data for the biological populations considered in this thesis, as well as an assembled description of the analytical and numerical methods which were necessary to develop the models. Since this thesis has been prepared as a collection of papers, some of the information in the sections below may be summarized in the following chapters. In order to study the dynamics of biological populations, the models in next chapters make use of two kinds of equations which require rather different techniques to compute the front speed. Thus, the analytical and numerical methods have been classified according to which kind of equation they are appropriate to solve. The last section in this chapter presents some experimental evidences which support the use of punishment in models for the evolution of cooperation, as well as a concise explanation regarding how periodic boundary conditions are applied in chapter 7.

3.1 Empirical data

3.1.1 Postglacial recolonizations

- **Age at first reproduction** T. This parameter determines the age at which trees reproduce for the first time. Observed values of the maturation age of many tree species have been previously published in several US agriculture department handbooks (see, e.g., Refs. [46, 47]). In this work we shall use values of T for the following two species. The range $15 - 20$ yr for the age at first reproduction of the yellow poplar was observed in the review of the silvical characteristics of this species by Donald E. Beck in Ref. [46]. For the case of the black alder, the value $T = 6$ yr lays within the observed range published in the study by Harrington et al. [47].

- **Characteristic dispersal distance** Δ (or Δ_0) . The seed dispersal distances considered in this thesis correspond to long-distance dispersal (see Sec. 1.1.1), because short-distance dispersal has a negligible effect on front spread rates [15]. In a previous work by Nathan et al. [18], a mechanistic model for the long-distance

dispersal of seeds by wind was tested against seed data collected along a 45 m walk-up tower. 102 seed traps placed at 12 levels along the tower collected thousands of seeds of five wind-dispersed tree species (including the yellow poplar species) during 35 summer days. This led the authors to predict with their mechanistic model long-distance dispersal in the range $10^3 - 10^4$ m. In chapters 4 and 6, realistic dispersal distances which lay within this range are considered (namely $\Delta = 6 \cdot 10^3$ m and $\Delta = 6.5 \cdot 10^3$ m for the yellow poplar and the black alder, respectively). The probability of long-distance dispersal is discussed below (in the persistence paragraph).

- **Net reproductive rate per tree and year** R_0. The net reproductive rate is computed as the product of the per capita seed production f and the seed survival rate s. Yellow poplar per capita seed production is of the order of 10^4 seeds per year, according to field observations in Ref. [46]. Concerning postdispersal seed-to-survival, D. De Steven performed an experimental study in which seeds of several trees were sown in different treated sites. For the yellow poplar species, a survival rate of 0.06% was observed in weeded fields, but seeds were unable to succeed in herbaceous covers. In agreement with these results, the seed survival of the species lays in the range $0.00 - 0.06\%$. In this thesis we consider the mean value of this range, i.e., $s = 0.03$. Thus, the range for $R_0 = fs$ applied in next chapters corresponds to $3 - 30$ seeds / tree yr for the yellow poplar.

  Previously published data on the black alder silviculture [47] establishes a per capita seed production of the order of 10^4 seeds per year. On the other hand, no available data has been found on the seed survival rate of this species (indeed, quantifying the survival of seeds travelling long distances is a major challenge for any tree species, since tracking long-distance dispersal events is a very difficult task [48]). For this reason, in this thesis the survival rate of black alder seeds has been approximated as $s = 0.03$ (i.e., the same survival rate considered above for the yellow poplar species). Hence, the estimated range for the net reproductive rate of black alder is $3 - 30$ seeds / tree yr.

- **Lifespan** l. The lifespan determines the order of the matrices in the equations of the overlapping-generations model (chapter 4). According to field observations in Ref. [46], the fertile age of yellow poplar trees lasts to a maximum of 200 years. In chapters 4 and 6, the considered lifespan value is below this maximum, namely $l = 130$ yr [1].

- **Persistence** p_e. The model by Nathan et al. [18] was able not only to predict long-dispersal distances, but also uplifting probabilities for several species. Seed uplifting (i.e., elevation above the top of the canopy) is necessary for wind-mediated long-distance transport of seeds. In Ref. [18] the uplifting and nonuplifting probabilities of yellow poplar seeds were represented as a function of the

[1] As it will be mentioned in chapter 4, considering larger values of l (e.g., $l = 200$) does not apreciably change the front speed predicted by the overlapping generations model.

dispersal distance (see Fig. 2 in Ref. [18]). J. Fort used this information to compute a mean probability of 0.202% for wind associated long-distance dispersals. The persistence parameter p_e accounts for the probability that a seed falls at a distance much smaller to those corresponding to long-range dispersal. Because short-range dispersal has a negligible effect on front speed [15], the models in following chapters assume that seeds are either dispersed to long distances (with probability 0.202%, see above) or not dispersed at all. Accordingly, the value of the persistence corresponds to $p_e = 1 - 2.02 \cdot 10^{-3} = 0.99798$.

- **Postglacial tree spread rate**. Tree spread rates at the end of the Pleistocene have been estimated mainly from the fossil record. ^{14}C-dated pollen sequence analysis from temperate lakes has established postglacial spread rates in the range $10^2 - 10^3$ m yr^{-1} for multiple tree species [49–53]. In Ref. [49] H. J. B. Birks performed a detailed isochrone mapping of the British Isles from 135 radiocarbon pollen diagrams. For the special case of the black alder, such isochrones (which are compared to theoretical results in chapter 6) revealed a spread rate of $500-600$ m yr^{-1}, which is reduced to $50 - 150$ m yr^{-1} when reaching northern latitudes [49]. Recolonization speeds in the range $10^2 - 10^3$ m yr^{-1} have been compared in previous works [12, 15] to theoretical predictions for the yellow poplar, as it is done in this thesis (chapters 4 and 6).

3.1.2 Focal infections

- **Diffusion coefficient** D. In focal infections, this parameter refers to the diffusivity of the virus species in the extracellular medium (i.e. agar). To the best of our knowledge, neither the VSV (studied in chapters 5 and 6) nor the T7 (chapter 6) diffusion coefficient in agar has been measured. As it has been previously done in Ref. [10], the diffusivity of T7 is approximated to the observed value for a virus species which is similar in size and shape [54]: the P22 virus. For the case of the VSV, two approximate values are used in the following chapters. On the one hand, the diffusivity of the VSV in water (which was measured in Ref. [55]) is applied. On the other hand, the diffusivity of the P22 in agar is also used to describe the diffusion of the VSV.

  The diffusion coefficient of the p22 through agar was measured by Stollar and Levine in Ref. [54]. The authors used the technique of double diffusion in agar in two dimensions, which allows both a virus and its corresponding antibody to diffuse toward each other from two separate depots. At the point where the virus and the antibody meet, an observable precipitate is formed[2]. Stollar and Levine initially stored the p22 virus and its antigen in troughs (which had previously been moulded into the agar layer) at right angles to each other, as shown in Fig. 3.1. As a result of the diffusion of both the virus and the antibody, a precipitin straight band (represented by the arrow in Fig. 3.1) appeared in the agar. The

[2]The observability of the precipitate depends on the transparency of the agar gel and the concentrations of both the virus and the antigen, see Ref. [54].

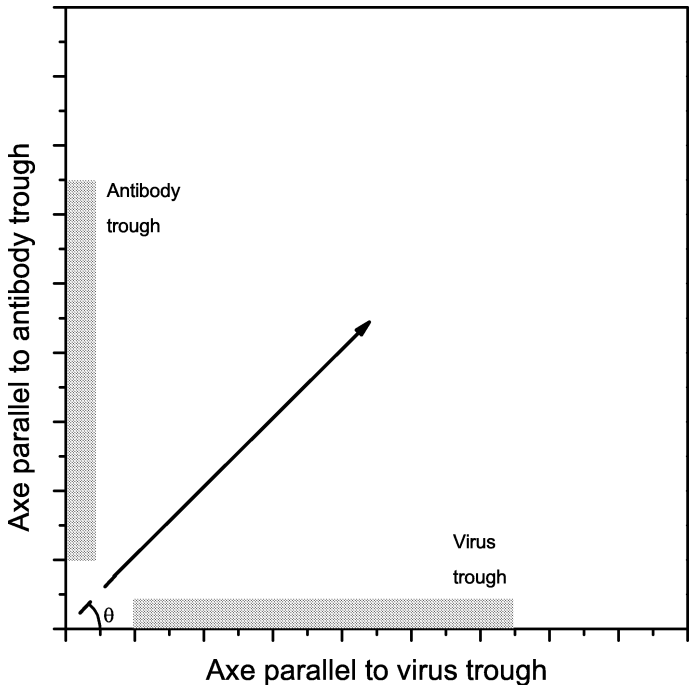

Figure 3.1: Scheme of the experimental setup for the measure of the diffusion coefficient of the p22 virus, as described by Stollar and Levine [54]. As expected intuitively, the precipitin band first appears at the point where the reactants are closest, then it extends outwards (as indicated by the arrow).

angle θ between this band and the virus trough is such that $\tan\theta = (D_v/D_a)^{1/2}$, where D_v and D_a are the diffusion coefficients of the virus and the antibody, respectively. From the value of D_a (namely, $1.37 \cdot 10^{-3}$ cm^2/hr for the rabbit antibody considered in Ref. [54]) and the measure of θ, the authors derived the value of $D = 1.44 \cdot 10^{-4}$ cm^2/hr for the diffusivity of the p22, which is applied in chapters 5 and 6.

The diffusivity of the VSV in water was measured by Ware et al. [55] by quasielastic light scattering. This technique is based on the Doppler broadening of scattered laser light caused by Brownian motion of macromolecules. Assuming spherical macromolecules, a Lorentzian scattered light spectrum is expected. The half-width of such spectrum is theoretically equal to DK^2, where $K = (4\pi n/\lambda_0)\sin(\theta/2)$ (n is the index of refraction of the solution, λ_0 is the incident wavelength and θ the scattering angle). Ware et al. used this relation to derive the diffusivity $D = 8.37 \cdot 10^{-5}$ cm^2/hr of VSV particles in a specific water solution [55].

- **Initial concentration of non-infected cells** C_0. The initial cell concentration is used to convert the equations of the focal infection models to their dimensionless form. Moreover, this parameter is applied in numerical simulations to set the initial conditions (see section 3.3.2). However, the value of C_0 does not affect the

virus infection speed (unless hindered diffusion is considered, see section 1.1.2). In this thesis, free diffusion is considered when modeling VSV infections (because hindered diffusion is important only in specific situations where C_0 is close to its maximum possible value [10]). For VSV infections, the initial cell concentration $C_0 = 3.8 \cdot 10^7$/ml (which was estimated in Ref. [23]) is applied. Concerning T7 mutants, the initial cell concentration $C_0 = 3 \cdot 10^6$ /ml from the experiments in Ref. [56] is used. Since this value of C_0 is close to the maximum possible value (namely 10^7 /ml) in the experiments [56], hindered diffusion is considered for the case of T7 infections.

- **Rate constant for virus adsorption** k_1. The adsorption rate for the T7 into *E. coli* bacteria was derived by Fort and Méndez in Ref. [10]. The authors used available data on an homogeneous, nonreproductive adsorption experiment in Ref. [57]. In such experiment the T7 virus reproduction is inhibited by the presence of KCN, and thus the dynamics of the system is governed by:

$$\frac{\partial [C]}{\partial t} = \frac{\partial [V]}{\partial t} = -k_1 [C][V] = -\frac{\partial [I]}{\partial t}. \tag{3.1}$$

From equation (3.1), it follows that $[C] = [V] + \alpha$, where the constant α is easily derived from the initial concentrations of $[V]$ and $[C]$. Furthermore, the solution for $[V]$ satisfies the relation $\ln\{([V] + \alpha)/[V]\} - \ln\{([V]_{t=0} + \alpha)/[V]_{t=0}\} = \alpha k_1 t$. This allowed Fort and Méndez [10] to determine the slope αk_1 from the observed concentrations of $[V]$ in the nonreproductive experiment [57]. In this way, they obtained the range $k_1 = (1.29 \pm 0.59) \cdot 10^{-9}$ ml/min for T7 infecting *E. coli*. In chapter 6, the mean value of this range (i.e., $k_1 = 1.29 \cdot 10^{-9}$ ml/min) is used to compute the exact theoretical speed of T7 focal infections [and the exact speed is compared to the approximation (1.8)].

In chapters 5 and 6, the value $k_1 = 1.4 \cdot 10^{-10}$ cm^3/h is applied in theoretical analysis of VSV infecting Baby Hamster Kidney (BHK) cells. This value was originally adjusted to the extracellular model by Haseltine et al. in Ref. [23]. Since no data on nonreproductive VSV experiments is available, it has not been possible to provide an empirical range of k_1 for VSV, but the results will be shown not to change appreciably for values of k_1 over four orders of magnitude.

- **Rate constant for the death of infected cells** k_2. The value of this parameter can be easily derived from one-step growth experimental data. In one-step growth experiments, the time evolution of the virus concentration in a homogeneous medium without adsorption is studied. Initially, the system is composed of infected cells (with a density close to saturation, $[I]_0 \simeq I_{MAX}$) and a few free viruses. The growth of the virus population in such systems can be described by the solution

of the logistic equation[3], which reads:

$$[V](t) = \frac{Y\ I_{MAX}}{c_1 \exp[-k_2 t] + 1}, \tag{3.2}$$

where c_1 is an integration constant that depends on the arbitrary definition of the moment $t = 0$.

The symbols in Fig. 3.2 show observed concentrations of the p005 strain of the T7 virus after one-step growth experiments in Ref. [56] (the data points in the inset of Fig. 3.2 refer to VSV experiments in Ref. [58]). Least-square fit of the data to Eq. (3.2) (solid line in Fig. 3.2) yields the observed rate $k_2 = 44.5$ hr^{-1} for the p005 mutant of the T7 infecting *E. coli*. The same procedure leads to $k_2 = 2.47$ hr^{-1} for the VSV infecting BHK cells (inset of Fig. 3.2). In this thesis, we also make use of the value $k_2 = 83.4$ hr^{-1} for the wild strain of the T7 infecting *E. coli*, which was derived by Fort and Méndez in Ref. [10] using the same method described above.

- **Yield** Y. The yield can be estimated as the ratio of the final virus concentration to its initial value in one-step growth experiments [4]. Thus, from the data in Fig. 3.2 we obtain $Y = [V]_f/[V]_0 = 63.6$ for the p005 strain of the T7. This same method was used in Ref. [10] to compute the yield $Y = 34.5$ for the wild strain of the T7. Moreover, applying this same ratio to the experimental data in the inset of Fig. 3.2 leads to $Y = 2.77 \cdot 10^5$ for the VSV (which is used in chapter 5). However, virus concentrations in Ref. [58] (which have been reproduced in the inset of Fig. 3.2) are expressed in PFU/cell instead of PFU/ml. This makes unnecessary to compute the ratio between the initial and the final concentration, and the yield can be estimated as the final virus concentration in the experiment, which leads to $Y = 4389$. This latter value is applied to VSV infections in both chapters 5 and 6.

- **Observed lag time** τ. This is the time elapsed since the adsorption of a virus by a cell, and the release of its progeny (Y virus). For T7 infecting E. Coli, the range $15 - 25$ min is obtained from the interval time in which virus concentration rises in one-step growth experiments (see hatched area in Fig. 3.2). For VSV infecting BHK cells, τ is much larger, about $5 - 10$ hr (hatched area in the inset of Fig. 3.2).

- **Observed infection speeds.** The spread of VSV infections on BHK cells was monitored by Lam et al. in Ref. [58]. The authors captured representative images of focal infection experiments using indirect immunofluorescence labeling of VSV-glycoprotein. This technique involves the use of antibodies which fix to virus

[3] A detailed discussion on logistic equations to model one-step growth experiments is provided in the appendix A in chapter 5.

[4] In fact, the experimental dots before the rise in $[V]$ (see Fig. 3.2) refer to infected cells concentration [59].

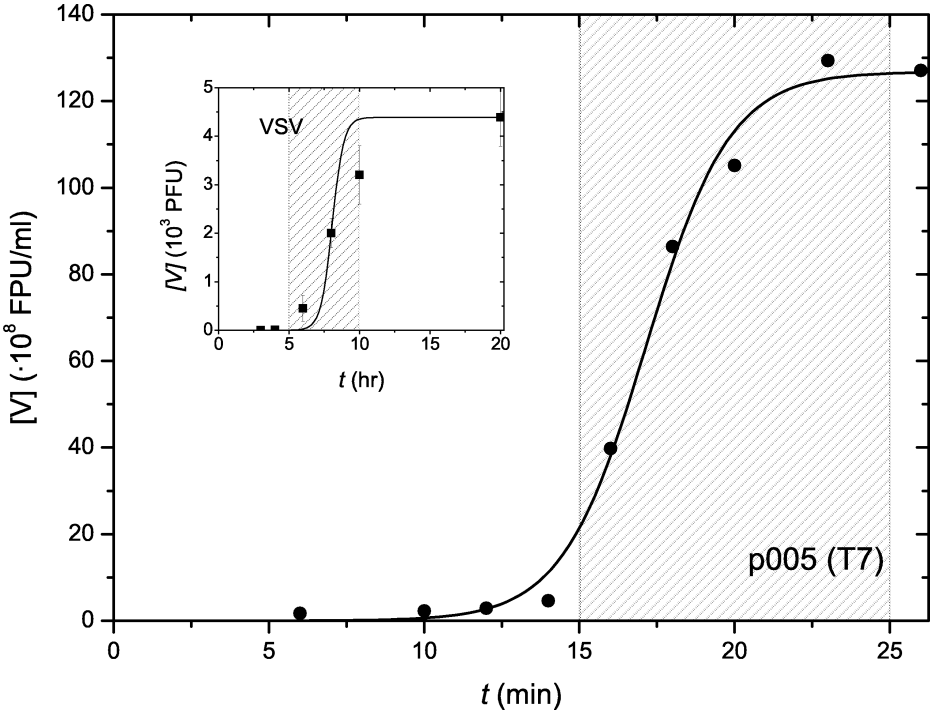

Figure 3.2: One-step growth of p005 (a strain of the T7 virus) on *E. coli* versus the time elapsed after adsorption. The solid line depicts the least-square fit of experimental data points [56] to Eq. (3.2). The interval time in which the rise in virus concentration is produced corresponds to the observed range of the lag time τ (hatched area). Inset: one-step growth of N1 (a strain of the VSV) on BHK cells. The solid line stands for the least-square fit of experimental data points [58] to Eq. (3.2). The hatched area corresponds to the observed range of τ for VSV infecting BHK cells.

proteins and can be visualized by fluorescence analysis. Thus, the fluorescence intensity reveals the virus distribution in the cell monolayer. Lam et al. [58] derived the VSV spread rate $c = 7.3 \cdot 10^{-2}$ cm/hr from linear regression of the mean infection radius at several times after virus inoculation. Considering the 95% confidence-level interval yields the range $(6.6 - 8.0) \cdot 10^{-2}$ cm/hr, which is used in chapter 5. However, Haseltine et al. [23] presented fluorescence intensity profiles on the same images in Ref. [58]. Linear regression of the position of maximum intensity peaks [23] at several times after inoculation leads to a spread rate of $5.6 \cdot 10^{-2}$ cm/hr. This latter infection speed is taken into account in chapter 6, in which the more realistic range $(5.6 - 8.0) \cdot 10^{-2}$ cm/hr is considered for VSV infections. It is worth to note that the above infection speed ranges refer to the N1 strain [58] of the VSV (i.e., the same strain considered in the above computation of empirical values for k_2 and Y).

J. Yin performed focal infection experiments with several T7 strains infecting *E. coli* in Ref. [56]. Yin measured the evolution of the plaque diameter in multiple

experiments for each virus strain. Infection speeds in the ranges $(1.6-2.2)\cdot 10^{-2}$ cm/hr, and $(1.9-2.7)\cdot 10^{-2}$ cm/hr were observed for the wild and the p005 strains, respectively. Since these two intervals are very close to each other, a unique range for the spread of the T7 mutants (namely, $(1.6-2.7)\cdot 10^{-2}$ cm/hr) is considered in chapter 6. Note that this latter range embraces observed infection speeds for either of the considered T7 strains (see above).

3.1.3 Neolithic human populations

This section summarizes the empirical data on the Neolithic transition which will be used in chapter 6. A more detailed discussion on available data for the Neolithic transition can be found in a recent Ph.D. thesis by N. Isern [33].

- **Initial growth rate a.** This parameter indicates the rate of growth when the population number N is low, and $\frac{\partial N}{\partial t} \simeq aN$. In Ref. [30], a was estimated from data on the evolution of the population number in human first colonizations of the Pitcairn Island, the islands of the Furneaux group in the Bass Strait, and the Tristan da Cunha islands. Moreover, the evolution of the population number of the United States during the period 1790-1910 was also analyzed. For the mentioned islands, each data set was fitted to an exponential curve for the corresponding early colonization period. This allowed to derive the corresponding ranges for a. Instead, for the case of the United States population the data was fitted to a logistic growth function [i.e., $\frac{\partial N}{\partial t} \simeq aN(1-N/N_{MAX})$] which permitted to evaluate a. From the corresponding ranges for the four colonizations above, Isern et al. [30] computed the 80% confidence level range for the growth rate, obtaining $a = (2.8 \pm 0.5)\cdot 10^{-2}$ yr^{-1}, which is the range considered in chapter 6.

- **Mean squared displacement per generation Δ^2.** In Ref. [30], the authors proposed a range for the mobility of the Neolithic population. This range was estimated from available data on the mobility of the Majangir people [60], a population of pre-industrial agriculturalists in Ethiopia. Mobility data per generation for three specific Majangir groups were used to estimate the range $\Delta^2 = (1531 \pm 598)$ km^2 [30].[5] This range is applied in chapter 6.

- **Lag time τ.** For the case of human populations, the lag time τ corresponds to a generation time, defined as the mean age difference between parents and one of their children (not necessarily the eldest). The mean lag time for the Neolithic population has been estimated in Ref. [61] using data for the Majangir population [60]. More recently, Isern derived the 80% confidence level range $\tau = (32 \pm 3)$ yr [33] from the same data used in Ref. [61].

[5] In this thesis, Δ^2 refers to the mean squared displacement per generation, which is expressed in km^2. This simplifies the notation in chapter 6. Note that in Refs. [30, 33] the mean squared displacement per generation is defined as $< \Delta^2 > /T$ (where T is the mean time difference between the migration of parents and their children), and its corresponding units are km^2/gen.

- **Spread rate for the Neolithic transition in Europe.** In chapter 6 the range $0.6 - 1.1$ km/yr for the speed of the Neolithic spread is considered. This range is based on the data in Ref. [32], where the authors used the dates of 765 early Neolithic sites in Europe to derive an observed range for the spread of the Neolithic transition. Although such range corresponds to $0.6 - 1.3$ km/yr if both calibrated and uncalibrated dates are taken into account, observed spread rates lay within the interval $0.6-1.1$ km/yr if only calibrated dates are considered. This range includes the results using great-circle distances ($0.6 - 1.0$ km/yr) and using shortest-path distances ($0.7 - 1.1$ km/yr). Great-circles do not take into account geographic barriers such as seas. The short-distance approach in Ref. [32] takes the Mediterranean sea into account but allows for short sea travels, as implied by the arrival of the Neolithic to islands such as Cyprus.

3.2 Fronts from integrodifference equations

Integrodifference equations are integral recurrent relations (such as Eq. (1.3) in chapter 1) which are widely used in mathematical biology to model the evolution of the population density. Both the nonoverlapping generations and the overlapping generations models for tree recolonizations discussed in this thesis are based on this kind of equations. This section presents three different techniques that will be used in subsequent chapters to compute the front speed from integrodifference equations.

3.2.1 Continuous-space random walks (CSRW)

The computation of the front speed from analytical methods is subject to four main assumptions. First, the evolution equation of the system is linearized in terms of p. Thus the speed is computed at the leading edge of the front, where low population densities are expected. This typically affects the growth process, and may neglect terms accounting for saturation effects in the growth function [also called the source function, for example F in Eq. (1.2)][6]. Admittedly, the models for tree recolonizations in the following chapters are already linear in terms of p, hence this first assumption does not modify their equations. As we deal with radially symmetric 2D fronts, the second assumption considers that for $t \to \infty$ the front is approximately planar at scales much larger than those of individual dispersal events. Thus, choosing the x axis parallel to the local velocity of the front, we can neglect the dependence of p along the perpendicular direction (y). The third *ansatz* presumes the solution has the shape $p = p_0 \exp(-\lambda z)$ for large values of the coordinate $z = (x - ct)$. Hence,

$$\begin{aligned} p(x, y, t + T) &= p(x, y, t) e^{\lambda c T} \\ p(x + \Delta_x, y + \Delta_y, t) &= p(x, y, t) e^{-\lambda \Delta_x}. \end{aligned} \tag{3.3}$$

[6] A nonlinear growth function example can be found in chapter 5 (see specially appendix A there), where quadratic saturation terms are taken into account for the infected cells population.

When introducing the above relations into an integrodifference equation (such as the nonoverlapping equation (1.3)) we obtain a complex equation for the front speed c which depends on the unknown parameter λ. Then, marginal stability (or linear) analysis [62] is applied in order to obtain the exact solution for the front speed. This last step is equivalent to assume that the minimum possible speed is the one of the front. However, for strongly non-linear source functions (such as those arising in combustion fronts) this assumption is not valid [1]. Therefore, as we shall see below, some methods have been used to check the speeds obtained using this assumption (and the other three assumptions above) for all of the models in this thesis.

For example, applying the four assumptions explained above to the non-structured tree population equation (1.3) leads us to:

$$c = \min_{\lambda>0} \frac{\ln[R_0 \iint e^{-\lambda \Delta_x} \phi(\triangle_x, \triangle_y) d\triangle_x \, d\triangle_y]}{\lambda T}. \tag{3.4}$$

This cannot be solved explicitly, so the function $c(\lambda)$ is plotted numerically and its minimum is found. Considering an isotropic kernel (as it will be done in chapter 4) slightly simplifies the integral in the above equation. However, the resulting expression is still complex and does not lead to an explicit solution. For this reason, the exact analytical speeds for postglacial recolonizations in this thesis (Chapters 4 and 6) have been computed numerically. The validity of equations such as (3.4) can be checked by means of the methods in the two subsections below.

3.2.2 Discrete-space random walks (DSRW)

The method explained in the previous section considers continuous space. In other words, individuals (or seeds) can be dispersed into any point in the 2D plane. However, this scenario is significantly different to that regarded by numerical simulations. In this latter case, the population density is computed explicitly. However, this can be done only at a finite number of points (e.g., at the nodes of a 2D grid), thus considering discrete space. Using discrete-space random walks (DSRW) provides analytical results for the front speed that are directly comparable with those from numerical simulations.

In order to take into account discrete space, the integral in the evolution equation for the population density has to be conveniently modified. For example, if we perform a DSRW analysis of the nonoverlapping generations Eq. (1.3), the integral:

$$\int_{-\infty}^{+\infty} \int_{-\infty}^{+\infty} p(x + \triangle_x, y + \triangle_y, t) \phi(\triangle_x, \triangle_y) d\triangle_x \, d\triangle_y, \tag{3.5}$$

must be discretized according to the assumptions used in the numerical simulation. In chapters 4 and 6, numerical simulations for tree colonizations (see section 3.2.3) consider seed dispersal to any of the four nearest neighbors with probability $(1 - p_e)/4$. It follows that seeds remain at the same location of their parent tree with probability p_e (this corresponds to short-distance dispersal, i.e., to negligible distances). Thus, in the DSRW approach Eq. (3.5) is replaced by:

$$p_e\ p(x,y,t) + \frac{(1-p_e)}{4}\left[p(x \pm \Delta_0, y, t) + \ p(x, y \pm \Delta_0, t)\right], \tag{3.6}$$

Then, the same mathematical analysis applied to CSRW above is used to compute the front speed from DSRW. That is, low population densities are assumed, as well as planar fronts and $p \simeq p_0 \exp(-\lambda z)$ (with $z = (x - ct)$), and marginal stability is applied. Note that modifications in the dispersal kernel in order to consider discrete spaces can lead to anisotropic front speeds. Fig. 3.3 graphically shows the horizontal (or vertical) spread rate is necessarily faster than the diagonal one if only jumps to the four nearest neighbors are taken into account. Because of this, in next chapters the DSRW speed will be computed for both the horizontal and the diagonal directions of propagation. The front speed will be obtained as the resulting average value, as it is the most accurate speed that both DSRW and simulations can provide.

Finally, note that Fig. 3.3 might lead to the conclusion that the front speed along the horizontal direction is simply r/T, and that along the diagonal direction $\sqrt{2}r/T$. In fact, it has been shown that this happens only in the limit of very fast growth functions [63], because the front speed depends in general not only on the dispersal process (Fig. 3.3) but also on the reproductive one (e.g., Fig 3.2).

3.2.3 Reactive random-walk simulations

In this kind of numerical simulations, the evolution of the population density is computed in time and space. For this purpose, a 2D grid must be defined in order to consider the population number density in its vertices. Then, the initial conditions in the grid are set (typically, $p(x, y, 0) = p_{\max}$ at $(x, y) = (0, 0)$ and $p(x, y, 0) = 0$ elsewhere). At each time step, both reaction (i.e., growth) and dispersal effects are computed at every node. As a consequence of dispersion processes, the population is redistributed according to the dispersal kernel $\phi(\Delta_x, \Delta_y)$, but approximated to a discrete grid. Below, the main steps in an iteration of the numerical simulations are outlined for the specific case of tree colonizations.

At each time step, seed production is determined. This is done by multiplying the tree population density $p(x, y, t)$ by the net reproduction rate R_0 at each node of the grid. Then, this seed population is distributed in accordance with the dispersal kernel, which considers dispersion to the four nearest neighbors as it is shown in Fig. 3.3 (see also Sec. 3.2.2). After dispersal has been computed at every node, the resulting seed distribution becomes the new population density $p(x, y, t + T)$. Finally, the front speed is obtained from linear regression of the position of successive fronts (defined, e.g., as $p = p_{\max}/10$) when the time is $t >> T$.

Above, the computer program for the non-overlapping generations model has been described. In chapters 4 and 6, reactive random walks simulations for overlapping generations will be performed. Additional details regarding the structure of the population in the numerical simulations will be presented in those chapters.

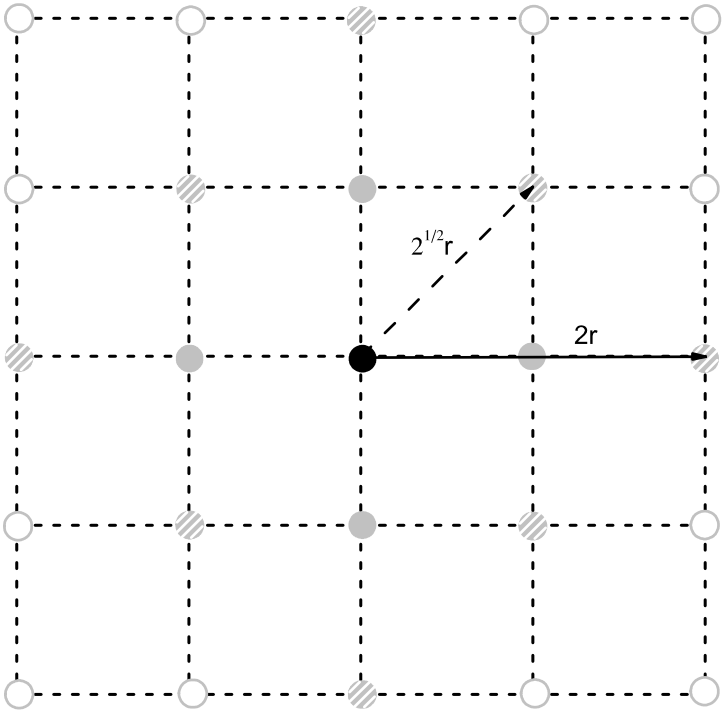

Figure 3.3: Anisotropic spread resulting from seed dispersal (jumps) to the four nearest neighbors in a square lattice. Initially, population density is concentrated in the center of the lattice (black vertex). After one iteration, seeds are dispersed to each of the nearest neighbors (grey vertices) with probability $(1-p_e)/4$. With the same probability, nearest empty vertices will be reached after two iterations (dashed grey vertices). At this time, the population will have spread up to a distance $2r$ (where r is the distance between two nearest vertices) along the horitzontal direction (solid arrow). In contrast, the colonization along the diagonal direction (dashed arrow) will have only reached those vertices located at distance $\sqrt{2}r$ from the initial position.

3.3 Fronts from differential equations

In this thesis, reaction-diffusion differential equations are used to model the evolution of virus infection fronts (Chapter 5 and 6) and the Neolithic transition (Chapter 6). Differential equations [such as (1.2) in chapter 1] require different techniques than integrodifference equations [such as (1.3) in chapter 1] in order to derive the front speed from analytical methods, and specially from numerical simulations. For the sake of clarity, such techniques are explained in this section by considering a specific example, namely virus infection systems. In Ref. [10], Fort and Méndez used the following equations to describe the evolution of T7 infections:

$$\frac{\partial [V]}{\partial t} + \frac{\tau}{2}\frac{\partial^2 [V]}{\partial t^2} = D_{eff}\frac{\partial^2 [V]}{\partial r^2} + F + \frac{\tau}{2}\frac{\partial F}{\partial t}, \tag{3.7}$$

$$\frac{\partial[C]}{\partial t} = -k_1[C][V] \tag{3.8}$$

$$\frac{\partial[I]}{\partial t} = k_1[V][C] - k_2[I]\left(1 - \frac{[I]}{I_{MAX}}\right), \tag{3.9}$$

where τ is the lag time, and F stands for the virus population growth function:

$$F = -k_1[V][C] + k_2 Y[I]\left(1 - \frac{[I]}{I_{MAX}}\right). \tag{3.10}$$

The system of equations (3.7)-(3.10) is an extension of (1.5)-(1.7) that takes care of the lag time effect, as reviewed in chapter 5. Such equations require the methods to derive the front speed that are discussed below. Furthermore, analogous guidelines are relevant when computing numerically the front speed of the Neolithic transition in chapter 6.

3.3.1 Linear analysis

The derivation of the front speed from differential equations is based on the same assumptions as for the case with integrodifference equations (see section 3.2.1). First, low population densities of the invasive species are assumed at the leading front edge. This allows to linearize the reaction-diffusion equations in terms of the population density. For example, in focal infections systems the linearization is made around the unstable steady state $([V],[C],[I]) = (0, C_0, 0)$, taking into account $([V],[C],[I]) = (\epsilon_V, C_0(1-\epsilon_C), \epsilon_I)$ at the leading edge of the front. This leads the virus growth function (3.10) to be rewritten as:

$$F = -k_1 C_0 \epsilon_V (1 - \epsilon_C) + k_2 Y \epsilon_I \left(1 - \frac{\epsilon_I}{I_{MAX}}\right), \tag{3.11}$$

and after linearization, F becomes simply:

$$F = -k_1 C_0 \epsilon_V + k_2 Y \epsilon_I. \tag{3.12}$$

In addition to the growth function F, the complete set of differential equations (3.7)-(3.9) has to be linearized using the same procedure above.

By means of the second assumption, the front can be considered approximately planar for $t \to \infty$ and $r \to \infty$, so the concentrations depend only on r. In accordance with the third assumption, constant shape solutions $\overrightarrow{\epsilon} = \overrightarrow{\epsilon}_0 \exp(-\lambda z)$ with $z = (x - ct)$ are sought. Considering again the example of focal infections, it follows that $\overrightarrow{\epsilon}_0 = (\epsilon_V, \epsilon_C, \epsilon_I)$, and this *ansatz* imposes the following relations regarding the partial derivatives of the population densities:

$$\begin{aligned}
\frac{\partial[V]}{\partial t} &= \lambda c[V], & \frac{\partial^2[V]}{\partial t^2} &= \lambda^2 c^2[V], \\
\frac{\partial[V]}{\partial r} &= -\lambda[V], & \frac{\partial^2[V]}{\partial r^2} &= (-\lambda)^2[V], \\
\frac{\partial[C]}{\partial t} &= -\lambda c C_0 \epsilon_C e^{-\lambda z}, & \frac{\partial[I]}{\partial t} &= -\lambda[I].
\end{aligned} \tag{3.13}$$

Applying these relations to the evolution equations describing the model (e.g., Eqs. (3.7)-(3.9)) leads to a vectorial equation $\overrightarrow{\epsilon} \cdot \overrightarrow{\overrightarrow{M}}(\lambda) = (0,0,0)$ (where $\overrightarrow{\overrightarrow{M}}(\lambda)$ is the matrix corresponding to the linearized evolution equations). For non-trivial solutions $\overrightarrow{\epsilon} \neq \overrightarrow{0}$ to exist, the determinant of $\overrightarrow{\overrightarrow{M}}(\lambda)$must vanish. This gives a characteristic equation which reveals the relation between the front speed and λ (i.e., $c(\lambda)$ is obtained). As when dealing with integrodifference equations in section 3.2.1, the marginal stability assumption [62] is applied, hence the minimum speed corresponds to the one of the front[7].

3.3.2 Numerical integrations: finite-difference method

This section is devoted to explain how differential equations have been numerically solved in this thesis. When performing numerical simulations, the use of dimensionless variables is specially useful because it provide results that can be applied to systems with any parameter values. Dimensionless expressions for both time and space variables are obtained by applying the definitions:

$$\begin{aligned}
\overline{t} &\equiv kt, \\
\overline{r} &\equiv r\sqrt{k/D},
\end{aligned} \tag{3.14}$$

where $1/k$ is the characteristic time of the reactive process [64]. For reaction-diffusion equations for virus infections such as the set (3.7)-(3.9), k corresponds to the rate constant for the death of infected cells k_2. Moreover, the dimensionless expressions for the three population densities read:

$$\begin{aligned}
\overline{C} &\equiv [C]/C_0, \\
\overline{I} &\equiv [I]/C_0, \\
\overline{V} &\equiv [V]/C_0,
\end{aligned} \tag{3.15}$$

[7]It is worth to note that, in a previous work, Isern and Fort computed the exact front speed from the HRD equation without making use of the marginal stability assumption [43]. For the case of one-species systems evolving according to a differential equation, it is possible to apply variational techniques. In this way they found the very same expression when deriving both the lower and the upper bound for the front speed.

where C_0 is the initial cell concentration and, for simplicity, the symbols [ ] have been omitted in the dimensionless population densities. The dimensionless parameters $\overline{\tau} \equiv k_2\tau$ and $\kappa \equiv k_1 C_0/k_2$ are also necessary. Then, for example, the evolution equation (3.8) for noninfected cells is rewritten as:

$$\frac{\partial \overline{C}}{\partial \overline{t}} = -\kappa \overline{C}\ \overline{V}. \tag{3.16}$$

In order to numerically solve differential equations, such as equation (3.16), the *fully implicit* or *backward time* differencing scheme [65][8] has been used. According to this method, the time and space derivatives are finite-differenced as follows:

$$\begin{aligned} \frac{\partial \overline{P}}{\partial \overline{t}} &\simeq \frac{\overline{P}_j^{n+1} - \overline{P}_j^n}{\Delta \overline{t}}, & \frac{\partial^2 \overline{P}}{\partial \overline{t}^2} &\simeq \frac{\overline{P}_j^{n+1} - 2\overline{P}_j^n + \overline{P}_j^{n-1}}{(\Delta \overline{t})^2}, \\ \frac{\partial \overline{P}}{\partial \overline{r}} &\simeq \frac{\overline{P}_{j+1}^{n+1} - \overline{P}_j^{n+1}}{\Delta \overline{r}}, & \frac{\partial^2 \overline{P}}{\partial \overline{r}^2} &\simeq \frac{\overline{P}_{j+1}^{n+1} - 2\overline{P}_j^{n+1} + \overline{P}_{j-1}^{n+1}}{(\Delta \overline{r})^2}, \end{aligned} \tag{3.17}$$

where $\overline{P}$ stands for the dimensionless population density, the superscripts denote the time and the subscripts the space point at which $\overline{P}$ ($\overline{C}$, $\overline{I}$ or $\overline{V}$ in the example of virus infections) is evaluated. The fully implicit differencing scheme has been used in numerical integrations because it is unconditionally stable. Partial derivatives can also be differenced by means of the explicit scheme (which uses the time instant n instead of $n+1$). Although both methods are first-order accurate in time, the explicit scheme requires the use of very short time steps $\Delta \overline{t}$ in order to be stable, thus largely increasing the number of steps required to perform the numerical integration [65].

Applying the fully implicit scheme to a reaction-diffusion equation yields a set of linear equations for each time step $n+1$. For example, Eq. (3.7) for the virus population density generates:

$$\alpha_j \overline{V}_{j-1}^{n+1} + \beta_j \overline{V}_j^{n+1} + \gamma_j \overline{V}_{j+1}^{n+1} = \mu_j, \qquad j = 1, 2 \ldots J-1, \tag{3.18}$$

with α_j, β_j and γ_j the coefficients for $\overline{V}_{j-1}^{n+1}$, $\overline{V}_j^{n+1}$ and $\overline{V}_{j+1}^{n+1}$, respectively; and μ_j a function of $\overline{V}_j^n$ and $\overline{V}_j^{n-1}$. Furthermore, the coefficients α_j, β_j, γ_j and μ_j are necessarily dependent on the population densities of the other species $\overline{C}_j^{n+1}$, $\overline{C}_j^n$, $\overline{I}_j^{n+1}$ and $\overline{I}_j^n$. Note that j is the discrete variable corresponding to coordinate r in Eq. (3.7).

In the above set (3.18), J corresponds to $J = \overline{L}/\Delta \overline{r}$, with $\overline{L} = L\sqrt{k_2/D}$ the dimensionless system size[9]. The set of linear equations (3.18) conform a tridiagonal system that is solved using the Tridag routine in Fortran [65]. In order to obtain a travelling wavefront that is independent of the initial conditions [66], the initial concentrations

[8] See section 16.6 and chapter 19 in this reference for further details on finite-difference methods. The *fully implicit* scheme is described in section 19.2 in this reference.

[9] In the numerical simulations for virus infections in next chapters, equations similar to (3.7)−(3.9) are integrated in one dimension. Instead, the simulations for the Neolithic transition (which involve less complex computations because they deal with only one species) consider a 2D square of side L.

$\overline{C}_j^0$, $\overline{I}_j^0$ and $\overline{V}_j^0$ must be implemented so that they have compact support. For example, appropriate initial conditions are such that

$$\begin{cases} \overline{V}_j^0 = \overline{V}_{\max}, & \text{for } j \leq j_{ic} \\ \overline{V}_j^0 = 0, & \text{for } j \geq j_{ic}+1 \\ \overline{C}_j^0 = \overline{C}_{\max} & \forall j \\ \overline{I}_j^0 = 0, & \forall j \end{cases} . \tag{3.19}$$

In focal infections, the range $j \leq j_{ic}$ corresponds to the area where the virus is initially inoculated.

3.4 Virtual interactions: considering punishment and avoiding border effects.

3.4.1 Evidences of extended human practice of punishment

Altruistic punishment means that a punisher voluntarily pays a cost to incur a loss on an opponent. In the present day, there is a very challenging debate centered on the role that punishment plays on human cooperation. This question has been targeted from multiple field perspectives (such as economy, evolutionary biology, physics, anthropology, etc.) leading to a very large amount of foremost studies (for a recent review, see [42]).

A key problem with punishment is that it generates a social loss by reducing the payoffs of both players. Many experimental studies have shown that this drawback makes punishment a powerless tool for communities to reach high average payoffs. For example, it has been argued that winner's don't punish [67], that reward (which incurs a cost to the rewarder but a benefit to the recipient) is as effective as punishment for maintaining public cooperation and leads to higher total earnings [68], and that costly punishment may disfavor groups in repeated interactions with strangers [69].

In contrast, other behavioral experiments have provided evidences that altruistic punishment is a key element in understanding widespread altruistic behaviors of human societies. In this sense, experiments based on several games (PG, PD, ultimatum game, etc. [42]) have shown that punishment emerges in different patterned fashions among populations from five continents [70], that cooperation flourishes if punishment is possible but breaks down if it is ruled out [71], and that punishment is an evolutionary stable strategy under conditions plausibly characteristic of the early stages of human evolution [72].

Notwithstanding the advantages and drawbacks of punishment, some general trends can be induced from human experiments with punishment. When punishment is an option in the game, human players are willing to make an extended use of it [42]. For example, above 6% of the decisions were punishment in a modified version of the PD game in Ref. [67], but more than the 84% of players punished at least once. Moreover, 34% of players punished at least 5 times when playing the PG game in Ref. [71]. Furthermore, punishment is more frequently directed toward free riders, as it can be

observed in Refs. [45, 69–71]. Therefore altruistic punishment is typically seen as a deterrent for defection.

As it has been discussed in this subsection, punishment practice is frequent among humans. Naturally, theoretical models have been specially useful to explore many of the consequences that punishment produces in large societies (laboratory conditions usually limit the number of participants to a few dozens at once). Chapter 7 in this thesis studies the effects of probabilistic punishment in virtual communities of 1000 individuals. Motivated by recent experimental evidence of frequent antisocial punishment in societies around the world [45], the model in chapter 7 considers not only punishment against defectors but also against cooperators.

3.4.2 Periodic boundary conditions

This section focuses on the periodic boundary conditions which have been applied in the work in chapter 7. At any iteration t, the program considers that individuals play the game with those neighbors laying within their radius of interaction. In Fig. 3.4, the red circle in the center indicates the interaction radius of a defector player (red spot located at the center of the circle). In a 2D square world such as that in Fig. 3.4, players standing close to a border may have fewer opportunities to interact with others (because their interaction area may cover some zones outside the frontiers). Periodic boundary conditions avoid these border effects in the following two ways:

1. Any fraction of an interaction area which extends over a square border is considered to cover an analogous space surrounding the opposite border. For example, in Fig. 3.4 a defector (red spot in the center of the upper broken red circle) is so close to the upper border than his area of interaction crosses the upper limit of the square. The player then benefits from an interaction area near the lower border (broken red circle) which balances the lack in the upper neighborhood. In other words, the player interacts with any neighbor within both broken red circles in Fig. 3.4. Moreover, four fractions of a green circle show the interaction area of a cooperator (green spot) located very close to the lower right side corner.

2. A player whose movement leads him to cross a square border is immediately placed in the corresponding opposite border (the relative position in the border is maintained when switching the player's location). Then, the player continues his motion until he moves the total distance he was supposed to travel.

Indeed, the two considerations above (which are applied in simulations in chapter 7, following Ref. [44]) make the square surface equivalent to a torus.

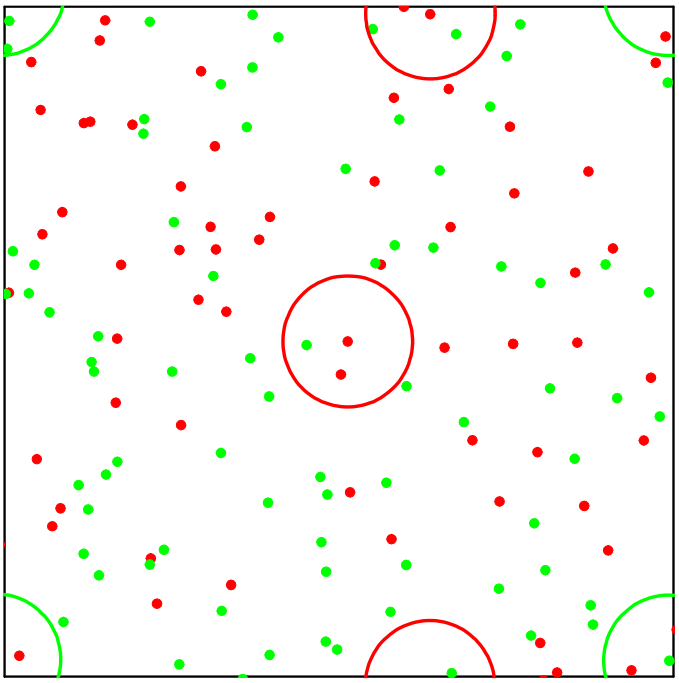

Figure 3.4: Snapshot of a simulation considering a mixed population of cooperators (green spots) and defectors (red spots). The circle in the center indicates the interaction radius of a defector player. The broken red (green) circle shows the interaction area of a defector (cooperator) player which is located close to a border (corner), after periodic boundary conditions have been applied.

Chapter 4

Fronts from two-dimensional dispersal kernels: beyond the nonoverlapping-generations model

This chapter is an exact transcription of the contents of the following paper:

Amor, D. R. & Fort, J. 2009 Fronts from two-dimensional dispersal kernels: Beyond the nonoverlapping-generations model. *Phys. Rev. E* 80, 051918.

Abstract Most integrodifference models of biological invasions are based on the nonoverlapping-generations approximation. However, the effect of multiple reproduction events (overlapping generations) on the front speed can be very important (especially for species with a long lifespan). Only in one-dimensional space has this approximation been relaxed previously, although almost all biological invasions take place in two dimensions. Here we present a model that takes into account the overlapping generations effect (or, more generally, the stage structure of the population), and we analyze the main differences with the corresponding nonoverlapping generations results.

PACS numbers: 87.23.Cc, 89.20.−a, 89.75.Fb

4.1 Introduction

Reaction-diffusion and reaction-dispersal fronts have many applications in physical, biological, and cross-disciplinary systems [1, 62, 73], e.g., virus infection fronts [10, 21], combustion fronts [74, 75], human population fronts [9, 61], etc. Motivated by Reid's paradox of rapid tree range expansions, recently we have proposed a framework which is useful in two-dimensional (2D) space under the assumption of nonoverlapping generations [15]. Modeling forest postglacial recolonization fronts by using single-kernel reaction-dispersal assumptions results in the underestimates of the observed speeds (this disagreement is known as Reid's paradox). In order to better predict such speeds, our recent work introduced several-component kernels (with characteristic distances

differing several orders of magnitude) [15]. In this way, long-distance dispersal (even if occurring infrequently) makes it possible to predict speeds of the right order of magnitude, as observed from postglacial tree recolonization fronts.

However, previous work in two dimensions did not take the age-structure of tree populations into account. Indeed, trees reproduce every year and not only once in their lifetime, so generations clearly overlap. Therefore, here we will extend the 2D model *[15]* to overlapping generations. We shall show that the corrections (relative to the nonoverlapping approximation) are relevant, which justifies the importance of our model. Previously, overlapping-generation models have been only developed in one dimension [19, 76–82]. Our model is relevant not only to tree species, but can be applied to compute front speeds also in other biophysical and physical systems in which the reproductive (or reactive) process happens more than once for each individual (or particle).

4.2 Evolution equation

4.2.1 Nonstructured populations in two dimensions (continuous space random walk)

Integrodifference equations have been widely used to model biophysical and cross-disciplinary reaction-dispersion phenomena. For example, for the case of trees population dispersion (seed dispersal) takes place just after reproduction (seed production). Thus the evolution of a nonstructured population in a 2D space is driven by the well-known integrodifference equation [12]

$$p(x,y,t+T) = R_0 \int_{-\infty}^{+\infty} \int_{-\infty}^{+\infty} p(x+\triangle_x, y+\triangle_y, t)\phi(\triangle_x,\triangle_y)d\triangle_x\, d\triangle_y, \qquad (4.1)$$

where $p(x,y,t+T)$ is the population density at the location (x,y) and time $t+T$. Recently we have argued that this evolution equation is also relevant to other biological species besides trees, e.g., humans [83]. However, for the sake of definiteness and clarity, in this paper we will consider trees in our explanations. The time interval T is that between two subsequent dispersal events or "jumps" (in the nonstructured model, T is one generation, i.e., the mean age of trees when they begin to produce seeds). R_0 is the net reproductive rate (number of seeds per parent tree and *year* which survive into an adult tree). Equation (4.1) is the nonoverlapping generations model. It is worth to stress that in this model, the net reproductive rate per *year* is always used for R_0 [12]. The dispersal kernel $\phi(\triangle_x,\triangle_y)$ is the probability per unit area that a particle that a seed falling from a parent tree located at $(x+\triangle_x, y+\triangle_y, t)$ reaches the ground at $(x,y,t+T)$. Strictly, Eq. (4.1) is valid only at sufficiently low values of the population density p, because there is a maximum saturation density above which net reproduction vanishes (see Eq. (9) in Ref. [83]); however, this point does not affect the computation of front speeds because, as we shall see below, such computations can be performed at low values of p.

Equation (4.1) is a continuous space random walk (CSRW) equation in two dimensions. It is just an integration over all possible jumps, which takes into account the probability of each possible jump [dispersal kernel $\phi(\triangle_x, \triangle_y)$] as well as the productivity of new individuals (net reproduction rate R_0).

Let us first summarize some previous results, and we will then extend them to more general situations. The speed of fronts evolving according to Eq. (4.1) can be obtained under some general assumptions, as follows [15, 84]. We assume that $R_0 > 1$, that the initial population density has bounded support [i.e., that $p(x, y, t)$ vanishes outside a finite region], and that for $t \to \infty$ the front becomes approximately planar at scales much larger than that of individual dispersal events. Then we can choose the x axis parallel to the local velocity of the front (i.e., $c \equiv |c_x|$ and $c_y = 0$). Finally, we look for constant-shape solutions with the form $p = p_0 \exp[-\lambda(x - ct)]$ at $x - ct \to \infty$ (leading edge of the invasion front). Requiring that $\lambda > 0$ yields the asymptotic ($t \to \infty$) front speed for 2D nonstructured populations [15, 84],

$$c = \min_{\lambda>0} \frac{\ln [R_0 \ \widehat{\varphi}(\lambda)]}{\lambda T}, \tag{4.2}$$

where

$$\widehat{\varphi}(\lambda) \equiv \int_0^\infty d\Delta \ \varphi(\Delta) \ I_0(\lambda\Delta), \tag{4.3}$$

and

$$I_0(\lambda\Delta) \equiv \frac{1}{2\pi} \int_0^{2\pi} d\theta \ \ \exp [\lambda\Delta \cos\theta] \tag{4.4}$$

is the modified Bessel function of the first kind and order zero. The dispersal probability per unit area $\phi(\triangle)$ is related to that per unit length $\varphi(\Delta)$ (i.e., into a 2D ring of area $2\pi\Delta \ d\Delta$) according to [15]

$$\varphi(\Delta) = 2\pi\Delta\phi(\Delta). \tag{4.5}$$

We have also assumed an isotropic dispersion kernel (i.e., that ϕ depends only on distance $\Delta \equiv \sqrt{\triangle_x^2 + \triangle_y^2}$), and applied the normalization of probability, i.e.,

$$\int_0^\infty d\Delta\varphi(\Delta) = 1. \tag{4.6}$$

4.2.2 Structured populations in two dimensions

In the previous section we have summarized the nonstructured (or nonoverlapping) model in two dimensions [15,84]. It is widely used because of its mathematical simplicity (let us mention that it has been often formulated in one dimension [12,84], because then it becomes even simpler). But obviously, assuming that individuals reproduce only once in their lifetime is not a good approximation in general. Indeed, trees produce new seeds during many years. Thus we should expect intuitively that multiple reproduction events will lead to faster values of the front speed (and, in some cases, even prevent the

extinction of the population). For these reasons, we have built a model that makes it possible to predict front speeds for structured populations spreading across 2D space.

Introductory example

Let us use a simple example to introduce the main assumptions and equations of our 2D overlapping model. Consider a species with a life span of three years. If one-year-old individuals cannot produce seeds, in the nonstructured model $T = 2$ yr. Thus, the limitation of the nonstructured model (4.1) is that it does not take into account the reproduction of three-year-old individuals in this simple example.

Let us assume that reproduction events take place only once per year (this is valid for most tree species, as seed production happens only during some period in fall). In order to compute the production of new individuals, we have to take into account the contribution of both the two-year-old and the three-year-old subpopulations. Therefore,

$$\begin{aligned} p_1(x, y, t+1) = R_{02} \int \phi_2(\Delta_x, \Delta_y) p_2(x + \Delta_x, y + \Delta_y, t) d\Delta_x d\Delta_y \\ + R_{03} \int \phi_3(\Delta_x, \Delta_y) p_3(x + \Delta_x, y + \Delta_y, t) d\Delta_x d\Delta_y, \end{aligned} \tag{4.7}$$

where $p_1(x, y, t+1)$ is the population density of one-year-old individuals at location (x, y) and time $t + 1$ (time is measured in years). The right-hand-side of Eq. (4.7) contains two terms. The first one is the contribution of two-year-old individuals. One can easily observe that this term is analogous to Eq. (4.1): R_{02} is the net reproductive rate of two-year-old individuals, $\phi_2(\Delta_x, \Delta_y)$ is the dispersal kernel, and $p_2(x + \Delta_x, y + \Delta_y, t)$ is the two-year-old population density at location $(x + \Delta_x, y + \Delta_y)$ and time t. Similarly, the last term describes the reproduction and dispersal of seeds produced by three-year-old individuals. In order to predict the invasion speed, we need to know the population densities of adult individuals in future times. These population densities are governed by the following equations:

$$p_2(x, y, t + 1) = p_1(x, y, t), \tag{4.8}$$

$$p_3(x, y, t + 1) = p_2(x, y, t), \tag{4.9}$$

because in this model, for simplicity, we neglect the effect of deaths in subpopulations 1 and 2 (i.e., all one-year-old individuals will be two years old after one year has elapsed, etc.). Finally we have the following set of equations that describes our structured population:

$$\begin{aligned} p_1(x, y, t + 1) = \int R_0 \phi(\Delta_x, \Delta_y) p_2(x + \Delta_x, y + \Delta_y, t) d\Delta_x d\Delta_y \\ + \int R_0 \phi(\Delta_x, \Delta_y) p_3(x + \Delta_x, y + \Delta_y, t) d\Delta_x d\Delta_y \\ p_2(x, y, t + 1) = p_1(x, y, t) \\ p_3(x, y, t + 1) = p_2(x, y, t). \end{aligned} \tag{4.10}$$

For simplicity, here we have assumed that the net reproductive rate and the dispersal kernel of two- and three-year-old individuals are the same. Similarly to the nonstructured model, we look for constant-shape solutions, but now for each subpopulation, i.e., $p_1(x,y,t) = w_1 \exp[-\lambda(x-ct)]$, $p_2(x,y,t) = w_2 \exp[-\lambda(x-ct)]$, $p_3(x,y,t) = w_3 \exp[-\lambda(x-ct)]$. Then we can rewrite Eq. (4.10) as

$$\begin{gathered} w_1 \exp(\lambda c) = R_0 w_2 \int_0^\infty \varphi(\Delta) I_0(\lambda\Delta)\Delta d\Delta + R_0 w_3 \int_0^\infty \varphi(\Delta) I_0(\lambda\Delta)\Delta d\Delta \\ w_2 \exp(\lambda c) = w_1 \\ w_3 \exp(\lambda c) = w_2, \end{gathered} \tag{4.11}$$

where $I_0(\lambda\Delta)$ and $\varphi(\Delta)$ are defined by Eqs. (4.4)-(4.5). If w_1, w_2, and w_3 are thought of as the entries of a array $\overrightarrow{w} = \begin{pmatrix} w_1 \\ w_2 \\ w_3 \end{pmatrix}$, then the system (4.11) can be rewritten as

$$\exp(\lambda c)\vec{w} \equiv \overrightarrow{\overrightarrow{H}}(\lambda)\vec{w}, \tag{4.12}$$

where $\overrightarrow{\overrightarrow{H}}(\lambda)$ is the matrix

$$\overrightarrow{\overrightarrow{H}}(\lambda) = \begin{pmatrix} 0 & R_0 \int_0^\infty \varphi(\Delta) I_0(\lambda\Delta)\Delta d\Delta & R_0 \int_0^\infty \varphi(\Delta) I_0(\lambda\Delta)\Delta d\Delta \\ 1 & 0 & 0 \\ 0 & 1 & 0 \end{pmatrix}. \tag{4.13}$$

It is well known that the front speed c for systems with the form (4.12) can be obtained from [19]

$$c = \min_{\lambda>0} \frac{\ln[\rho_1(\lambda)]}{\lambda}, \tag{4.14}$$

where ρ_1 is the largest of the eigenvalues of $\overrightarrow{\overrightarrow{H}}(\lambda)$.

Equation (4.14) is the result for the front speed of structured populations in two dimensions. Some results exist in one dimension [19], but in that case the Bessel function $I_0(\lambda\Delta)$ does not appear at all and the solutions are rather different. Indeed, in order to compare the one- and two-dimensional models, below we present the main one-dimensional (1D) equations and we assign some hypothetical values to the parameters.

In one dimension, clearly the kernel per unit area $\phi(\triangle_x, \triangle_y)$ has no physical meaning. The 1D evolution equation [equivalent to Eq. (4.1)] is obviously:

$$p(x, t+T) = R_0 \int_{-\infty}^{+\infty} p(x+\triangle_x, t)\widetilde{\varphi}(\triangle_x) d\triangle_x \ , \tag{4.15}$$

where we have not used the notation $\varphi(\Delta)$ for the kernel in order to avoid confusion with the 2D model. Let us assume a very simple dispersal kernel so that seeds can be only

dispersed at a specific distance Δ_0 (with probability $\frac{1}{2}(1-p_e)$ along each direction of propagation) or not dispersed at all (with probability p_e, which is called the persistence),

$$\widetilde{\varphi}(\triangle_x) = p_e\ \delta(\Delta_x) + \frac{1}{2}(1-p_e)\ \delta(\Delta_x - \Delta_0) + \frac{1}{2}(1-p_e)\ \delta(\Delta_x + \Delta_0) \tag{4.16}$$

where $\delta(\Delta_x)$ is the 1D Dirac delta. It is easy to extend Eqs. (4.15) and (4.16) to the overlapping case by performing the same steps as in the 2D example above (i.e., assuming a three-stage population, looking for constant-shape solutions $p_i(x,y,t) = w_i \exp[-\lambda(x-ct)]$, etc.). This yields

$$h_{ij}^{1D} = \begin{cases} R_0 \left[\begin{array}{c} p_e + \frac{1}{2}(1-p_e)\exp(-\lambda\Delta_0) \\ +\frac{1}{2}(1-p_e)\exp(\lambda\Delta_0) \end{array} \right] \text{if } i=1,\ j=2,3 \\ 1 \quad \text{if } i=2, j=1 \\ 1 \quad \text{if } i=3, j=2 \\ 0 \quad \text{elsewhere,} \end{cases} \tag{4.17}$$

where h_{ij}^{1D} are the elements of the matrix $\overrightarrow{\overrightarrow{H_{1D}}}(\lambda)$. Such a matrix is the analog to Eq. (4.13), but now describing one-dimensional spread [76–82]. Instead of the 2D Eq. (4.14), we obtain for the speed of the front in one dimension

$$c_{1D} = \min_{\lambda>0} \frac{\ln\left[\rho_{1D}(\lambda)\right]}{\lambda}, \tag{4.18}$$

where ρ_{1D} is the largest of the eigenvalues of $\overrightarrow{\overrightarrow{H_{1D}}}(\lambda)$.

In order to compare to this 1D invasion speed, in two dimensions we also consider a kernel corresponding to isotropic jumps at a single distance $\Delta = \Delta_0$,

$$\varphi(\triangle) = p_e\ \delta(\Delta) + (1-p_e)\ \delta(\Delta - \Delta_0), \tag{4.19}$$

and the dispersal kernel (4.19) must be introduced in $\overrightarrow{\overrightarrow{H}}(\lambda)$ [see Eq. (4.13)] in order to solve the 2D invasion speed.

In order to present some estimates of the 1D and 2D speeds, let us assign some reasonable numerical values to the parameters [15]. We assume that the typical jump distance of our hypothetical species is $\Delta_0 = 100$ m. We take the value of 0.98 for the probability p_e (i.e., the probability that a seed is dispersed 100 m away from its parent tree is 2%). Then, Table 4.1 shows 1D and 2D front speeds [obtained by solving Eq. (4.18) and (4.14), respectively] for several values of R_0.

It is seen from Table 4.1 that the 1D model leads to an overestimation of the 2D speeds, and the overestimation is more important for low values of R_0. This justifies the need to tackle the 2D case for nonoverlapping generations, as first done in the present paper. Still, Eq. (4.14) holds only for populations with a life span of 3 years. Below we tackle the general case of an arbitrary number of years n, and apply it to an example.

R_0	c_{1D}	c	$Error\ (\%)$
4	30.8	24.4	20.7
10	39.6	32.5	17.9
40	48.4	40.7	15.9

Table 4.1: Front speeds in one and two dimensions (in m/yr) and the error of the 1D speed (relative to the 2D speed c) for an example with n=3 stages and several values of the net fecundity R_0 [measured in seeds/(tree $\cdot$ yr)].

Spread of structured populations in two dimensions

In this section we generalize the introductory example (presented above) to deal with a population structured into n subpopulations. Although we apply the method to tree species, our model can be extended to other invasive species (like animals). Then one should take into account some specific features (e.g., the fact that for trees dispersal is simultaneous with reproduction) and make new assumptions (e.g., for birds dispersal is more frequent in young individuals), but we plan to tackle such cases in future work. The main point here is to note that building the *reaction-dispersal matrix* $\overrightarrow{\overrightarrow{H}}(\lambda)$ is an important step in order to solve the front speed problem. In the following lines we explain how to obtain the matrix $\overrightarrow{\overrightarrow{H}}(\lambda)$ by using two simpler matrices. At the end of the section we will use the reaction-dispersal matrix to find a new, general equation for the invasion speed of structured populations in two dimensions.

In order to introduce the notation, let us first return to our simple example (three-stage system). If dispersal were not present, obviously

$$\begin{array}{c} p_1(x,y,t+1) = R_0 p_2(x,y,t) \\ +R_0 p_3(x,y,t) \\ p_2(x,y,t+1) = p_1(x,y,t) \\ p_3(x,y,t+1) = p_2(x,y,t), \end{array} \tag{4.20}$$

and Eq. (4.20) would provide the population dynamics of the three stages, governed only by reproduction. Using a simpler notation,

$$\overrightarrow{p}(x,y,t+1) = \overrightarrow{\overrightarrow{A}}\,\overrightarrow{p}(x,y,t), \tag{4.21}$$

Where $\overrightarrow{p}(x,y,t) = \begin{pmatrix} p_1(x,y,t) \\ p_2(x,y,t) \\ p_3(x,y,t) \end{pmatrix}$. From Eq. (4.20),

$$\overrightarrow{\overrightarrow{A}} = \begin{pmatrix} 0 & R_0 & R_0 \\ 1 & 0 & 0 \\ 0 & 1 & 0 \end{pmatrix}. \tag{4.22}$$

$\overrightarrow{\overrightarrow{A}}$ can be called the demographic matrix. Element a_{ij} of this matrix represents the rate at which an individual in state j gives rise to individuals in state i per unit time (in

this case one year). For example, element $a_{12} = R_0$ is the productivity of new (one-year old) individuals from a two-year old individual. $a_{32} = 1$ means that all two-year-old individuals will be three years old a year later (and similarly for $a_{21} = 1$). The zeros of the matrix represent the transitions that are forbidden under our assumptions. For example, $a_{23} = 0$ because a three-year old individual will never become neither produce a two-year-old individual a year later.

Let us now add stage-specific dispersal into this description. Similarly to 1D studies [19, 85], we introduce $\phi_{ij}(\Delta_x, \Delta_y)$ as the probability that an individual making the transition from stage i to stage j moves from location $(x + \Delta_x, y + \Delta_y)$ to location (x, y). If there is no dispersal during a given transition, the associated kernel is the 2D Dirac delta function.

Instead of Eq. (4.20), taking into account dispersal events we obtain the set

$$p_i(x, y, t + 1) = \int_{-\infty}^{+\infty} \sum_{j=1}^{3} \phi_{ij}(\Delta_x, \Delta_y) a_{ij} p_j(x + \Delta_x, y + \Delta_y, t) d\Delta_x d\Delta_y, \tag{4.23}$$

with $i = 1, 2, 3$. Again, the notation can be simplified by creating a dispersal matrix $\overrightarrow{\overrightarrow{\Phi}}$. In our example,

$$\overrightarrow{\overrightarrow{\Phi}} = \begin{pmatrix} \delta_{2D}(\Delta) & \phi(\Delta_x, \Delta_y) & \phi(\Delta_x, \Delta_y) \\ \delta_{2D}(\Delta) & \delta_{2D}(\Delta) & \delta_{2D}(\Delta) \\ \delta_{2D}(\Delta) & \delta_{2D}(\Delta) & \delta_{2D}(\Delta) \end{pmatrix}. \tag{4.24}$$

We can now rewrite Eq. (4.23) in vector form,

$$\overrightarrow{p}((x, y, t + 1) = \int_{-\infty}^{+\infty} \overrightarrow{\overrightarrow{\Phi}} \circ \overrightarrow{\overrightarrow{A}}\ \overrightarrow{p}(x + \Delta_x, y + \Delta_y, t) d\Delta_x d\Delta_y, \tag{4.25}$$

where the symbol $\circ$ stands for the Hadamard product [86], i.e., $\left(\overrightarrow{\overrightarrow{\Phi}} \circ \overrightarrow{\overrightarrow{A}}\right)_{ij} = \phi_{ij}\ a_{ij}$. It is very important to note that Eq. (4.25) remains valid if we extend our study to a population with a larger number of stages (say, n stages). In this case, the matrices $\overrightarrow{\overrightarrow{\Phi}}$ and $\overrightarrow{\overrightarrow{A}}$ are both square matrices of order n. This is the general case we will now deal with.

For each subpopulation, we look for constant-shape solutions (e.g., $p_i(x, y, t) = w_i \exp[-\lambda(x - ct)]$, as in the example above). Whereas in the three-stage population (considered above) using this into Eq. (4.25) leads to Eq. (4.11), in the general case of n stages we obtain

$$\exp(\lambda c)\overrightarrow{w} = \left(\int_{-\infty}^{+\infty} \overrightarrow{\overrightarrow{\Phi}} \circ \overrightarrow{\overrightarrow{A}}\ \exp\left[-\lambda \Delta \cos\theta\right]\ d\Delta d\theta \right) \overrightarrow{w}\ . \tag{4.26}$$

Assuming an isotropic dispersal kernel, Eq. (6.13) can be written as

$$\exp(\lambda c)\overrightarrow{w} = \left(2\pi \int_{0}^{+\infty} \overrightarrow{\overrightarrow{\Phi}} \circ \overrightarrow{\overrightarrow{A}}\ I_0(\lambda \Delta)\ d\Delta \right) \overrightarrow{w}, \tag{4.27}$$

where $I_0(\lambda\Delta)$ stands for the modified Bessel function of the first kind and order zero [Eq. (4.4)].

It is easy to see that the matrix inside the brackets in the right-hand side of Eq. (6.13) becomes, for $n = 3$, the matrix $\overrightarrow{\overrightarrow{H}}(\lambda)$ given by Eq. (4.13). We define generally $\overrightarrow{\overrightarrow{H}}(\lambda)$ as

$$\overrightarrow{\overrightarrow{H}}(\lambda) \equiv 2\pi \int_0^{+\infty} \overrightarrow{\overrightarrow{\Phi}} \circ \overrightarrow{\overrightarrow{A}}\ I_0(\lambda\Delta)\ d\Delta. \tag{4.28}$$

Then we can rewrite Eq. (6.13) as

$$\exp(\lambda c)\vec{w} \equiv \overrightarrow{\overrightarrow{H}}(\lambda)\vec{w}, \tag{4.29}$$

and, as mentioned above, the solution for the front speed c is [19]

$$c = \min_{\lambda>0} \frac{\ln\left[\rho_1(\lambda)\right]}{\lambda}, \tag{4.30}$$

where ρ_1 is the largest real of the eigenvalues of $\overrightarrow{\overrightarrow{H}}(\lambda)$, which is now given by Eq. (4.28).

This new result is the 2D equivalent to previous results in one dimension [19] for an arbitrary number of stages n. However, we stress that 1D results can be applied only in very special systems (e.g., a population spreading along a coast or a river), but most population invasions on the Earth take place in two dimensions. Therefore, in most cases 1D results cannot be applied. Indeed, the Bessel function $I_0(\lambda\Delta)$ appears in Eq. (4.28), whereas it does not appear at all for populations spreading in one dimension [19]. In Sec. 4.3.2 we present some numerical 1D and 2D overlapping results for a population with a large number of stages.

4.3 Application

In previous sections we have developed a model to calculate front speed for a general case of structured populations in two dimensions. As an example, in this section we will use the matrices in Eq. (4.25) and parameter values appropriate to study a specific tree species, namely, the *yellow poplar (Liriodendron tulipifera).* This species was already considered in Ref. [15], but only by means of a nonoverlapping generation model. Below we apply our overlapping-generations model, and compare to simulations of structured populations. Furthermore, at the end of this paper we will tackle the question of how important the effect of overlapping generations is, by comparing our results with those of the nonoverlapping-generations model [15].

4.3.1 Molecular dynamics simulations

We are not dealing with a differential but with an integrodifference set of equations in two dimensions [Eq. (4.25)]. Therefore, numerical simulations in this paper will not be

based on finite-step approximations to partial derivatives but on molecular dynamics. We have performed simulations on a 2D grid, with nearest neighbors separated by a distance Δ_0. Initially $p(x, y, 0) = 1$ at $(x, y) = (0, 0)$ and $p(x, y, 0) = 0$ elsewhere. At each time step, we compute the new number density of trees $p(x, y, t + 1)$ at all nodes of the grid as follows.

First of all, because of the structure of the population, not all of the individuals can produce seeds. We need to distinguish the adult population (i.e., individuals that take a role in a reproduction event) from juvenile individuals (i.e., those that cannot yet produce seeds). In order to do so, we introduce a second field $j(x, y, t)$ that accounts for the juvenile individuals. While the first field accounts for the total population density [i.e., $p(x, y, t)$ includes juveniles and adults], the second one contains only the juvenile population density $j(x, y, t)$. The number of individuals being available to reproduce [namely $a(x, y, t)$] is simply the difference between $p(x, y, t)$ and $j(x, y, t)$. In each time step (or iteration), our computer program calculates the seed production $R_0\, a(x, y, t)$ at every node and then redistributes this value among all grid nodes by using the dispersal kernel. Moreover, we also take into account when an individual is too old to be fertile (i.e., when it reaches the typical life span l of the species considered). This is done by removing such individuals from the calculations after each time step (i.e., after each year).

We will focus our attention on the effects of the population structure (in order to solve the front speed problem), instead of studying complicated dispersal kernels. Therefore, our simulations apply a simple kernel such that, when a seed is produced, it either remains at the same node where it was generated (with a probability p_e) or it is dispersed to one of the four nearest-neighbor nodes located at distance Δ_0 [with probability $(1 - p_e)/4$].

We have performed our 2D simulations by using the typical values measured for the *yellow poplar*, namely life span $l = 130$ yr., age at first reproduction $T = 20$ yr., persistence $p_e = 0.99798$ and characteristic dispersal distance $\Delta_0 = 6000$ m *. The results for the front speed are shown in Fig. 4.1, both along the horizontal and along the diagonal direction of the 2D grid (upper and lower triangles in Fig. 4.1). We also include the average speeds between both directions (circles in Fig. 4.1).

4.3.2 CSRW

In order to study an overlapping-generations front using a 2D CSRW, first we need to determine the order of the matrices in Eq. (4.25). Recall that in our structured-population model, every year of an individual's life is thought of as a different stage.

*According to field observations in sites close to those where the dispersal kernel was measured, we estimate the net reproductive rate R_0 of the *yellow poplar (Liriodendron Tulipifera)* to be in the range of 2-50 seeds/(tree yr.). The age at first reproduction (generation time in the nonstructured model) of the same species is $T = 20$ yr. As shown in [15], the long-distance dispersal component of the kernel has a much more important effect on the front speed than the short-distance component (even if long-distance dispersal happens seldom). Therefore, we use for the distance between cells that from the long-distance component, $\Delta_0 = 6000$ m, both in the CSRW and in the DSRW models.

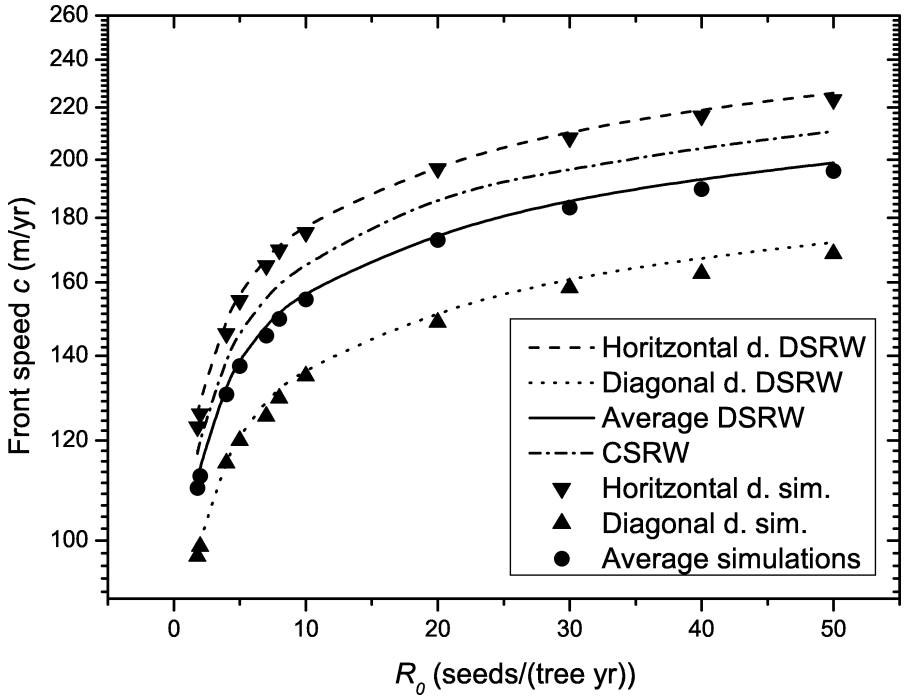

Figure 4.1: Front speed in two dimensions versus net reproductive rate. There are relevant differences between the CSRW and the simulations (above 5%). Because of this, we have also devellopped a DSRW model that agrees correctly with simulations (differences are always under 3%).

From the life span of the *yellow poplar* [†], namely, 130 years, it follows that Eq. (4.25) shall be a system of order 130 [‡]. *Yellow poplar* trees begin to produce seeds when they are 20 years old. Therefore, the demographic matrix $\overrightarrow{\overrightarrow{A}}$ will be

$$a_{ij} = \begin{cases} R_0 \text{ if } i = 1 \text{ and } j \geq 20 \\ 1 \text{ if } i = j + 1 \\ 0 \text{ otherwise.} \end{cases} \tag{4.31}$$

Note that the structure of this matrix is the same as that of Eq. (6.24), with the

[†]See footnote *.

[‡]All of the results in this paper have been calculated with square matrices $\overrightarrow{\overrightarrow{A}}$ and $\overrightarrow{\overrightarrow{\Phi}}$ of order 130. However, we have observed that in many cases we can obtain accurate results using matrices of lower order. That can be very useful in order to reduce computation times. For instance, omitting all of the elements a_{ij} with $i > 65$ and/or $j > 65$, we obtain a demographic matrix of order 65. If we do the same for the dispersal kernel matrix and we solve the equations of our overlapping-generations model, we obtain the same invasion speeds (differences are under the 1%) for values of R_0>5. The reason is that very old individuals do not appear near the leading edge of the invasion front, so for high values of the fecundity R_0 the front dynamics is driven by younger individuals and the contribution of older ones is not relevant. However we do not give a general description of such an approximation because it depends on the dispersal kernel and demographic characteristics of each species.

difference that the matrix (4.31) is of order 130. In order to obtain the dispersal kernel matrix $\overrightarrow{\Phi}$, we recall that, as explained above, the dispersal kernel per unit length reads

$$\varphi(\Delta) = \begin{cases} (1-p_e) \text{ if } \Delta = \Delta_0 \\ p_e \text{ if } \Delta = 0 \\ 0 \text{ otherwise,} \end{cases} \tag{4.32}$$

where Δ_0 and p_e take the typical values of long-distance dispersal and persistence for the *yellow poplar, namely* $p_e = 0.99798$ and $\Delta_0 = 6000m$ [§]. On the other hand,

$$\Phi_{ij} = \begin{cases} \frac{\varphi(\Delta)}{2\pi\Delta} \text{ if } i = 1 \text{ and } j > 20 \\ \delta^{2D}(\Delta) \qquad \text{otherwise,} \end{cases} \tag{4.33}$$

where $\delta^{2D}(\Delta)$ is the Dirac delta function in two dimensions, namely [see Eq. (4.5)]

$$\delta^{2D}(\Delta) = \frac{\delta^{1D}(\Delta)}{2\pi\Delta}, \tag{4.34}$$

and its normalization condition reads

$$\int_0^\infty \int_0^{2\pi} \delta^{2D}(\Delta)\Delta d\Delta d\theta = 1. \tag{4.35}$$

We have used these equations into Eqs. (4.28)-(4.30) to compute invasion speeds for different values of the net reproductive rate R_0. The results are shown in Fig. 4.1. Both the simulations and the CSRW predictions are seen to increase with increasing values of R_0, as it was to be expected intuitively. However, there are some differences (larger than 5%) between the CSRW and the average simulations. This effect is due to the fact that, while the CSRW describes jumps into a ring of radius Δ_0, the numerical simulations describe jumps to four discrete points (i.e., the four nearest neighbors of the grid). The consistency between the analytic and numeric results can be improved by using a discrete-space random-walk model (DSRW). In such an analytical model, seeds and trees can only lie on discrete points of the space (similarly to what happens in the numerical simulations). Recently, a DSRW model for nonstructured (i.e., nonoverlapping) populations of persistence p_e has been proposed [83]. In the next section we will extend that nonoverlapping DSRW model to our structured populations, and we will apply it to the *yellow poplar*.

Before closing this section, a numerical comparison to the 1D overlapping model can be useful. Whereas Sec 4.2.2 and Table 4.1 include such a comparison for three-stage populations, here we present it for a *yellow poplar* population (because it has a large number of stages). Similarly to Eq. (4.17), elements h_{ij}^{1D} of the corresponding yellow poplar $\overrightarrow{\overrightarrow{H_{1D}}}(\lambda)$ matrix take the form

$$h_{ij}^{1D} = \begin{cases} R_0 \left[\begin{array}{c} p_e + \frac{1}{2}(1-p_e)\exp(-\lambda\Delta_0) \\ +\frac{1}{2}(1-p_e)\exp(\lambda\Delta_0) \end{array} \right] \text{ if } i = 1,\ j \geq T \\ 1 \text{ if } i = j+1 \\ 0 \text{ elsewhere,} \end{cases}$$

[§]See footnote *.

R_0	c_{1D}	c	$Error$ (%)
4	164.1	139.8	14.8
10	193.7	165.8	14.4
40	236.8	204.5	13.6

Table 4.2: Front speeds in one and two dimensions (in m/yr) and the error of the 1D speed (relative to the 2D speed c) for n=130 stages (yellow poplar) and several values of the net fecundity R_0 [measured in seeds/(tree $\cdot$ yr)].

and the front speed is given by Eq. (4.18). Using the values of the persistence and jump distance above (i.e., $p_e = 0.99798$ and $\Delta_0 = 6000m$) we have calculated the front speed for several values of R_0. The results are shown in Table 4.2. It follows that for a *yellow poplar* population, the overestimation of the 1D model is still important, but a bit lower than in the three-stage example (Table 4.1). In all cases, the overestimation is always higher than 10% (and it increases for decreasing values of the net reproductive rate). Thus we remark the convenience of using a 2D model, also in the case of populations with large number of stages.

4.3.3 DSRW

Horizontal direction (0^o)

Assuming nonoverlapping generations, the DSRW model corresponds to the following evolution equation [83]

$$p(x,y,t+T) = R_0 \left\{ p_e\ p(x,y,t) + \frac{(1-p_e)}{4} \left[p(x \pm \Delta_0, y, t) + \ p(x, y \pm \Delta_0, t) \right] \right\}. \tag{4.36}$$

In contrast, the dynamics of a population with overlapping generations will be driven by the set

$$\begin{array}{c} p_1(x,y,t+1) = R_0 \sum\limits_{i=T}^{n} \left\{ \begin{array}{l} p_e\ p_i(x,y,t) \\ \ +\frac{(1-p_e)}{4} \left[\begin{array}{c} p_i(x \pm \Delta_0, y, t) \\ +\ p_i(x, y \pm \Delta_0, t) \end{array} \right] \end{array} \right\} \\ p_2(x,y,t+1) = p_1(x,y,t) \\ p_3(x,y,t+1) = p_2(x,y,t) \\ \ldots \\ p_n(x,y,t+1) = p_{n-1}(x,y,t), \end{array} \tag{4.37}$$

where, as in the previous sections, for simplicity we have assumed that all stages have the same reproductive and dispersive behavior, that individuals in stage i will be in stage $i+1$ a year later, which trees cannot reproduce before the so-called generation time T, etc.

As usual, we look for constant-shape solutions with the form $p_i(x,y,t) = w_i \exp[-\lambda(x - ct)]$. We remark that looking for such solutions implies that we will evaluate the speed

of the front along the horizontal direction (i.e., the 0^o direction relative to the x axis). In this way, we obtain the following equations:

$$\begin{array}{c} w_1 \exp(\lambda c) = R_0 \sum_{i=T}^{n} w_i \left[\frac{p_e+1}{2} + \frac{1-p_e}{2}\cosh(\lambda\Delta_0)\right] \\ w_2 \exp(\lambda c) = w_1 \\ w_3 \exp(\lambda c) = w_2 \\ \cdots \\ w_n \exp(\lambda c) = w_{n-1}. \end{array} \tag{4.38}$$

Finally, we use matrix notation to rewrite the system in more compact form,

$$\exp(\lambda c)\vec{w} \equiv \overrightarrow{\overrightarrow{H}}(\lambda)\vec{w}, \tag{4.39}$$

where it is easy to see that the reaction-dispersal matrix of population takes the form

$$h_{ij} = \begin{cases} R_0 \left[\frac{p_e+1}{2} + \frac{1-p_e}{2}\cosh(\lambda\Delta_0)\right] \text{ if } i = 1,\ j \geq T \\ 1 \text{ if } i = j+1 \\ 0 \text{ elsewhere,} \end{cases} \tag{4.40}$$

and the front speed will be found by means of Eq. (4.30).

Diagonal direction (45^o)

We now introduce new coordinate axes (x', y') on the diagonal direction, i.e., X' and Y' axes rotated 45^o with respect to the X and Y axes. Then, for nonoverlapping generations the population density evolves according to [83]

$$p(x', y', t+1) = R_0 \left\{ \begin{array}{c} p_e\ p(x', y', t) \\ +\frac{(1-p_e)}{4}\left[\ p\left(x' + \frac{\Delta_0}{\sqrt{2}}, y' \pm \frac{\Delta_0}{\sqrt{2}}, t\right) + \ p\left(x' - \frac{\Delta_0}{\sqrt{2}}, y' \pm \frac{\Delta_0}{\sqrt{2}}, t\right)\right] \end{array} \right\}. \tag{4.41}$$

However, for overlapping generations we have instead

$$\begin{array}{c} p_1(x', y', t+1) = R_0 \sum_{i=T}^{n} \left\{ \begin{array}{c} p_e\ p_i(x', y', t) \\ +\frac{(1-p_e)}{4}\left[\ p_i\left(x' + \frac{\Delta_0}{\sqrt{2}}, y' \pm \frac{\Delta_0}{\sqrt{2}}, t\right) + \ p_i\left(x' - \frac{\Delta_0}{\sqrt{2}}, y' \pm \frac{\Delta_0}{\sqrt{2}}, t\right)\right] \end{array} \right\} \\ p_2(x', y', t+1) = p_1(x', y', t) \\ p_3(x', y', t+1) = p_2(x', y', t) \\ \cdots \\ p_n(x', y', t+1) = p_{n-1}(x', y', t). \end{array} \tag{4.42}$$

Next, we look for constant-shape solutions, now with the form $p_i(x', y', t) = w_i \exp[-\lambda(x' - ct)]$. We obtain from the set (4.42),

$$
\begin{aligned}
w_1 \exp(\lambda c) &= \sum_{i=T}^{n} w_i R_0 \left[p_e + (1-p_e) \cosh\left(\lambda \tfrac{\Delta_0}{\sqrt{2}} \right) \right] \\
w_2 \exp(\lambda c) &= w_1 \\
w_3 \exp(\lambda c) &= w_2 \\
&\cdots \\
w_n \exp(\lambda c) &= w_{n-1},
\end{aligned}
\tag{4.43}
$$

the corresponding reaction-dispersal matrix takes the form

$$
h_{ij} = \begin{cases} \sum_{i=T}^{n} R_0 \left[p_e + (1-p_e) \cosh\left(\lambda \tfrac{\Delta_0}{\sqrt{2}} \right) \right] & \text{if } i = 1,\ j \geq T \\ 1 \text{ if } i = j+1 \\ 0 \text{ elsewhere,} \end{cases}
\tag{4.44}
$$

and the front speed shall be obtained with the usual procedure [Eq. (4.30)].

In Fig. 4.1, the DSRW calculations have been performed for both the horizontal and the diagonal direction (dashed and dotted curves, respectively). We can see an almost perfect agreement between DSRW and simulations (differences are always under 2% after averaging results along both directions). Thus the DSRW is the model that agrees closer to the simulations, even when overlapping generations are considered. This shows the validity of the simulation results in Fig. 4.1, as well as the origin of the discrepancies between the CSRW and the simulations in Fig. 4.1.

4.4 Nonoverlapping versus overlapping generations model

The nonoverlapping approximation has an obvious advantage, namely, that computation times are much shorter **. Figure 4.2 shows invasion speeds of *yellow poplar* fronts calculated with both the classical, nonoverlapping model and our overlapping model (both in two dimensions). From Fig. 4.2 we see that the behavior of both nonoverlapping (squares) and overlapping (circles) front speeds are similar. As it was expected, the overlapping model yields faster invasion speeds. Actually, both models tend to the same asymptotic speed for very high values of the net reproductive rate ($R_0 \to \infty$). This happens because in the limit $R_0 \to \infty$, the contribution of the youngest individuals able to produce seeds on the front clearly becomes much more important than that from older trees, and that is precisely the main assumption of the nonoverlapping approximation. In contrast, multiple reproduction events have a very important effect on the front speed for lower, realistic values of the net reproductive rate R_0. Figure

**Calculation of each overlapping-DSRW speed in Fig. 4.2 takes about 50 to 80 minutes. We used an Intel Core 2 CPU, T7400 (2,16GHz and 2GB RAM). We remark that calculation times become much longer as the order of the matrix $\overrightarrow{\overrightarrow{H}}$ increases. In contrast, each overlapping-model simulation takes about 10 minutes using the same computer. For nonoverlapping models, calculation times are about ten times shorter than for overlapping models.

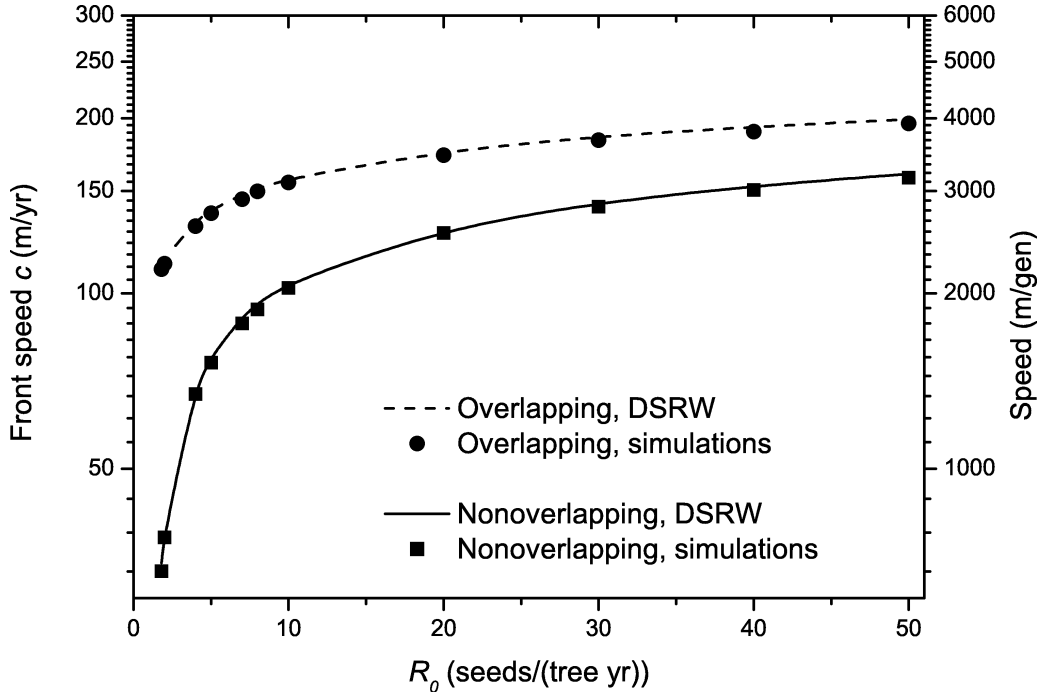

Figure 4.2: Front speed in two dimensions versus net reproductive rate. Both nonoverlapping (squares) and overlapping (circles) DSRW results correspond to the average between the horitzontal and diagonal spread directions (Sec. 4.3.3). Each model agrees perfectly with its corresponding simulations (continuous and dashed lines). The effect of considering overlapping generations becomes more important as lower values of R_0 are considered.

4.2 shows substantial differences between the nonoverlapping and the overlapping case for $2 < R_0 < 10$, which is within a realistic range for the *yellow poplar* ¶. The speed predicted by the classical, nonoverlapping model is less than $\frac{1}{3}$ of that predicted by our overlapping model.

From Fig. 4.2, it is also very interesting that the overlapping-generations effect allows the survival and spread of the population even for $R_0 < 1$ (the precise threshold will of course depend on the features of the species considered), whereas the nonoverlapping model predicts extinction if $R_0 < 1$ [84]. This effect also shows that the overlapping-generations model can be very important to perform realistic predictions on the fate of biological populations. It can also be very useful in more detailed studies involving, e.g., nonsteady or random values of R_0 (simulating climate change, drought, or epidemic episodes), different productivities R_{0i} for each stage i, etc. In contrast, the nonoverlapping model is not suitable to analyze such situations because it will break down as soon as values $R_0 < 1$ are considered.

Concerning Reid's paradox of rapid tree migration, our previous work suggests that it can be solved by taking into account bimodal dispersal kernels (at least, as far as the

¶See footnote *.

order of magnitude of the speed is concerned). The structure of the population, introduced in this paper, makes the overlapping-generations model more realistic. Therefore, we expect its results to be closer to real measurements of, for example, postglacial recolonization fronts (even though such direct comparisons are not yet feasible for a variety of tree species, because of the uncertainties in the measurements of survival rates and dispersal kernels).

4.5 Conclusions

In this paper we have presented a model that considers the effect of overlapping generations (or, more generally, the stage-structure) of populations that spread on a two-dimensional space. Describing such populations with a matrix notation is useful, and notably simpler, in order to solve the equations that drive the reaction-dispersal dynamics. Actually, in Secs. 4.2.2, 4.3.2 and 4.3.3, writing down the reaction-dispersal matrix $\overrightarrow{\overrightarrow{H}}$ is one of the main steps in the resolution of the front speed problem. This reaction-dispersal matrix contains all of the information concerning the population (i.e., parameters such as the persistence, stage-to-stage transitions, characteristic dispersal distance, etc.) necessary to apply Eq. (4.30) to a specific species and, thus, to obtain its front speed. Generally, the construction of two simpler matrices (namely the demographic matrix and the dispersal one) is quite useful to create the reaction-dispersal matrix (as it is done for the CSRW in Sec. 4.3.2). However, in some cases it is easier to develop the $\overrightarrow{\overrightarrow{H}}$ matrix directly from the description of the population. That is the case of the DSRW explained in Sec. 4.3.3.

Figure 4.1 shows remarkable differences between the CSRW analytical results and the corresponding molecular-dynamics simulations. The same problem was solved previously in the nonoverlapping case using the DSRW description [83]. Therefore, in Sec. 4.3.3 we have extended the DSRW to the overlapping case, obtaining an almost perfect agreement with the simulations (see Fig. 4.1).

We have compared the nonoverlapping and the overlapping models (Fig. 4.2.) Overlapping-generations fronts are always faster than nonoverlapping ones (except in the limit $R_0 \to \infty$). The overlapping-generations approximation can seriously underestimate the speed. Indeed, for realistic parameter values, the speed predicted by the classical, nonoverlapping model is less than $\frac{1}{3}$ of that predicted by our overlapping model. This shows the interest of the problem solved in the present paper. It is also important that the nonoverlapping-generations approximation can wrongly predict extinction for low values of the net reproductive rate R_0. Our 2D overlapping-generations model can be easily extended to describe more complicated situations that cannot the tackled within the nonoverlapping approximation (e.g., a net reproductive rate R_0 that decreases with increasing age of individuals), so future works could report a variety of new applications of the results reported in the present paper.

4.6 Acknowledgements

Funded by European Commission under Grant No. 28192-FEPRE, MICINN under Grant No. FIS-2009-13050, and Generalitat de Catalunya under Grant No. 2009-SGR-374.

Chapter 5

Virus infection speeds: Theory versus experiment

This chapter is an exact transcription of the contents of the following paper:

Amor, D. R. & Fort, J. 2010 Virus infection speeds: Theory versus experiment. *Phys. Rev. E* 82, 061905.

Abstract In order to explain the speed of Vesicular Stomatitis Virus (VSV) infections, we develop a simple model that improves previous approaches to the propagation of virus infections. For VSV infections, we find that the delay time elapsed between the adsorption of a viral particle into a cell and the release of its progeny has a very important effect. Moreover, this delay time makes the adsorption rate essentially irrelevant in order to predict VSV infection speeds. Numerical simulations are in agreement with the analytical results. Our model satisfactorily explains the experimentally-measured speeds of VSV infections.

PACS numbers: 87.23.Cc, 89.20.−a, 89.75.Fb

5.1 Introduction

Mathematical models of infectious diseases are a field that has advanced substantially during the last decades [5]. It makes use of many methods from Physics, e.g., reaction-diffusion equations and front speed computations. On the other hand, in the last century vaccination has become one of the best tools against infection spreading, and some models including vaccination strategies have been developed recently [87,88]. Moreover, new computer technology advances have played an important role on infection spreading research, since they have made it possible to introduce novel methods such as complex networks [89–91]. However, in addition with macroscopic epidemiology studies [5, 87, 88, 90], the effects of infectious diseases at a cellular levels (as well as microscopic viral infection front propagation) are also of scientific interest [22, 92–96].

When a virus infects a cell, some time τ elapses before the new generation of viruses is released from the cell. Some years ago, it was shown that this delay time τ has an

important effect and can satisfactory explain the infection front speeds of T7 viruses infecting *E. Coli* bacteria [10, 20, 21]. In Ref. [21], we mentioned that it should be possible to apply the same model to Vesicular Stomatitis Viruses (VSV), which replicate on mammalian or insect cells (not on bacteria), because there is again a delay due to the time elapsed between virus adsorption into a cell and the release of its progeny. Detailed measurements of infection front speeds for VSV were not available when we developed our models [10, 92], but such measurements have been performed recently [23, 58].

Some very recent models for the spread of VSV infections have been proposed by Haseltine et al. [23]. Their models include the reaction-diffusion process, as well as some additional relevant biological phenomena, in order to explain the experimental images of this phenomenon. In this paper we revisit the approach by Haseltine et al. [23] to reduce the complexity of the models, and to better account for the experimental speeds. We will present a simple model, using as few unknown parameters as possible, and compare its predicted front speeds to VSV experimental data [58]. We will show that it is necessary to take it into account the effect of the delay time τ in order to explain properly the front speeds of VSV infections.

The plan of this paper is as follows. In Sec. 5.2 we present a time-delayed model using as few free or adjustable parameters as possible. In Sec. 5.3 we derive some approximate explicit equations for the front speed. In Sec. 5.4, we perform numerical simulations to check the validity of our theoretical model. In Sec. 5.5 we compare to experimental data. Section 5.6 is devoted to concluding remarks, especially the importance of the delay time τ for VSV infections. We will also find that this delay-time effect leads to the front speed being approximately independent of the adsorption constant k_1 over four orders of magnitude. This is very important in order to compare predicted speeds to experimental ones, because the value of k_1 is very uncertain.

5.2 Model

The infection and virus replication processes can be summarized by the reactions

$$V + C \stackrel{k_1}{\rightarrow} I \stackrel{k_2}{\rightarrow} YV. \tag{5.1}$$

In Eq. (5.1), k_1 is the adsorption rate of viruses V into uninfected cells C, k_2 is the rate constant for the death of infected cells I, and the yield Y is the number of new viruses produced per infected cell. In contrast to some previous papers [10, 20, 21, 92], here we use the symbol C instead of B because VSV infections propagate on mammalian or insect cells (not on bacteria, in contrast to T7 infections).

The experiments reported in Refs. [23, 58] were performed in agar, such that cells are immobilized and only viruses diffuse. The extracellular model by Haseltine et al. [see Eq. (5a) in Ref. [23]] uses the following reaction-diffusion equations for the concentrations at large infected distances, $r \rightarrow \infty$ (where $r = 0$ corresponds to the

initial inoculation point of viruses into a medium of uninfected cells)*,†,

$$\frac{\partial[V](r,t)}{\partial t} = D\frac{\partial^2[V](r,t)}{\partial r^2} - k_1[V][C](r,t) + k_2 Y[I](r,t), \tag{5.2}$$

$$\frac{\partial[C](r,t)}{\partial t} = -k_1[C](r,t)[V](r,t), \tag{5.3}$$

$$\frac{\partial[I](r,t)}{\partial t} = k_1[V](r,t)[C](r,t) - k_2[I](r,t), \tag{5.4}$$

where D is the diffusion coefficient, [...] denotes concentration and t is the time. The set of Eqs. (5.2)−(5.4) can be further improved for two reasons, which we now discuss.

First, Eq. (5.4) implies a virus dynamics that does not agree with experimental data in homogeneous media [see Eq. (5.37) and the text below it in Appendix A‡]. In order to improve this point, it has been proposed [10] that $k_2[I](r,t)$ in Eqs. (5.2) and (5.4) should be replaced by a logistic-type growth function, namely, $k_2[I](r,t)\left\{1-[I](r,t)/I_{MAX}\right\}$, which leads to a virus dynamics that agrees very well with one-step growth experimental data (see Appendix A). Such an improved model is therefore described, instead of by Eqs. (5.2)−(5.4), by the following set:

$$\frac{\partial[V](r,t)}{\partial t} = D\frac{\partial^2[V](r,t)}{\partial r^2} - k_1[V][C](r,t) + k_2 Y[I](r,t)\left(1-\frac{[I](r,t)}{I_{MAX}}\right), \tag{5.5}$$

$$\frac{\partial[C](r,t)}{\partial t} = -k_1[C](r,t)[V](r,t), \tag{5.6}$$

$$\frac{\partial[I](r,t)}{\partial t} = k_1[V](r,t)[C](r,t) - k_2[I](r,t)\left(1-\frac{[I](r,t)}{I_{MAX}}\right). \tag{5.7}$$

This set is more reasonable than Eqs. (5.2)−(5.4), because it agrees better with experimental data in homogeneous media (see Appendix A), but we would like to stress that this point does not affect the analytical results in the present paper, because the infection speeds that we will derive would be the same if the last term in Eqs. (5.5) and (5.7) were neglected (see Appendix A).

A second, much more important improvement can be made. The diffusion dynamics in both Eqs. (5.5) and (5.2) (left side and first term in the right side) is Fickian or nondelayed. This means that it does not take into account the effect of the time interval τ during which a virus does not move appreciably because it is inside a cell.

*The Laplacian is $\frac{\partial^2[V](r,t)}{\partial x^2}+\frac{\partial^2[V](r,t)}{\partial y^2} = \frac{1}{r}\frac{\partial}{\partial r}\left(r\frac{\partial[V](r,t)}{\partial r}\right) = \frac{1}{r}\frac{\partial[V](r,t)}{\partial r}+\frac{\partial^2[V](r,t)}{\partial r^2}$, but since we are interested in the asymptotic front speed ($r\to\infty$ and $t\to\infty$) this simplifies into $\frac{\partial^2[V](r,t)}{\partial r^2}$.

†We try to avoid using unnecessary parameters to explain the experimental front speeds, so we neglect the effects of (i) the reproduction of uninfected cells [i.e., we use $k_3=0$ in Eq. (5b) in Ref. [23], as in the *extracellular model with no growth* in Table 3 in that reference], (ii) the decay of dead cells [$k_4=0$ in Eq. (5d) in [23]], (iii) age dependencies, etc.

‡The appendixes to which the published version of this work refers as appendixes A and B correspond to the sections 5.7 and 5.8, respectively, in this chapter.

The parameter τ is the time interval elapsed from the adsorption of a virus into a cell until the virus has reproduced inside it and the virus progeny have left the cell. Obviously, this effect will slow down the propagation of virus fronts. Indeed, it has been previously shown that taking into account this delay time is essential to find good agreement with the experimental observations in other kinds of virus infections [10]. For this reason, Eq. (5.5) must be replaced by a time-delayed diffusion equation [97], namely, (see Appendix B for a derivation)

$$\frac{\partial [V](r,t)}{\partial t} + \frac{\tau}{2}\frac{\partial^2 [V](r,t)}{\partial t^2} = D\frac{\partial^2 [V](r,t)}{\partial r^2} + F(r,t) + \frac{\tau}{2}\left.\frac{\partial F(r,t)}{\partial t}\right|_g , \tag{5.8}$$

where the virus growth function $F(r,t)$ accounts for all growth processes affecting the virus population density $[V]$, i.e.,

$$F(r,t) \equiv \left.\frac{\partial [V](r,t)}{\partial t}\right|_g = -k_1 [V](r,t)[C](r,t) + k_2 Y [I](r,t)\left(1 - \frac{[I](r,t)}{I_{MAX}}\right). \tag{5.9}$$

Note that Eq. (5.8) simplifies to Eq. (5.5) if the effect of the delay time is neglected ($\tau = 0$).

The symbol $...|_g$ indicates that the corresponding time derivatives in Eqs. (5.8) and (5.9) take into account exclusively growth (i.e., reactive) but not diffusive processes. In a recent paper [43] it has been shown that taking this subindex properly into account improves previous results [9] for the speed of fronts (albeit Refs. [9, 43] consider a simpler system with a single species, whereas here we have three species). For this very same reason, Eq. (5.8) here improves Eq. (6) in Ref. [10], and yields a different infection speed that will be derived below. In order to do so, let us further develop the last term in Eq. (5.8),

$$\left.\frac{\tau}{2}\frac{\partial F(r,t)}{\partial t}\right|_g = -\frac{\tau}{2}k_1 \left.\frac{\partial \left\{[V](r,t)[C](r,t)\right\}}{\partial t}\right|_g + \frac{\tau}{2}k_2 Y \left.\frac{\partial}{\partial t}\left[[I](r,t)\left(1 - \frac{[I](r,t)}{I_{MAX}}\right)\right]\right|_g . \tag{5.10}$$

From Eqs. (5.6) and (5.7), we can see that there are no diffusive processes affecting the time derivatives of neither uninfected C nor infected cells I (physically, this is due to the fact that cells are immobilized in agar in these experiments). Thus, in fact the symbol $...|_g$ is not required for the last term in Eq. (5.10), and the first term on the right can be written as $-\frac{\tau}{2}k_1[V]\ \partial[C]/\partial t\ -\frac{\tau}{2}k_1[C]\ \partial[V]/\partial t|_g$. Making use of Eq. (5.9), this allows us to rewrite Eq. (5.8) as

$$\begin{aligned}\frac{\partial [V](r,t)}{\partial t} + \frac{\tau}{2}\frac{\partial^2 [V](r,t)}{\partial t^2} &= D\frac{\partial^2 [V](r,t)}{\partial r^2} + F(r,t) \\ &- \frac{\tau}{2}k_1 [V](r,t)\frac{\partial [C](r,t)}{\partial t} - \frac{\tau}{2}k_1 [C](r,t)F(r,t) \\ &+ \frac{\tau}{2}k_2 Y \frac{\partial}{\partial t}\left[[I](r,t)\left(1 - \frac{[I](r,t)}{I_{MAX}}\right)\right].\end{aligned} \tag{5.11}$$

This equation has three dependent variables, namely $[V](r,t)$, $[C](r,t)$ and $[I](r,t)$, so in order to analyze its solutions we need two additional equations, namely, Eqs. (5.6) and (5.7),

$$\frac{\partial[C](r,t)}{\partial t} = -k_1[C](r,t)[V](r,t), \tag{5.12}$$

$$\frac{\partial[I](r,t)}{\partial t} = k_1[V](r,t)[C](r,t) - k_2[I](r,t)\left(1 - \frac{[I](r,t)}{I_{MAX}}\right). \tag{5.13}$$

Our model will be based on the set of Eqs. (5.11)−(5.13). Before going ahead, however, we can see better the importance of the symbol $...|_g$ by noting that, if it had not been included in Eq. (5.8), Eq. (5.10) would be the same but without the symbols $...|_g$, so its first term on the right would be $-\frac{\tau}{2}k_1\left([V]\partial[C]/\partial t + [C]\partial[V]/\partial t\right)$ and, since the symbol $...|_g$ does not appear, we would be unable to substitute Eq. (5.9). Therefore, instead of Eq. (5.11) we would have obtained

$$\begin{aligned}\frac{\partial[V](r,t)}{\partial t} + \frac{\tau}{2}\frac{\partial^2[V](r,t)}{\partial t^2} &= D\frac{\partial^2[V](r,t)}{\partial r^2} + F(r,t) \\ &- \frac{\tau}{2}k_1[V](r,t)\frac{\partial[C](r,t)}{\partial t} \; - \frac{\tau}{2}k_1[C]\frac{\partial[V](r,t)}{\partial t} \\ &+ \frac{\tau}{2}k_2 Y\frac{\partial}{\partial t}\left[[I](r,t)\left(1 - \frac{[I](r,t)}{I_{MAX}}\right)\right].\end{aligned} \tag{5.14}$$

This corresponds to the model in Refs. [10, 20]. The fourth term in the right of Eq. (5.14) is improved by that in Eq. (5.11). The difference is that this term in Eq. (5.11) corresponds to the variation of $[V](r,t)$ due to adsorption and replication, whereas in Eq. (5.14) it also includes its variation due to diffusion [i.e., Eq. (5.14) uses $\frac{\partial[V](r,t)}{\partial t}$ instead of $\left.\frac{\partial[V](r,t)}{\partial t}\right|_g = F(r,t)$]. For details, see the derivation of Eq. (5.8) in Appendix B in the present paper.

Our model will be based on the set of Eqs. (5.11)−(5.13). Their front speed will be derived below, and they will be integrated numerically in Sec. 5.4.

Equations (5.11)−(5.13) can be written in terms of dimensionless variables $\overline{C} \equiv [C]/C_0$, $\overline{V} \equiv [V]/C_0$, $\overline{I} \equiv [I]/C_0$, $\overline{t} \equiv k_2 t$, and $\overline{r} \equiv r\sqrt{k_2/D}$ and dimensionless parameters $\overline{\tau} \equiv k_2\tau$, $\kappa \equiv k_1 C_0/k_2$, and $\overline{I_{MAX}} = I_{MAX}/C_0$, where C_0 is the initial cell concentration. Then Eqs. (5.11)−(5.13) become

$$\frac{\overline{\tau}}{2}\overline{V}_{\overline{t}\overline{t}} + \overline{V}_{\overline{t}} = \overline{V}_{\overline{r}\overline{r}} + \overline{F} - \frac{\overline{\tau}}{2}\kappa\overline{V}\,\overline{C}_{\overline{t}} - \frac{\overline{\tau}}{2}\kappa\overline{F}\,\overline{C} + \frac{\overline{\tau}}{2}Y\left[\overline{I}\left(1 - \frac{\overline{I}}{\overline{I_{MAX}}}\right)\right]_{\overline{t}} \tag{5.15}$$

$$\overline{C}_{\overline{t}} = -\kappa\overline{V}\,\overline{C} \tag{5.16}$$

$$\overline{I}_{\overline{t}} = \kappa\overline{V}\,\overline{C} - \overline{I}\left(1 - \frac{\overline{I}}{\overline{I_{MAX}}}\right), \tag{5.17}$$

where $\overline{F}$ is the dimensionless growth function defined as

$$\overline{F} = -\kappa \overline{V}\,\overline{C} + Y\overline{I}\left(1 - \frac{\overline{I}}{\overline{I}_{MAX}}\right). \tag{5.18}$$

For simplicity, in Eqs. (5.15)−(5.18) we have used de notation $\overline{V}_{\overline{t}}$, $\overline{C}_{\overline{t}}$, and $\overline{I}_{\overline{t}}$ to indicate, respectively, the partial time derivatives of $\overline{V}$, $\overline{C}$, and $\overline{I}$. Moreover, we have omitted the dependences of the dimensionless population densities and growth function [i.e., $\overline{V}(\overline{r},\overline{t})$, $\overline{C}(\overline{r},\overline{t})$, $\overline{I}(\overline{r},\overline{t})$, and $\overline{F}(\overline{r},\overline{t})$ appear as $\overline{V}$, $\overline{C}$, $\overline{I}$ and $\overline{F}$]. In Eq. (5.15) $\overline{V}_{\overline{t}\overline{t}}$ and $\overline{V}_{\overline{r}\overline{r}}$ stand for the second partial time and second partial space derivatives of $\overline{V}$, respectively.

We look for solutions depending only on the new variable $\overline{z} \equiv \overline{r} - \overline{c}\overline{t}$, where $\overline{c} > 0$ is the dimensionless wave front speed, which is related to dimensional speed c by $\overline{c} = c/\sqrt{k_2 D}$. As usual, we linearize our Eqs. (5.15)−(5.18) around the unstable steady state $([V],[C],[I]) = (0, C_0, 0)$, i.e., $(\overline{V},\overline{C},\overline{I}) = (\epsilon_V, 1-\epsilon_C, \epsilon_I)$, where $\overrightarrow{\epsilon} = (\ \epsilon_V, \epsilon_C, \epsilon_I) = \overrightarrow{\epsilon}_0 \exp(-\lambda\overline{z})$. For nontrivial solutions $(\epsilon_V, \epsilon_C, \epsilon_I) \neq (0,0,0)$ to exist, the determinant of the matrix corresponding to the linearized set of three evolution equations must vanish. Therefore, the following characteristic equation must be satisfied:

$$\lambda^3 + \frac{-\overline{c}^2(1+\beta)+1}{\overline{c}(1-\beta\overline{c}^2)}\lambda^2 + \frac{\kappa(\beta\kappa-1)+\beta\kappa Y - 1}{1-\beta\overline{c}^2}\lambda + \frac{(1-\beta\kappa)(\kappa Y - \kappa)}{\overline{c}(1-\beta\overline{c}^2)} = 0. \tag{5.19}$$

For simplicity, we have introduced the parameter $\beta = \overline{\tau}/2$. According to marginal stability analysis [98], the wave front speed can be calculated numerically from

$$\overline{c} = \min_{\lambda>0}[\overline{c}(\lambda)], \tag{5.20}$$

where $\overline{c}(\lambda)$ is given implicitly by Eq. (5.19).

5.3 Approximate explicit equations for the speed

In this section we derive explicit expressions for the dimensionless front speed $\overline{c}$. Its exact value is given by the implicit Eq. (5.20). Since an exact explicit equation for the speed would be very complicated, some assumptions and approximations will be made.

In order to avoid nonpositive values for concentrations, we must impose that the three solutions for λ in Eq. (5.19) are real, so it must be satisfied that

$$-4C_1^3C_3 + C_1^2C_2^2 + 18C_1C_2C_3 - 4C_2^3 - 27C_3^2 \geq 0, \tag{5.21}$$

where C_1, C_2, and C_3 are the coefficients of second, first, and zeroth powers of λ, respectively. We rewrite condition (5.21) in terms of $\nu = \overline{c}^2$ and then we get

$$a_3\nu^3 + a_2\nu^2 + a_1\nu + a_0 \geq 0, \tag{5.22}$$

where the coefficients a_i are easily derived from condition (5.21). However, the exact expressions for a_i are rather long. Fortunately, they can be simplified under some simple

approximations that take into account typical values of the parameters in the present paper, namely, a high value of the yield (e.g., $Y = 2.77 \times 10^5$) and a small value of κ (e.g., $\kappa = 2.15 \times 10^{-3}$). In Sec. 5.5 we will give a detailed discussion of these and other parameter values. Then the coefficients a_i can be written as

$$a_3 \simeq 4\kappa^3 Y^3 \beta^4 - 12\kappa^2 Y^2 \beta^3 + (\chi^2 \kappa^2 Y^2 - 18\chi\omega\kappa^2 Y^2 - 27\omega^2 \kappa^2 Y^2)\beta^2 + (-2\chi^2 \kappa Y + 18\chi\omega\kappa Y)\beta - 4\chi^3 \omega\kappa Y, \tag{5.23}$$

$$a_2 \simeq -4\kappa^3 Y^3 \beta^3 + (-2\chi\kappa^2 Y^2 + 18\omega\kappa^2 Y^2 + 12\kappa^2 Y^2)\beta^2 + (18\chi\omega\kappa^2 Y^2 + 54\omega^2 \kappa^2 Y^2)\beta + 12\chi^2 \omega\kappa Y - 18\chi\omega\kappa Y, \tag{5.24}$$

$$a_1 \simeq \kappa^2 Y^2 \beta^2 - 18\omega\kappa^2 Y^2 \beta - 27\omega^2 \kappa^2 Y^2, \tag{5.25}$$

$$a_0 \simeq 4\omega\kappa Y, \tag{5.26}$$

where $\chi = 1 + \beta$, $\omega = \kappa\beta - 1$, we have assumed the typical values mentioned above and made the approximation $(Y - 1) \simeq Y$. Even at this point, an exact solution for the front speed would be extremely cumbersome. Therefore, below we present two special cases where a manageable expression for the front speed can be found. First, we deal with the case $\beta >> 1$. Then, Eqs. (5.23)-(5.26) can be simplified as

$$a_3 \simeq 4\kappa^3 Y^3 \beta^4, \tag{5.27}$$

$$a_2 \simeq -4\kappa^3 Y^3 \beta^3, \tag{5.28}$$

$$a_1 \simeq \kappa^2 Y^2 \beta^2, \tag{5.29}$$

$$a_0 \simeq 4\omega\kappa Y, \tag{5.30}$$

where we have just kept the highest-order power of β for every coefficient a_i. The critical condition to obtain the propagation speed is given by Eq. (5.22) when the equality holds. Then, substituting Eqs. (5.27)−(5.30) into Eq. (5.22), it is easy to see that the only real, positive solution if $\beta >> 1$ is simply

$$\overline{c} \simeq \frac{1}{\sqrt{\beta}}. \tag{5.31}$$

Note the interesting fact that the velocity is seen to be independent of κ (hence, independent of k_1) and Y in this limit. In Sec. 5.5 we will check this point by means of numerical simulations and discuss it in more detail.

On the other hand, we can easily obtain a solution for the nondelayed case ($\tau = 0$). Then $\beta = 0$ and all of the terms containing β in Eqs. (5.23)−(5.26) vanish. We substitute the resulting coefficients a_i in Eq. (5.22) and obtain

$$\overline{c}_{\beta=0} = \left(\begin{array}{c} -\frac{\delta_2}{3\delta_3} - \frac{2^{1/3}\left(-\delta_2^2+3\delta_3\delta_1\kappa Y\right)}{3\delta_3\left\{-2\delta_2^3-\delta_3^3\delta_1+9\delta_3\delta_2\delta_1\kappa Y+\left[\delta_3\left(-\delta_2^2+3\delta_3\delta_1\kappa Y\right)^3+\left(-2\delta_2^3-\delta_3^3\delta_1+9\delta_3\delta_2\delta_1\kappa Y\right)^2\right]^{1/2}\right\}^{1/3}} \\ + \frac{\left\{-2\delta_2^3-\delta_3^3\delta_1+9\delta_3\delta_2\delta_1\kappa Y+\left[\delta_3\left(-\delta_2^2+3\delta_3\delta_1\kappa Y\right)^3+\left(-2\delta_2^3-\delta_3^3\delta_1+9\delta_3\delta_2\delta_1\kappa Y\right)^2\right]^{1/2}\right\}^{1/3}}{3\cdot 2^{1/3}\delta_3} \end{array} \right)^{1/2}, \tag{5.32}$$

where $\delta_3 = 4$, $\delta_2 = 6$, and $\delta_1 = -27$.

5.4 Numerical simulations

We have integrated numerically the set of Eqs. (5.15)−(5.17), in order to check the exact speeds obtained from Eqs. (5.19) and (5.20) and the approximate speeds from Eqs. (5.31) and (5.32). Numerical simulations are also interesting because they make it possible to obtain not only the front speed, but also profiles for the concentrations of the three species, namely, $[V], [C]$, and $[I]$.

In the experiments that we want to explain, the virus concentration of the initial inoculum is [23],

$$[V]_0 = \begin{cases} v_0, & r < 0.075cm, \\ (1 - \frac{20}{cm}(r - 0.075cm))v_0, & 0.075cm \leq r \leq 0.125cm, \\ 0, & r > 0.125cm, \end{cases} \tag{5.33}$$

where $[V]_0$ is the concentration of viruses at $t = 0$ and $v_0 = 9.3 \times 10^8$/ml.

The initial condition (5.33), together with $[C] = C_0$ everywhere at $t = 0$ and $[I] = 0$ everywhere at $t = 0$, was used in all simulations.

We used finite differences to approximate the partial derivatives in Eqs. (5.15)−(5.17). Typical values for the space and time steps used in our simulations [e.g., in Fig. 5.1 and most of the simulations in Fig. 5.2(b)] were 1.5 s and 1×10^{-5}cm, respectively [dimensionless values for these steps were computed in order to use Eqs.(5.15)−(5.17)]. However, in some cases a higher resolution was required in order to find good agreement with the theoretical front speeds. When high values of the parameters (Y, k, or τ) were explored, the steps of space and time had to be reduced to 1×10^{-6}cm and below 0.3 s, respectively. Moreover, the same high resolution was required when very low values of the same parameters were used. Such step reductions lead to a substantial increase in computing time. Such higher resolution was needed in some of the simulations in Figs. 5.2(a) and 5.3.

Figure 5.1 depicts an example of the concentration profiles $[V], [C]$, and $[I]$ after 48 h of infection. In Fig. 5.1 we observe that the profile of the uninfected cells C has the

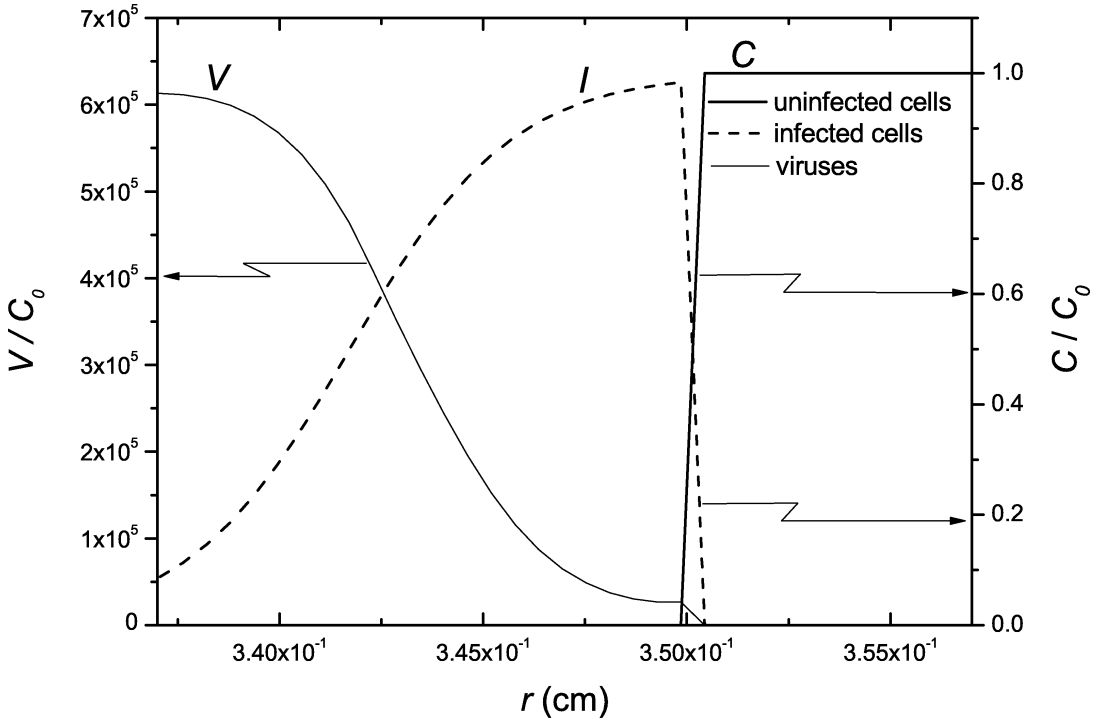

Figure 5.1: Radial profiles of the concentrations $[V], [C]$ and $[I]$ after 48 h of infection, obtained from numerical simulations. The parameter values used are $C_0 = 3.8 \times 10^7$/ml, $Y = 2.77 \times 10^5$, $k_1 = 1.4 \times 10^{-10}$cm^3/h, $k_2 = 2.47$/h, $\tau = 8.1$ h and $D = 8.37 \times 10^{-5}$ cm^2/h (see Sec. V for a discussion on these values).

shape of a front (full curve), whereas that of the infected cells I has the shape of a pulse. This was to be expected intuitively, because the infection [first reaction in Eq. (5.1)] decreases the number of uninfected cells C, which transform into infected cells I and eventually die. On the other hand, their death releases new viruses V [second reaction in Eq. (5.1)] after some delay time τ, which explains the fact that the virus profile lags substantially behind that of infected cells I (in contrast to what is observed in numerical simulations of nondelayed models [99][§]). Finally, let us compute the distance traveled by the infection front during 48 h. This should be 48 h times 0.053 cm/h [from Fig. 5.2(a), rhombus with $\tau \simeq 8$ h], i.e., 0.25 cm. Adding 0.10 cm from the initial condition (5.33) we obtain 0.35 cm for the front position, in agreement with Fig. 5.1.

5.5 Comparison to experiment

In this section we apply our model to the specific case of a VSV focal infection spreading in Baby Hamster Kidney (BHK) cells. Experimental results of this biophysical system, including the observed front speeds, have been published in Ref. [58]. Below we compare

[§]See specially Fig. 2 in Ref. [99]

the observed speed range to both simulations and analytical solutions of our model.

First, we briefly discuss the parameter values used in our computations. Since we have not found any value for I_{MAX} in the VSV experiments [58], we assume that $I_{MAX} \simeq C_0$ (in agreement with Fig. 5.1), i.e., that viruses are able to infect almost all of the cells at large enough times after the infection. The value of I_{MAX} is thus $I_{MAX} \simeq C_0 = 3.8 \times 10^7$/ml [23].

The rate constant for the death of infected cells, k_2, and the virus yield, Y, can be easily derived from the one-step growth data of VSV on BHK cells [Fig. 3(a) in [23]] by fitting the logistic function]Eq. (5.44) in Appendix A]. This is the same procedure we already used in Fig. 5.1 in Ref. [10] (that figure gives details on the same computation for the case of T7 viruses infecting *E. Coli* bacteria). This yields $k_2 = 2.47$/h and $Y = 2.77 \times 10^5$ for VSV infecting BHK cells. The analytical results and numerical simulations for the front speed are shown in Fig. 5.2(a) using these values. For comparison, in Fig. 5.2(b) we have used the yield $Y = 4389$ proposed in Ref. [23]. All parameters except Y have the same values in Figs. 5.2(a) and 5.2(b). Let us now discuss the values of the remaining parameters.

Since the diffusion coefficient D of VSV in agar solutions has not been measured, we performed our analytical and numerical computations using two different values of D, namely that in agar for other viruses [10, 100] [$D = 1.44 \times 10^{-4}$ cm^2/h, full curves in Figs. 5.2(a) and 5.2(b)] and the only value of D for VSV available, which refers to a very specific water solution [55] [$D = 8.37 \times 10^{-5}$ cm^2/h, dashed curves in Figs. 5.2(a) and 5.2(b)].

After VSV viruses infect BHK cells, their progeny leave the cells between $\tau \simeq 2$ h and $\tau \simeq 10$ h after infection [see Fig. 3(a) in [23]]. Within this range, the predicted speeds in our Fig. 5.2(a) are consistent (for $3 < \tau < 7$ h) with the observed range, namely, $(6.6-8.0) \times 10^{-3}$ cm/h [¶], in spite of the fact that the value of the diffusivity for the VSV virus is rather uncertain because (as mentioned above) it has not been measured through agar[‖]. Essentially the same agreement between theory and experiment is also obtained for the value of Y proposed in Ref. [23] [Fig. 5.2(b)]. In contrast, the nondelayed model [$\tau = 0$, as assumed in the model in Ref. [23] corresponding to Eq. (5.2) in the present paper] yields a very large error, as it is clear from its mismatch with the experimental data [compare the dotted horizontal lines to the shaded rectangle in Figs. 5.2(a) and 5.2(b)]. This comparison with the experiments clearly shows the need to take into account the delay-time effect in order to explain the infection speed. This conclusion had not been reached before for VSV infections.

Our approximate solutions for the speed [Eqs. (5.31) and (5.32)] make it possible to understand better the differences between Figs. 5.2(a) and 5.2(b). If the delay time τ

[¶] The mean of this range was obtained from the slope of a linear fit to Fig. 2B in Ref. [58] (data points labeled N1), and the error of the slope was estimated at the 95% confidence-level interval by multiplying the standard deviation of the slope by the t-distribution $t(\frac{0.005}{2}, \nu) \simeq 3.2$, with $\nu = 5-2 = 3$ because there are five data points in that figure (see Ref. [101], specially p. 25 therein).

[‖] The value of the diffusivity is rather uncertain also because the value of $f \equiv C_0/C_{\max}$ necessary to estimate the effective diffusion coefficient (D_{eff} in Ref. [9]) was not measured in Refs. [23, 58], so we have had to approximate $D_{eff} \simeq D$.

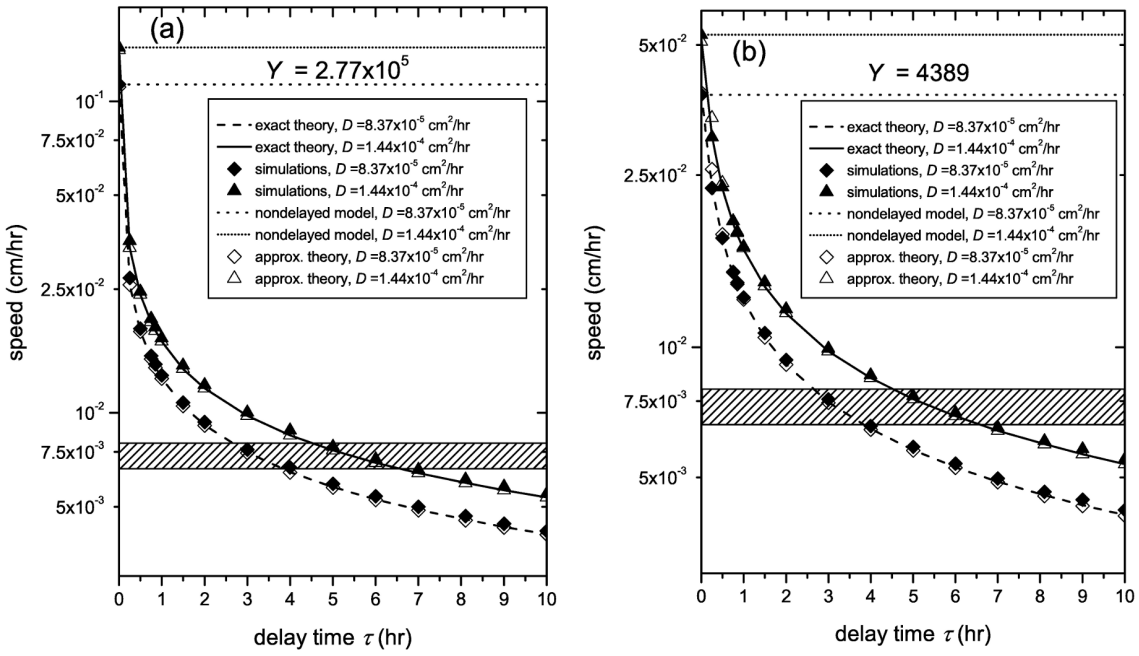

Figure 5.2: Predicted front speed versus the delay time τ, for (a) the value $Y = 2.77\times10^5$ proposed in this paper and (b) the value $Y = 4389$ proposed in Ref. [23]. The dotted horizontal lines correspond to the nondelayed model ($\tau = 0$) and the hatched rectangle to the experimental range, namely $(6.6-8.0)\times10^{-3}$ cm/h . The curves are the analytical results from Eqs. (5.19) and (5.20) and the full symbols are the numerical simulations. The empty symbols indicate the approximate analytical speed results. The parameter values used are $C_0 = 3.8 \times 10^7$/ml, $k_1 = 1.4 \times 10^{-10}$cm^3/h and $k_2 = 2.47$/h.

is large enough, according to Eq. (5.31) the front speed does not depend on Y neither κ. Both simulations and exact analytical results agree with the non-dependence of the speed on Y, since for $\tau > 2$ h the curves in Figs. 5.2(a) and 5.2(b) are approximately the same. Note also that the approximate Eq. (5.31) has been derived assuming a high value of Y. Because of this, for $\tau < 2$ h some differences between the exact and the approximate results arise [specially in Fig. 5.2(b), because the value of Y is two orders of magnitude smaller than in Fig. 5.2(a)]. Similarly, the approximate speed for $\tau = 0$ [Eq. (5.32)] is much more accurate for high values of Y [Fig. 5.2(a)].

In Figs. 5.1 and 5.2 we have used the value $k_1 = 1.4 \times 10^{-10}$cm^3/h proposed in Ref. [23] for the adsorption rate, because the value of k_1 has not been measured experimentally for VSV infecting BHK cells. However, the former value $k_1 = 1.4\times10^{-10}$cm^3/h was obtained by fitting the observations to an extracellular model in Ref. [23]. Because that model does not take into account the role of the delay time τ [compare Eqs. (5.2) to (5.11) above], this value of k_1 should be regarded as highly uncertain. Therefore, we analyzed the dependence of the front speed on k_1. We found the very interesting result, shown in Fig. 5.3, that the value of the front speed is approximately independent of k_1

over several orders of magnitude (provided that the delay time τ is taken into account, as first done in the present paper for VSV infections). Indeed, in Fig. 5.3, the speed remains almost independent of the adsorption rate k_1 for large enough values of the delay time τ, namely $\tau > 2$ h. In contrast, k_1 becomes a relevant parameter for the case $\tau = 0$. This is reasonable intuitively, because a long enough delay τ in the release of the new generation of viruses from the infected cells will substantially slow down the infection process. Then we should expect the time needed for the parent virus to cross the cell membrane (which is measured by k_1) to become irrelevant. This is indeed observed in Fig. 5.3 for $\tau > 2$ h. The approximate solution given by Eqs. (5.31) and (5.32) also supports this conclusion, because for large enough values of τ ($\beta >> 1$) according to Eq. (5.31) the speed does not depend on κ, hence neither in k_1 [whereas for the nondelayed case ($\tau = 0$), Eq. (5.32) shows a nonlinear dependence on κ and therefore on k_1]. This also illustrates that the conclusions obtained from delayed and nondelayed models can be very different. Furthermore, this makes it possible to make quantitative predictions of the front speed in spite of the uncertainty in the value of k_1, and strongly supports the validity of our Figs. 5.2(a) and 5.2(b), because it shows that they would remain almost the same even if the value of k_1 differed several orders of magnitude from the value used to obtain those figures (namely, $k_1 = 1.4 \times 10^{-10}\text{cm}^3/\text{h}$, from Ref. [23]).

We can also see that there is good agreement between the analytical results from Eqs. (5.19) and (5.20) (curves in Figs. 5.2 and 5.3) and the numerical simulations of Eqs. (5.15)−(5.18) (full symbols).

Relative differences between the speeds in Fig. 5.3 would not change if a different value of the virus diffusivity D were used. This is due to the fact that in the dimensionless Eq. (5.19), the parameter D does not appear, thus it is used only when computing the dimensional speed c from the dimensionless one $\overline{c}$ as $c = \overline{c}\sqrt{k_2 D}$. Thus, using another diffusivity value $\widetilde{D}$ would only change the speeds by the factor $\sqrt{\widetilde{D}/D}$. Hence, we have shown that the only two parameters that have not been measured experimentally (namely, D and k_1) do not affect our conclusion that the role of the delay time cannot be neglected in order to understand VSV infection speeds.

In this section we have shown that the delay time τ is a strongly significant parameter in models of VSV infection spread. The authors of Ref. [23] fitted a large number of parameters (up to 9). In some cases, this can lead to overfitting the observed phenomena. We also think that it can sometimes lead to unjustified conclusions (e.g., to neglect the role of the delay time, which here we have found to be of utmost importance). In this paper, we have only used two unknown parameters (D and k_1) and shown that they are not strongly relevant to our main conclusions.

5.6 Concluding remarks

We have built a simple time-delayed model of VSV infections. In order to do so, we have improved a model previously applied to other kinds of viruses [10]. Our analytical speeds agree well with those from numerical simulations. They are also in agreement

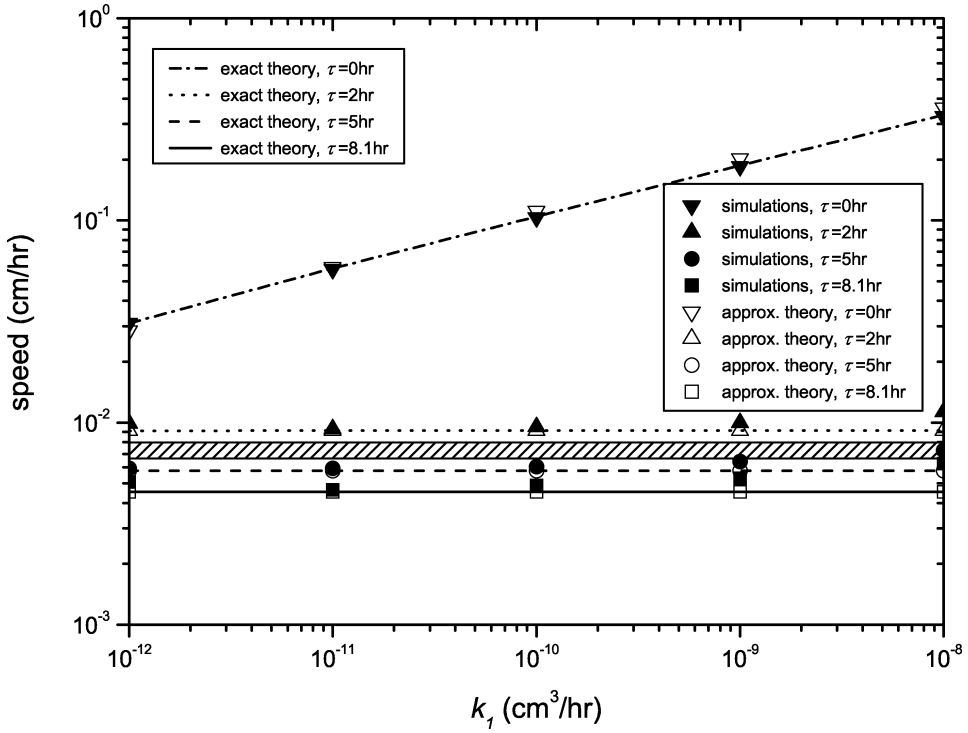

Figure 5.3: Front speed versus adsorption rate k_1 for several values of the delay time. The hatched rectangle corresponds to the experimental range, namely, $(6.6-8.0)\times 10^{-3}$ cm/h . The curves correspond to the analytical results from Eqs. (5.19) and (5.20) and the full symbols to the numerical simulations. The empty symbols indicate the approximate analytical speed results. The parameter values used are $C_0 = 3.8\times 10^7$/ml, $D = 8.37\times 10^{-5}$cm^2/h, $k_2 = 2.47$/h and $Y = 2.77\times 10^5$.

with experimentally observed VSV infection speeds [Figs. 5.2(a) and 5.2(b)]. Moreover, we have derived approximate front speeds that have lead us to additional understanding on the results and made our conclusions more intuitive.

As expected intuitively, the front speed decreases with increasing values of the delay time τ [Figs. 5.2(a) and 5.2(b)]. We have obtained a strong decrease from $\tau = 0$ to $\tau \simeq 1$ h, and a smoother decrease for larger values of τ. We have shown that the introduction of the delay time τ is critically important to account for the front speeds of VSV infections. Indeed, neglecting the delay-time effect (i.e., $\tau = 0$) leads to an infection front speed one order of magnitude faster than the observed range [Figs. 5.2(a), 5.2(b), and 5.3].

Moreover, we have shown that the infection speed is almost independent of the adsorption rate k_1 over four orders of magnitude for large enough values of the delay time τ (Fig. 5.3), a conclusion not previously reached for any kind of virus infections.

5.7 Appendix A. Logistic growth in an homogeneous medium

As mentioned in Sec. 5.2, Eqs. (5.2)−(5.4) do not agree with the experimental data in the so-called one-step growth experiments. To see this, consider the very simple case of a homogeneous medium [so that $\partial^2[V](r,t)/\partial r^2 = 0$], composed initially only of *infected* cells [$[C](t) \simeq 0$ and $[I](t=0) = [I]_0$] and free viruses [$[V](t=0) = [V]_0$]. In such a situation, Eq. (5.4) becomes simply

$$\frac{d[I](t)}{dt} = -k_2[I](t), \tag{5.34}$$

so that

$$[I](t) = [I]_0 \exp(-k_2 t), \tag{5.35}$$

and Eq. (5.2) simplifies to

$$\frac{d[V](t)}{dt} = k_2 Y[I](t) = Y k_2 [I]_0 \exp(-k_2 t), \tag{5.36}$$

thus

$$[V](t) = [V]_0 + Y[I]_0 \left(1 - \exp[-k_2 t]\right). \tag{5.37}$$

However, this exponential behavior does not agree with the experimental data in the so-called one-step growth experiments, because in those experiments a logistic or S-shape curve is always observed instead (see, e.g., Fig. 1 in Ref. [10]).

As a solution to avoid this inconsistency, it has been proposed [10] to replace Eqs. (5.2)−(5.4) by Eqs. (5.5)−(5.7). In order to explain this point, let us derive the virus dynamics predicted by the set [Eqs. (5.5)−(5.7)] in one-step growth experiments. Taking into account again that those experiments are performed in an homogeneous medium [so that the first term in the right-hand side of Eq. (5.5) is negligible] and in the absence of uninfected cells [so that $[C](r,t) \simeq 0$], Eqs. (5.5)−(5.7) simplify to

$$\frac{d[V](t)}{dt} = -Y\frac{d[I](t)}{dt}, \tag{5.38}$$

$$\frac{d[I](t)}{dt} = -k_2[I](t)\left(1 - \frac{[I](t)}{I_{MAX}}\right). \tag{5.39}$$

Integration of Eq. (5.39) yields

$$[I](t) = \frac{I_{MAX}}{1 + \left(\dfrac{I_{MAX}}{[I]_0} - 1\right)\exp[k_2 t]}, \tag{5.40}$$

where $[I]_0$ is the value of $[I](t)$ at time $t = 0$. Note that this equation leads to $[I](t) \to 0$ for $t \to \infty$, as it should (because after a sufficiently long time, all infected cells will have died due to the second of reactions [Eq. (5.1)]).

On the other hand, integrating Eq. (5.38) from $t = 0$ *to* $t \to \infty$ we come to

$$[V]_\infty = [V]_0 + Y[I]_0, \tag{5.41}$$

so the increase in the concentration of viruses is limited by the initial concentration of infected cells $[I]_0$ and the yield Y, as it should (because Y viruses per infected cell are produced, according to the second of reactions [Eq. (5.1)]).

If we integrate Eq. (5.38) from $t = 0$ to t we obtain, instead of Eq. (5.41),

$$[V](t) = [V]_0 + Y\left[[I]_0 - [I](t)\right], \tag{5.42}$$

so, again, the increase in virus particles is equal to the decrease in infected cells multiplied by the yield. This is much more reasonable intuitively than Eq. (5.37).

Using Eq. (5.40) into (5.42) leads us to

$$[V](t) = [V]_0 + Y[I]_0 - \frac{Y\ I_{MAX}}{1 + \left(\dfrac{I_{MAX}}{[I]_0} - 1\right)\exp[k_2 t]}. \tag{5.43}$$

If only a few viruses are present initially ($[V]_0 \ll Y[I]_0$ or $[V]_0 \ll [V]_\infty$) and the initial concentration of infected cells is close to saturation ($[I]_0 \simeq I_{MAX}$), this simplifies to

$$[V](t) = \frac{Y\ I_{MAX}}{c_1 \exp[-k_2 t] + 1}, \tag{5.44}$$

where $c_1 \equiv \left(\frac{I_{MAX}}{[I]_0} - 1\right)^{-1}$. Equation (5.44) is the typical logistic or S-shaped curve which (in contrast to the exponential curve [Eq. (5.37)] agrees very well with experimental data of one-growth experiments [see Eq. (3) and Fig. 1 in Ref. [10], and Fig. 2 in Ref. [58]]. We conclude that, both intuitively [see the text below Eq. (5.42)] and from the perspective of providing good fits to experimental data, Eqs. (5.5)−(5.7) are more reasonable than Eqs. (5.2)−(5.4).

Notwithstanding the former two strong arguments, the question arises if there is some physical mechanism that can lead to a dynamics with a quadratic saturation term [last term in Eq. (5.39)] or, equivalently, to its analytical solution [the logistic expression (5.44)]. The answer is that there is at least one such mechanism, namely, to consider that in practice not all viruses spend exactly the same time inside a cell before releasing their progeny (i.e., that the value of the delay time τ is not the same for all virus particles). Then, if we choose the time origin $t = 0$ when the viruses enter the cells, the number of viruses at time t will be

$$[V](t) = [V]_0 + (Y - 1)[V]_0 \int_0^t d\tau\ \varphi(\tau), \tag{5.45}$$

where $\varphi(\tau)$ is the probability distribution of the delay time τ. Note that in the special case that all viruses have exactly the same value of τ, say τ_0, $\varphi(\tau)$ is a Dirac delta

centered at $\tau = \tau_0$ and Eq. (5.45) yields $[V](t) = [V]_0$ if $t < \tau_0$ and $[V](t) = Y[V]_0$ if $t > \tau_0$, as it should. If we consider the following delay-time distribution,

$$\varphi(\tau) = \frac{Y\ I_{\max}}{(Y-1)[V]_0} \frac{c_1\ k_2 \exp[-k_2\tau]}{\left(c_1 \exp[-k_2\tau] + 1\right)^2}, \tag{5.46}$$

which is bell-shaped (see the full curve in the inset to Fig. 1 in Ref. [21]), using it into Eq. (5.45) and integrating yields the logistic Eq. (5.44), i.e., the solution to the quadratic expression (5.39). This gives a possible physical reason for the logistic solution [Eq. (5.44)], and thus for the quadratic evolution Eq. (5.39). However, we stress that there are other reasons why such a quadratic evolution equation is more reasonable than a linear one, both intuitively [see the text below Eq. (5.42)] and from the perspective of providing better fits to experimental data [see the text below Eq. (5.44)]. In any case, the inclusion or not of a quadratic saturation term does not affect the analytical results in this paper, since the infection speeds derived would be the same if the quadratic term [last term in Eqs. (5.5), (5.7), and (5.39)] were neglected [because after linearization, the last term in Eqs. (5.15), (5.17), and (5.18) do not yield any term in Eq. (5.19)]. However, let us emphasize an important practical advantage of including this quadratic term, namely, that since Eq. (5.44) instead (5.37) gives a much better fit to data, it leads to a more accurate estimate of the value of k_2 (as we have done in the Comparison to experiment section).

Finally, it is worth to note that Y appears multiplying k_2 in all reaction-diffusion equations for $[V]$ discussed in this paper [i.e., Eqs. (5.2), (5.5), (5.9) and (5.11)]. Therefore, the question arises if it is possible to absorb Y into k_2 and, in this way, get rid of one parameter. The problem is that one-step growth experiments measure $[V](t)$ but not $[I](t)$ (see, e.g., p. 1736 in Ref. [23]). Thus in order to estimate the parameter values, it is necessary to fit Eq. (5.44) to the experimental data. But in Eq. (5.44) Y no longer multiplies k_2. For this reason, Y cannot be absorbed into k_2.

5.8 Appendix B. Time-delayed reaction-diffusion equation

In order to make this paper as much self-contained as possible, in this appendix we give a derivation of the time-delayed reaction-diffusion Eq. (5.8). Variations in the population number density of viruses are due to two processes: population growth (replication minus adsorption) and dispersal. As usual [43], we Taylor-expand the variation due to population growth,

$$\begin{aligned} \left|[V](x,y,t+\tau) - [V](x,y,t)\right|_g &= \tau \left.\frac{\partial [V](x,y,t)}{\partial t}\right|_g + \frac{\tau^2}{2} \left.\frac{\partial^2 [V](x,y,t)}{\partial t^2}\right|_g + \cdots \\ &= \tau F(r,t) + \frac{\tau^2}{2} \left.\frac{\partial F(r,t)}{\partial t}\right|_g + \cdots \end{aligned} \tag{5.47}$$

where (x, y) are Cartesian space coordinates, τ is the generation time, the subindex g means growth, and we have introduced the growth function as $F(r,t) \equiv \left.\frac{\partial [V]}{\partial t}\right|_g$. On the other hand, the variation due to dispersal is [9]

$$\begin{aligned} &|[V](x,y,t+\tau) - [V](x,y,t)|_d \\ &\quad = \iint [V](x+\Delta_x, y+\Delta_y, t)\, \phi(\Delta_x, \Delta_y)\, \mathrm{d}\Delta_x \mathrm{d}\Delta_y \\ &\quad - [V](x,y,t)\,, \end{aligned} \tag{5.48}$$

where we have introduced the dispersal kernel $\phi(\Delta_x, \Delta_y)$, defined as the probability per unit area that a virus particle initially placed at $(x+\Delta_x, y+\Delta_y)$ has moved to (x,y) after a generation time τ. In a system involving both dispersal and population growth, the total variation is the sum of both contributions,

$$\begin{aligned} &[V](x,y,t+\tau) - [V](x,y,t) = \\ &\quad \iint [V](x+\Delta_x, y+\Delta_y, t)\, \phi(\Delta_x, \Delta_y)\, \mathrm{d}\Delta_x \mathrm{d}\Delta_y \\ &\quad - [V](x,y,t) + \tau F(r,t) + \frac{\tau^2}{2} \left.\frac{\partial F(r,t)}{\partial t}\right|_g + \cdots \end{aligned} \tag{5.49}$$

Finally, we Taylor-expand Eq. (5.49) up to second order in time and space and assume an isotropic kernel [i.e., $\phi(\Delta_x, \Delta_y) = \phi(\Delta)$, with $\Delta = \sqrt{\Delta_x^2 + \Delta_y^2}$]. This yields **

$$\begin{aligned} \frac{\partial [V]}{\partial t} + \frac{\tau}{2}\frac{\partial^2 [V]}{\partial t^2} &= D\left(\frac{\partial^2 [V]}{\partial x^2} + \frac{\partial^2 [V]}{\partial y^2}\right) + F(r,t) + \frac{\tau}{2} \left.\frac{\partial F(r,t)}{\partial t}\right|_g \\ &\simeq D\frac{\partial^2 [V](r,t)}{\partial r^2} + F(r,t) + \frac{\tau}{2} \left.\frac{\partial F(r,t)}{\partial t}\right|_g, \end{aligned} \tag{5.50}$$

where D is the diffusion coefficient $D = \frac{\langle \Delta^2 \rangle}{4\tau} = \frac{\langle \Delta_x^2 \rangle}{2\tau} = \frac{\langle \Delta_y^2 \rangle}{2\tau}$. Equation (5.50) is the time-delayed Eq. (5.8) in our model. Note that the last term reads $\left.\frac{\partial F(r,t)}{\partial t}\right|_g$ instead of $\frac{\partial F(r,t)}{\partial t}$. This corrects an error in a previous derivation [9] that was later applied to T7 virus infection fronts infecting *E. Coli* bacteria [10, 20]. That error was due to not including the symbol $...|_g$ in the last term in Eq. (5.47).

5.9 Acknowledgements

Funded by the Ministry of Science (Consolider grant No. CSD-2010-00034 and grant No. FIS-2009-13050), the European Commission (grant No. 28192-FEPRE), and the Generalitat de Catalunya (grant No. 2009-SGR-374). D.R.A. was supported by the MEC under the FPU program.

**See footnote *.

Chapter 6

Lag-driven motion in front propagation

This chapter is an exact transcription of the contents of the following manuscript submitted for publication at the Journal of Statistical Mechanics: Theory and Experiment and is being revised at the moment of writing this Ph. D. thesis:

Amor, D. R. & Fort, J. Lag-driven motion in front propagation. *J Stat Mech - Theor Exp* Submitted.

Abstract Front propagation is an ubiquitous phenomenon. It arises in physical, biological and cross-disciplinary systems as diverse as flame propagation, superconductors, virus infections, cancer spread or transitions in human prehistory. Here we derive a single, approximate front speed from three rather different time-delayed reaction-diffusion models, suggesting a general law. According to our approximate speed, fronts are crucially driven by the lag times (periods during which individuals or particles do not move). Rather surprisingly, the approximate speed is able to explain the observed spread rates of completely different biophysical systems such as virus infections, the Neolithic transition in Europe, and postglacial tree recolonizations.

6.1 Introduction

Fronts are widely used in physical models of flame propagation [7], superconductors [8], virus infections [10], cancer spread [11], transitions in human prehistory [9], etc. In many systems, individuals or particles are at rest during some time intervals, and for this reason the corresponding fronts become time-delayed [9]. For single-species systems, the dynamics is governed by the hyperbolic reaction-diffusion (HRD) equation [43]:

$$\frac{\delta p}{\delta t}+\frac{T}{2}\frac{\delta^2 p}{\delta t^2}=D\left(\frac{\delta^2 p}{\delta x^2}+\frac{\delta^2 p}{\delta y^2}\right)+\left.\frac{\delta p}{\delta t}\right|_g+\left.\frac{T}{2}\,\frac{\delta^2 p}{\delta t^2}\right|_g, \tag{6.1}$$

where $p = p(x, y, t)$ is the population (or particle) number density at point (x, y) and time t, D is the diffusion coefficient, and the subindex $...|_g$ indicates that the corresponding time derivatives take into account growth (i.e., net reproductive) but not diffusive processes [43]. In Eq. (6.1), terms proportional to T are second-order Taylor expansion terms [43] and account for the effects of the delay (or lag) time T which is elapsed between two successive motions of particles or individuals. If no delay time is considered (i.e., if $T = 0$), Fisher's classical reaction-diffusion equation [2] is recovered.

A set of coupled equations is required when extending the scope to multiple-species systems. For example, focal infections provide a convenient experimental platform to study the replication (reaction) and spread (diffusion) of viruses in a cell monolayer [10, 56, 58]. The interaction between viruses (V), non-infected cells (C) and infected cells (I) give rise to the following evolution equations [10, 20, 102]:

$$\frac{\partial [C]}{\partial t} = -k_1 [C][V], \tag{6.2}$$

$$\frac{\partial [I]}{\partial t} = k_1 [V][C] - k_2 [I] \left(1 - \frac{[I]}{I_{MAX}} \right), \tag{6.3}$$

where k_1 stands for the rate constant of adsorption of viruses V to non-infected cells C and k_2 is the death (or lysis) rate of infected cells I (each infected cell releases a new generation of Y viruses after a delay time T). If we replace p by the virus number density $[V](r, t)$ (where r is the radial coordinate centered at the inoculation point of the infection) in the above HRD equation (6.1), we obtain the evolution equation for the virus population. In agreement with Eqs. (6.2)-(6.3), the virus population growth reads:

$$\left. \frac{\delta [V]}{\delta t} \right|_g = -k_1 [V][C] + k_2 Y [I] \left(1 - \frac{[I]}{I_{MAX}} \right). \tag{6.4}$$

Hence, in order to determine the dynamics of focal infections, the set of differential equations (6.1)-(6.4) must be solved. Whereas the exact speed of front solutions to the Eqs. (6.1)-(6.4) is very complicated (see Appendix A), recently we derived an approximate solution for the spread of virus infections which reads [102]†:

$$c = \sqrt{2D/T}. \tag{6.5}$$

Note that dimensional analysis could also suggest that c is proportional to $\sqrt{D/T}$, but other dependencies are possible on this ground, e.g. $\sqrt{k_2 D}$ for Eqs. (6.1)-(6.4), $\sqrt{aD}$ (Fisher's speed [2]), $\sqrt{a^2 D/T}$ for Eq. (6.1), etc. Moreover, dimensional analysis cannot predict the factor $\sqrt{2}$, which was derived by marginal stability analysis in Ref. [102].

We would like to emphasize the following physical interpretation of Eq. (6.5). First, the parameter T is defined as the mean time a virus needs to reproduce inside an infected cell. If this lag T is substantially longer than the rest of the interval times involved in a

†In Ref. [102] we presented an approximate infection front speed in dimensionless variables which is equivalent to Eq. (6.5) in the present paper.

virus life cycle (i.e., the death time of cells k_2^{-1}, the mean travel time in the extracellular medium, and the time viruses need to cross the cell membrane $k_1^{-1}C_0^{-1}$), then T becomes the only relevant time scale in our model. On the other hand, the parameter D is related to how easily the virus diffuses in the extracellular medium. It is thus reasonable that the parameters T and D determine the front speed under these assumptions. But is this framework valid in real situations? Before closing this introduction, we address this question by applying Eq. (6.5) to several virus infections.

Figure 6.1 compares the results from the approximate speed (6.5), the exact theory, and simulations for the front speed of focal infections for Vesicular Stomatitis Virus (VSV) [102]. Moreover, for the first time Eq. (6.5) is applied to the T7 virus [10]: in Fig. 6.1 we present results for two T7 strains, namely the wild type and the p005 mutant [56]. Both for T7 and VSV, perfect agreement between the exact result (which is rather complicated, see Appendix A) and the approximate speed (6.5) is observed. Hence Eq. (6.5) provides convenient results to predict virus infection speeds. Moreover, both exact and approximate results in Fig. 6.1 show consistency with the corresponding experimental data (shaded rectangles).

The main aims of the present paper are (i) to derive mathematically the same approximate equation (6.5) for two other systems, which are driven by equations completely different to the virus reaction-diffusion equations (6.1)-(6.4), and (ii) to show that a fair agreement with observations can be attained also for those two additional systems. Accordingly, in Sec. 6.2 we consider a single-population model (and apply it to the Neolithic transition front in Europe) and in Sec. 6.3 we analyze a structured populations model (and apply it to forest recolonization fronts).

6.2 Approximate front speed for nonstructured populations

Two major processes drive the spatial population dynamics of biophysical systems: population growth (reproduction minus deaths) on one hand, and migration (dispersal) on the other. In many cases, these two processes can be considered independent of each other. Typically, such an assumption is implicit in the study of nonstructured populations [9, 43]. Within this framework, in this section we derive an approximate front speed from reaction-diffusion equations applied to nonstructured populations systems involving a single species. For the sake of clarity, we first review briefly the derivation of the HRD speed [9, 43].

The variation of the population number density due to population growth can be generally expressed as a Taylor series,

$$[p(x,y,t+T)-p(x,y,t)]_g = T\left.\frac{\delta p}{\delta t}\right|_g + \frac{T^2}{2}\left.\frac{\delta^2 p}{\delta t^2}\right|_g + ... \tag{6.6}$$

where the subindex $...|_g$ indicates that the corresponding time derivatives take into account growth (i.e., net reproductive) but not migration processes [43]. In most bio-

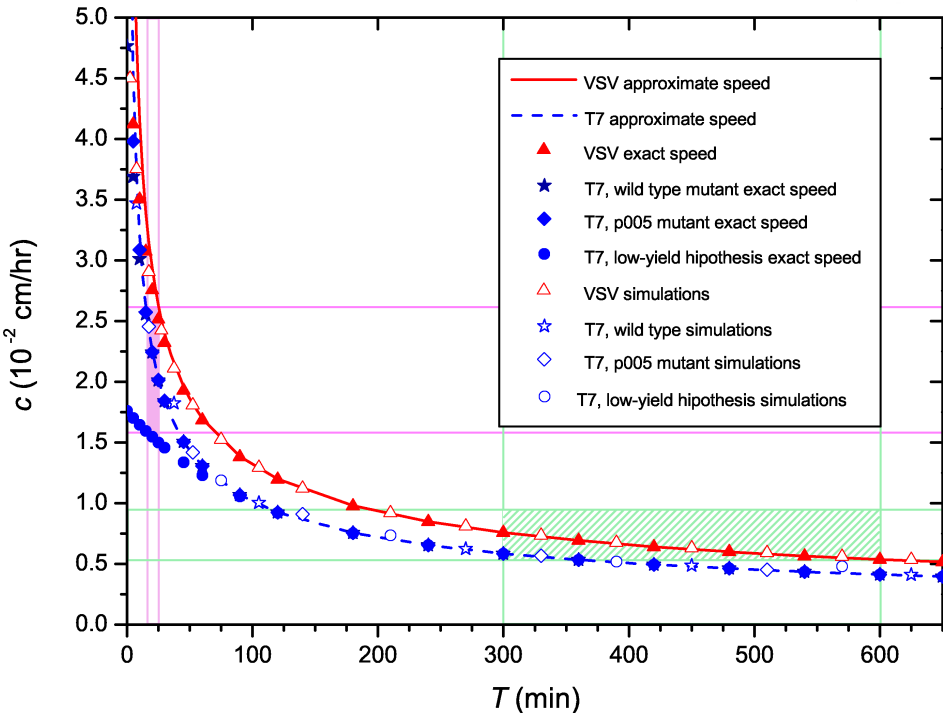

Figure 6.1: **Focal infections**. Front speed versus lag time. Curves stand for the approximate solution $c = \sqrt{2D/T}$. The solid curve corresponds to VSV ($D = 1.44{\cdot}10^{-4}$ cm^2/hr) and the dashed curve to the two T7 mutants ($D = 8.55 \cdot 10^{-5}$ cm^2/hr). Full (empty) symbols correspond to the results of the exact theory (simulations). Triangles represent the results for VSV ($Y = 4983$ [102]). Stars stand for the wild T7 strain ($Y = 34.5$ [10]), and rhombs for the p005 T7 mutant ($Y = 63.6$). Circles represent an hypothetical low-yield case $Y = 5$. The hatched (shaded) shaded area corresponds to the observed ranges of T and c for VSV (T7) viruses. Details on the parameter values and the simulations appear in appendix A.

logical applications the lag T corresponds to one generation [9] (see, e.g., the lag time in focal infections above).

In order to account for migration (dispersal), it is useful to define the dispersal kernel $\phi(\Delta_x, \Delta_y)$ as the probability per unit area that an individual initially placed at $(x + \triangle_x, y + \triangle_y)$ has reached the position (x, y) after a time T. This leads to the following change for the population density due to the migration process [9, 43],

$$[p(x,y,t+T) - p(x,y,t)]_m = \int_{-\infty}^{+\infty}\int_{-\infty}^{+\infty} p(x+\Delta_x, y+\Delta_y, t) \\ \phi(\Delta_x,\Delta_y) d\Delta_x\, d\Delta_y - p(x,y,t). \tag{6.7}$$

Thus, the evolution of a system involving both processes (i.e., population growth and migration) is driven by the sum of both contributions,

$$p(x,y,t+T) = \int_{-\infty}^{+\infty}\int_{-\infty}^{+\infty} p(x+\Delta_x, y+\Delta_y, t) \\ \phi(\Delta_x,\Delta_y)d\Delta_x\, d\Delta_y + T\left.\frac{\delta p}{\delta t}\right|_g + \frac{T^2}{2}\left.\frac{\delta^2 p}{\delta t^2}\right|_g + ... \tag{6.8}$$

If isotropic migration is assumed (i.e., if $\phi(\Delta_x,\Delta_y)=\phi(\Delta)$, with $\Delta=\sqrt{\Delta_x^2+\Delta_y^2}$), then Taylor-expanding the above equation (6.8) up to second order in time and space yields the HRD equation (6.1). The diffusivity of the population in the HRD equation is defined as $D=\frac{<\Delta^2>}{4T}$ [9]. In order to solve the HRD equation, it is convenient to define $F(p)$ as the population growth function $F(p)=\left.\frac{\delta p}{\delta t}\right|_g$. Assuming (i) low population densities at the leading edge of the front, (ii) that the front is locally planar for $t\to\infty$ and $r\to\infty$, and (iii) constant-shape solutions with the form $p=\overline{p}\exp[\lambda(x-ct)]$, then the exact solution of Eq. (6.1) yields the HRD front speed, namely [43]

$$c=\frac{2\sqrt{DF'(0)\left[1+\frac{T}{2}F'(0)\right]}}{1+TF'(0)}, \tag{6.9}$$

where the growth rate at the front's edge has been approximated as $F'(0)=\left.\frac{dF}{dp}\right|_{p=0}$.

Let us now consider the limiting case of a high reproduction rate, $F'(0)\to\infty$, into the above equation (6.9). This leads to the very simple expression

$$c=\sqrt{2D/T}. \tag{6.10}$$

Remarkably, this simple approach has led us to the very same approximate front speed as for the case of focal infections above (see Eq. 6.5). It is worth to note that the single-species systems analyzed in this section are very different (both mathematically and physically) from the focal infections considered in the introduction (in which the equations of the system must account for the interactions between three species, so a set of coupled equations is involved instead of a single equation).

Let us now apply the HRD equation [43] to the invasion front of the Neolithic transition, in order to check the results of the approximate speed $c=\sqrt{2D/T}$. Previous HRD models for this single-species system [9, 43] have shown good agreement with the observed dates from hundreds of European Neolithic sites [32]. Applying the HRD exact speed (6.9) involves the computation of the Neolithic population growth function. For this purpose, we consider the logistic growth function, which agrees very well with many human populations [9, 66], namely

$$F(p)=\left.\frac{\delta p}{\delta t}\right|_g = ap\left(1-\frac{p}{p_{\max}}\right), \tag{6.11}$$

where a is called the initial growth rate and $p_{\max}$ is the saturation density. Note that considering logistic growth leads to $F'(0)=a$.

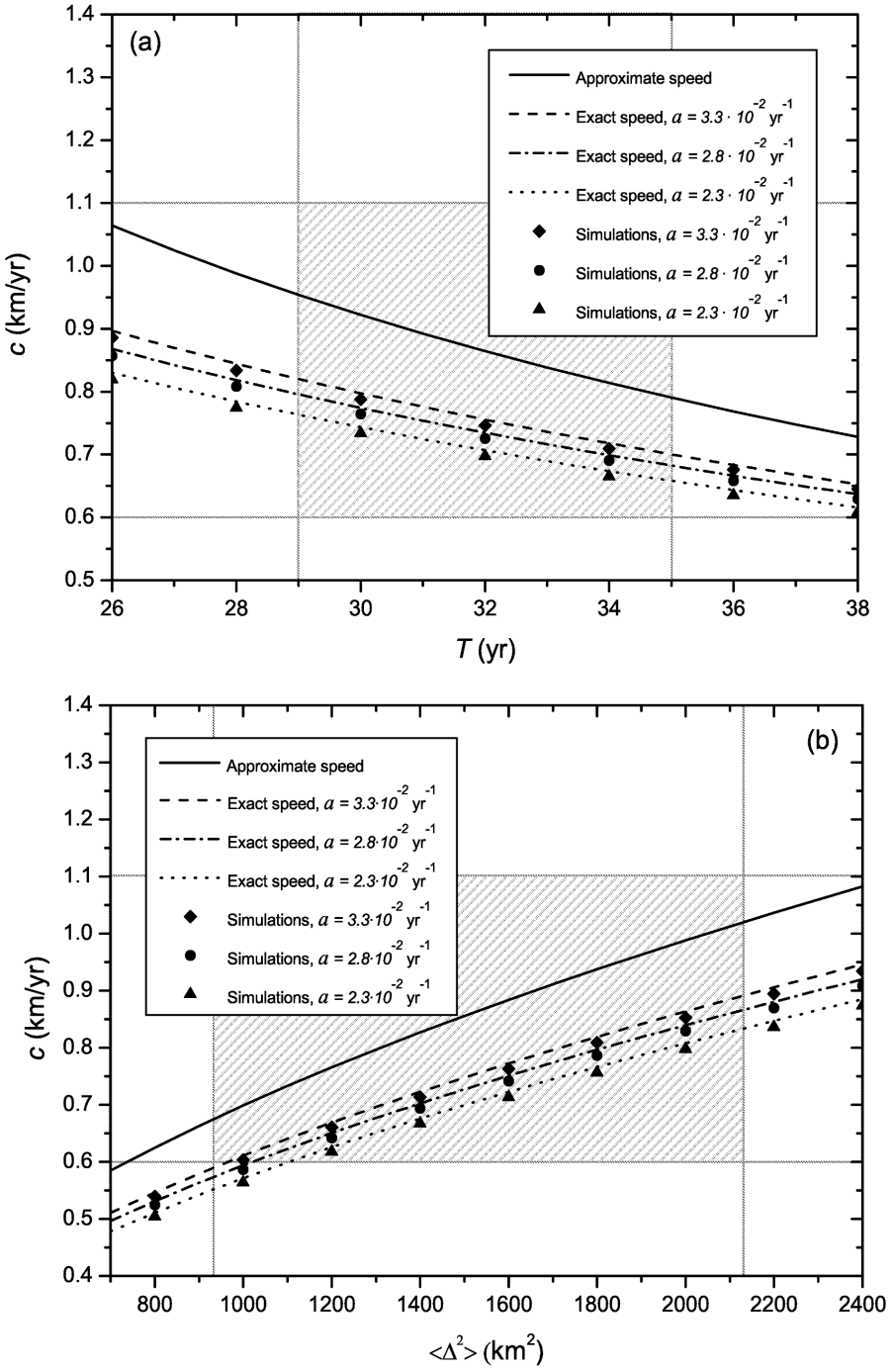

Figure 6.2: **The Neolithic transition.** a) Invasion front speed versus T (using $< \Delta^2 >= 1531$ m^2 [30]). The solid curve corresponds to the approximate $c = \sqrt{2D/T}$. The dashed-dotted curve represents the exact theoretical speed (6.9) for the mean observed value $a = 2.8 \cdot 10^{-2}$ yr^{-1} [30]. The dashed and dotted curves stand for the maximum ($a = 3.3 \cdot 10^{-2}$ yr^{-1}) and minimum ($a = 2.3 \cdot 10^{-2}$ yr^{-1}) values of the observed range, respectively. Symbols correspond to numerical simulations as indicated in the legend (see the appendix B for details on the simulations). The hatched area indicates the observed ranges of T [61] and c [32]. b) Invasion front speed versus the mean-squared migration distance. The curves and the symbols stand for the same cases presented in a), but for $T = 32$ yr. The hatched rectangle represents the observed ranges of $< \Delta^2 >$ and c [30, 32].

Figure 6.2(a) plots the invasion speed of the Neolithic transition as a function of T. In this case, T represents the generational lag during which children stay with their parents until they reach adulthood and can migrate [61]. Figure 6.2(b) plots the Neolithic front speed as a function of the mobility $< \Delta^2 >$ [30]. In both Figs. 6.2(a) and 6.2(b) we observe differences (about 15%) between the approximate speed (6.5) and the exact solution (6.9) if the mean observed growth rate $a = 0.028$ yr^{-1} [30,103–105] is considered. Interestingly, both the approximate and the exact solutions are consistent with the observed invasion speed of the Neolithic front, as estimated from archaeological data [hatched area in Figs. 6.2(a) and 6.2(b) [32,61].

6.3 Approximate front speed for structured populations

In some biophysical systems, the age structure of the population plays a major role on the evolution of the system [19,106,107]. In some cases (e.g., for tree species), the fertile ages of several generations widely overlap. Thus it is necessary to introduce $p_i(x, y, t)$ as the number density of the subpopulation which is i years old ($i = 1, 2, ..., N$). The system dynamics is then controlled by the vector equation [106]

$$\overrightarrow{p}(\Delta x, \Delta y, t+1) = \int_{-\infty}^{+\infty}\int_{-\infty}^{+\infty} \overrightarrow{\overrightarrow{\Phi}} \circ \overrightarrow{\overrightarrow{A}} \cdot \overrightarrow{p}(x+\Delta_x, y+\Delta_y, t) d\Delta_x d\Delta_y, \tag{6.12}$$

where $\left(\overrightarrow{\overrightarrow{\Phi}} \circ \overrightarrow{\overrightarrow{A}}\right)_{ij} = \Phi_{ij} A_{ij}$. The elements A_{ij} of the demographic matrix $\overrightarrow{\overrightarrow{A}}$ describe the rate at which an individual in state j gives rise to individuals in state i per unit time. Similarly, the elements Φ_{ij} of the dispersal matrix $\overrightarrow{\overrightarrow{\Phi}}$ indicate the probability that an individual moves from $(x + \triangle_x, y + \triangle_y)$ to (x, y) when its stage changes from j to i. For example, any adult tree which is j years old will be $j + 1$ one year after (i.e., after t has increased to $t + 1$). Thus $A_{ij} = 1$ if $i = j + 1$. However, trees cannot move, so $\Phi_{ij} = \delta_{2D}(\Delta)$ if $i = j + 1$ (where $\delta_{2D}(\Delta)$ is the 2-dimensional Dirac delta centered at $\Delta = 0$). Indeed, a single stage could be used to represent several years in the life of an individual (as in some structured population models [19, 107]), but this would not significantly change the discussion below. In Eq. (6.12) growth and dispersal are not necessarily independent processes, in contrast to the case in the previous section. For example, note that for tree populations only seeds are dispersed, hence dispersal immediately follows reproduction [15, 106] (see also appendix C).

For clarity, let us briefly recall that the exact solution for the front speed from the evolution equation (6.12) is derived as follows by looking for constant-shape solutions for each subpopulation, $p_i(x, y, t) = w_i \exp[-\lambda(x - ct)]$. Using this into Eq. (6.12) yields

$$\exp(\lambda c)\overrightarrow{w} = \left(\int_{-\infty}^{+\infty}\int_{0}^{+\infty} \overrightarrow{\overrightarrow{\Phi}} \circ \overrightarrow{\overrightarrow{A}} \ \exp\left[-\lambda r\cos\theta\right] \ dr d\theta\right)\overrightarrow{w} \ , \tag{6.13}$$

and the exact theoretical front speed is given by [106]

$$c = \min_{\lambda} \frac{\ln\left[\rho_1(\lambda)\right]}{\lambda}, \tag{6.14}$$

where ρ_1 is the largest real of the eigenvalues of the matrix $\int_0^{+\infty} \overrightarrow{\overrightarrow{\Phi}} \circ \overrightarrow{\overrightarrow{A}} \, \exp\left[-\lambda r \cos\theta\right] \, dr d\theta$.

Given the substantial complexity of Eq. (6.13), an explicit expression for the exact front speed cannot be derived. For instance, the high lifespan of trees can lead both $\overrightarrow{\overrightarrow{A}}$ and $\overrightarrow{\overrightarrow{\Phi}}$ to be of order above 100 when applying the model to tree recolonizations [106]. For this reason, we need to make some simplifying assumptions in order to derive an approximate expression for the front speed (later we will assess the validity of our assumptions by comparing to the exact speed (6.14)). First, we assume that the following nonstructured equation [15] provides an approximately valid description of the evolution of the structured population at the leading edge of the front,

$$\begin{array}{c} p(x,y,t+T) = R_{0g} \int_{-\infty}^{+\infty} \int_{-\infty}^{+\infty} p(x+\triangle_x, y+\triangle_y, t) \\ \phi(\triangle_x, \triangle_y) d\triangle_x \, d\triangle_y, \end{array} \tag{6.15}$$

where R_{0g} is the generational initial growth rate (i.e., the average reproductive rate per individual and generation). Note that a major effect of considering the structure of the population (i.e., Eq. (6.12) instead of Eq. (6.15)) is that the reproduction of elder individuals is taken into account. However, such contribution to the population growth has been shown to play a minor role on the front speed when reproduction rates are above a certain threshold [106], because then the reproduction at the leading edge of the front is mainly produced by young individuals. Thus, if we assume a fast growth rate it is reasonable to expect that Eq. (6.12) can be approximated by the nonstructured Eq. (6.15). Next, we Taylor-expand Eq. (6.15) up to second order in time and space and obtain

$$\frac{\delta p}{\delta t} + \frac{T}{2} \frac{\delta^2 p}{\delta t^2} = \frac{(R_{0g}-1)}{T} p(x,y,t) + D\left(\frac{\delta^2 p}{\delta x^2} + \frac{\delta^2 p}{\delta y^2}\right), \tag{6.16}$$

where $D = R_{0g} < \Delta^2 > /4T$. As usual, we look for solutions with the form $p = p_0 \exp[-\lambda(x-ct)]$ with $\lambda > 0$. Using this into Eq. (6.16) yields

$$\lambda = \frac{Tc \pm \sqrt{(Tc)^2 - 4(R_{0g}-1)(DT - \frac{T^2c^2}{2})}}{2(DT - \frac{T^2c^2}{2})}, \tag{6.17}$$

and, assuming as usual that the minimum speed is the one of the front [98], we obtain

$$c = \left(\frac{2D}{T(1 + \frac{1}{2(R_{0g}-1)})}\right)^{1/2}. \tag{6.18}$$

Since we are considering high values of the reproduction rate, we assume that the condition $1 >> (2(R_{0g}-1))^{-1}$ is satisfied in Eq. (6.18). Interestingly, this finally

simplifies into the same approximate front speed as that in the previous two sections, namely

$$c = \sqrt{2D/T}. \tag{6.19}$$

It is worth to note that in Eq. (6.15) dispersal (of seeds) occurs immediately after reproduction (this is a major feature of tree populations). This is why the diffusivity D in this section (see its definition below Eq. (6.16)) depends on the growth rate R_{0g}. For the applications to postglacial recolonizations below, we consider $R_{0g} = TR_0$ (where R_0 is the average reproduction rate per tree and year). In other words, we assume that R_{0g} corresponds to the sum of the seasonal fecundities of the T reproduction events in which a parent tree is involved before individuals of the next generation become adults[‡]. Details on the empirical data for the tree species considered below, as well as the definition of the matrix elements A_{ij} and ϕ_{ij}, are presented in Appendix C.

Figure 6.3(a) shows the exact speed for the overlapping-generations model (4.30) and three values within the observed range of R_0 for the yellow poplar (*Liriodendron tulipifera)* species, which was previously used to study postglacial recolonization fronts [15, 106]. Both the exact theory and the simulations in Fig. 6.3(a) are in good agreement (the observed differences, about 7%, are due to the discretization of the space in the simulations [106]). In Fig. 6.3(a), within the observed range of T, the differences between approximate (6.5) and exact (4.30) theory are below 15% for the case $R_0 = 30$ yr^{-1} (the lower reproduction rates $R_0 = 10$ yr^{-1} and $R_0 = 3$ yr^{-1} present higher differences). However, if $R_0 \geq 10$ yr^{-1} the approximate, exact and numerical front speeds all lay within $10^2 - 10^3$ m/yr (which is the observed range for postglacial recolonizations [12]). On the other hand, long-distance dispersal events (due to atmospheric turbulence) have been shown to spread seeds along distances $\Delta \sim 10^3 - 10^4$ m for this species [16, 18][§]. The front speed dependence on the seed dispersal distance Δ is shown in Fig. 6.3(b). Remarkably, if the reactive process is fast enough (curve for $R_0 = 30$ yr^{-1}) then the approximate solution derived above, Eq. (6.19), closely agrees with the exact solution to Eq. (6.14), which is very complicated mathematically (see the discussion above). Furthermore, for $R_0 = 30$ yr^{-1} and $\Delta > 3000$ m we observe predicted speeds within the observed range for postglacial recolonizations ($10^2 - 10^3$ m/yr) [12]. Finally, in Fig. 6.3(c) we have applied our approximate Eq. (6.5) to model the Holocene invasion of the black alder *(Alnus glutinosa),* across the British Isles [49]. Obviously, the invasion predicted by Eq. (6.5) gives a circular-shaped front, corresponding to a constant speed. Although admittedly simple, this approximate front is in remarkable agreement with the observed colonization dates of the black alder, specially for the isochrones ≥ 6500 yr before present (BP). The slowdown of the observed invasion front when reaching high latitudes (< 6500 yr BP) is not surprising, because such a slowdown is observed in many tree species and could be due to adaptations to the harsher northern climate [49].

[‡]This is a smoother approach than those in some previous non-overlapping generations models, such as considering $R_{0g} = R_0$ [15, 106], or assuming R_{0g} is equal to R_0 times a mean fertile age [108].

[§]The values of Δ considered in this paper correspond to long-distance jumps, which produce a much more important effect on the front speed than short-distance jumps (see Ref. [15]).

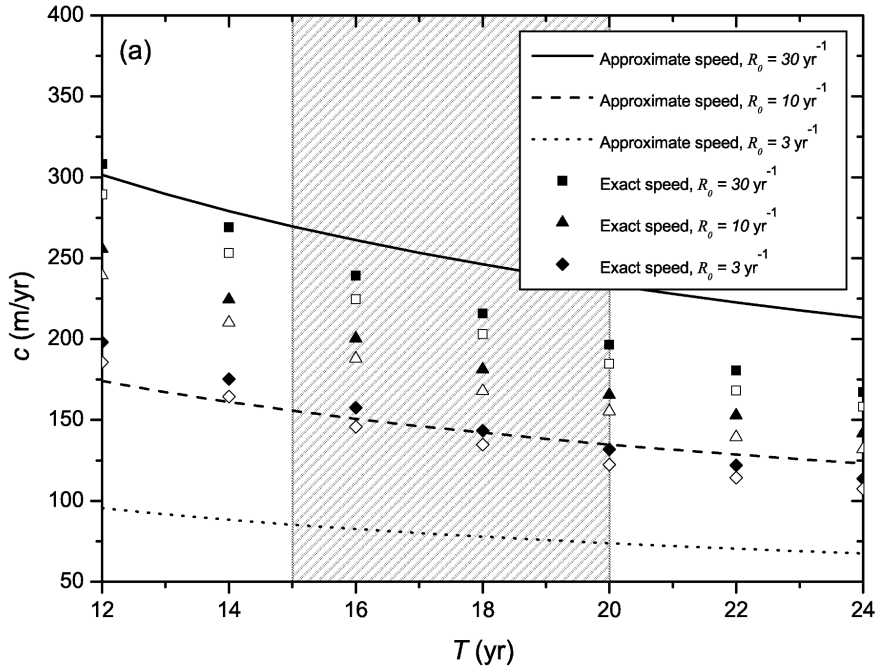
(a)
Approximate speed, R_0 = 30 yr^{-1}
Approximate speed, R_0 = 10 yr^{-1}
Approximate speed, R_0 = 3 yr^{-1}
Exact speed, R_0 = 30 yr^{-1}
Exact speed, R_0 = 10 yr^{-1}
Exact speed, R_0 = 3 yr^{-1}
c (m/yr)
T (yr)
400
350
300
250
200
150
100
50
12
14
16
18
20
22
24

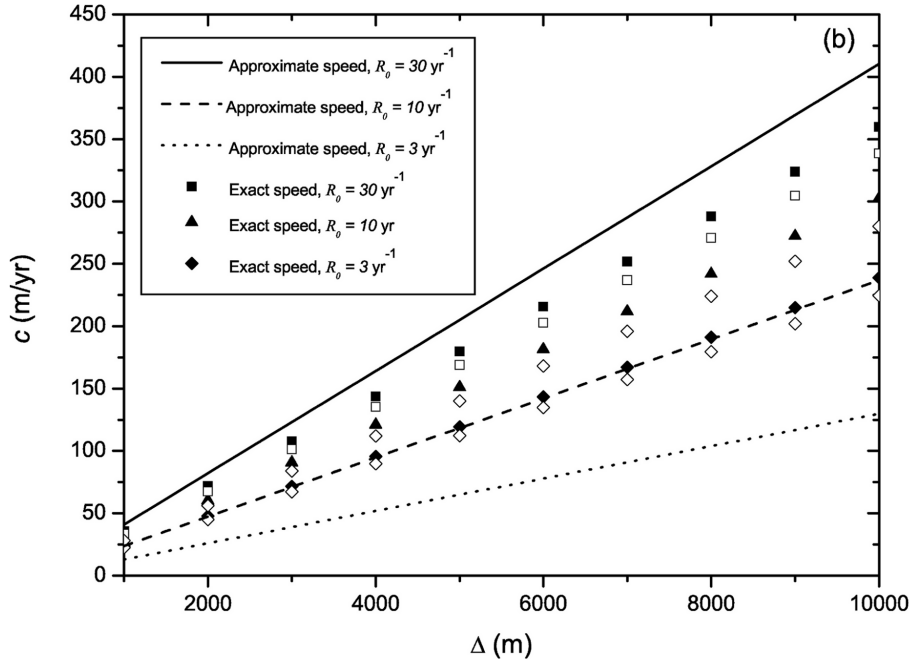
(b)
Approximate speed, R_0 = 30 yr^{-1}
Approximate speed, R_0 = 10 yr^{-1}
Approximate speed, R_0 = 3 yr^{-1}
Exact speed, R_0 = 30 yr^{-1}
Exact speed, R_0 = 10 yr
Exact speed, R_0 = 3 yr^{-1}
c (m/yr)
Δ (m)
450
400
350
300
250
200
150
100
50
0
2000
4000
6000
8000
10000

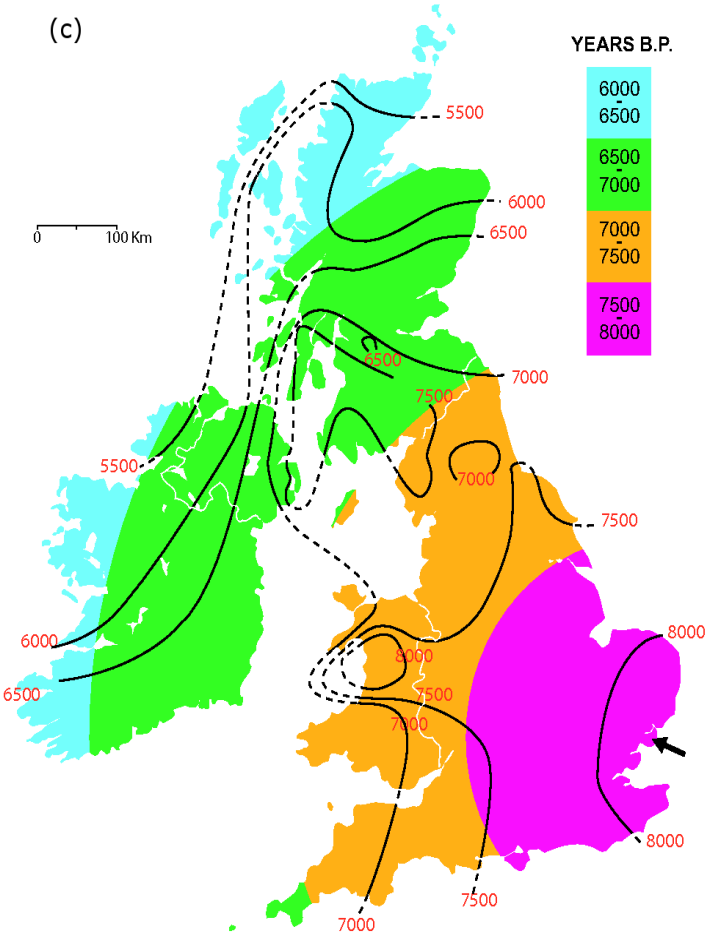

Figure 6.3: **Postglacial recolonizations**. a) Invasion front speed versus lag time for the yellow poplar($\Delta = 6000$ m). The solid, dashed and dotted curves stand for the approximate $c = \sqrt{2D/T}$, for the cases $R_0 = 30$, 10 and 3 yr^{-1}, respectively. The probability $(1 - p_e)$ for long-distance dispersals (with $p_e = 0.99798$ [15]) has been taken into account when computing $< \Delta^2 >$. Full (empty) squares, triangles and rhombus correspond to the exact theoretical solutions (numerical simulations) for $R_0 = 30$, 10 and 3 yr^{-1}, respectively. The hatched rectangle is the observed range of T [46]. Additional information on simulations and empirical data is provided in appendix C. b) Invasion front speed versus seed dispersal distance. Lines and symbols correspond to the same cases in a), but for $T = 18$ yr [46]. c) Black alder post-glacial recolonization of the British Isles (color online). Colored regions depict the predicted arrival times for an invasion with the constant speed $c = 462$ m/yr, computed from Eq. (6.5) with $T = 6$ yr [47], $\Delta = 6500$ m *, $p_e = 0.99798$ and $R_0 = 30$. The black isochrone curves correspond to those inferred from pollen data by H. Birks in Ref. [49]. The arrow indicates the direction of arrival of black alder trees into the British Isles [49].

6.4 Discussion

When studying the three systems presented above, we observe the following general trend: the higher the reproduction rate [i.e., Y in Fig. 6.1, a in Fig. 6.2, and R_0 in Figs. 6.3(a) and 6.3(b)], the closer our approximate speed $c = \sqrt{2D/T}$ is to the corresponding exact solution. For virus infections, both the VSV and the T7 display high enough values of Y and Eq. (6.5) agrees well with observations. In contrast, when introducing the hypothetical low-yield case where $Y = 5$ (circles in Fig. 6.1), the approximate speed does not provide accurate results for $T < 60$ min. This is not a problem at all (because such values of Y and T are far below the observations for T7 [56])¶.

The approximate speed (6.5), originally derived for a very special case (namely focal infection systems), has been shown here to be valid for a wide range of systems, from nonstructured single-species systems (Sec. 6.2) to rather complicated structured systems (Sec. 6.3). In all of those cases, we have also shown that observations agree reasonable well with our approximate equation (6.5). Thus, we find many substantially different systems with the same front speed (6.5) and, remarkably, this makes all parameter values related to the reactive processes (a, Y, k_1, k_2, R_0, etc.) irrelevant. Obviously, this enormously simplifies the task of comparing theory and experiment.

In this paper we have analyzed a wide variety of propagating fronts in biophysical systems, where the lag time T plays an important role in the system dynamics. We have shown that the approximate speed $c = \sqrt{2D/T}$ provides convenient results to explain the advance of rather different fronts such as several virus infections, the Neolithic transition and postglacial tree recolonizations. We have noted that our approximate speed $c = \sqrt{2D/T}$ is valid if high values of the reproduction rate are assumed. This suggests Eq. (6.5) could be a general trend in front propagation. Future work could report further applications of our simple approximate speed to other systems in which a lag time is important, e.g. crystallization fronts [109], combustion fronts (where the ignition time plays the role of the lag T) [110], etc.

6.5 Appendix A: Exact equations, numerical simulations and empirical data for virus infections

In the main text, Eqs. (1)-(4) are used to model the invasion front of several focal infection systems (then $[V]$ replaces p in Eq. (1)). In such experiments cells are not able to diffuse because they are immobilized by agar [56]. Hence, Eqs. (2) and (3) contain reactive but not diffusive terms. Viruses are the only species able to diffuse in the system, see

*Seeds of *Alnus glutinosa* are typically water-dispersed [49]. However, long-distance dispersals are rare events which produce long migrations independently of the usual dispersal agency of the seed [16]. Therefore, as in the case for *Liriodendron tulipifera* (Fig. 3a and 3b), migrations in the range $10^3 - 10^4$ m are expected for the *Alnus glutinosa*.

¶However, this was exactly the expected result, since high values of Y and T were assumed to derive Eq. (6.5) [102].

Eq. (1). In order to compute the invasion speed, we introduce a frame moving with the front and look for solutions depending only on the new variable $z \equiv r - ct$, where $c > 0$ is the front speed. As usual, we linearize our equations (1)-(4) around the unstable steady state $([V], [C], [I]) = (0, C_0, 0)$. Hence we consider $([V], [C], [I]) = (\epsilon_V, 1 - \epsilon_C, \epsilon_I)C_0$ at the front edge, where $\overrightarrow{\epsilon} = (\epsilon_V, \epsilon_C, \epsilon_I) = \overrightarrow{\epsilon}_0 \exp(-\lambda z)$. For non-trivial solutions $(\epsilon_V, \epsilon_C, \epsilon_I) \neq (0, 0, 0)$ to exist, the determinant of the matrix corresponding to the linearized set of three evolution equations must vanish. Therefore, the following characteristic equation must be satisfied

$$\lambda^3 + \frac{-\alpha^2 c^2 (1-\beta) + 1}{\alpha c(1 - \alpha^2 \beta c^2)}\lambda^2 + \frac{\kappa(\beta\kappa - 1) + \beta\kappa Y - 1}{1 - \alpha^2\beta c^2}\lambda + \frac{(1 - \beta\kappa)(\kappa Y - \kappa)}{\alpha c(1 - \alpha^2\beta c^2)} = 0, \quad (6.20)$$

where $\alpha = (k_2 D)^{-1/2}$, $\beta = T/2$ and $\kappa \equiv k_1 C_0/k_2$.

According to marginal stability analysis [98], the wave front speed can be finally calculated numerically from

$$c = \min_{\lambda > 0}[c(\lambda)]. \quad (6.21)$$

This summarizes the computation of the exact infection front speed from Eqs. (1)-(4) (full symbols in Fig. 6.1). Usually dimensionless variables are used, but the final equations for the front speed are still rather complicated. Details, exact and approximate results can be found in our previous Ref. [102].

Besides the exact speed summarized above (full symbols in Fig. 6.1) and the approximate speed $c = \sqrt{2D/T}$ (curves in Fig. 6.1), simulated speeds have been obtained by integrating numerically the set of Eqs. (1)-(4) (empty symbols in Fig. 6.1). In order to do so, we have used finite differences to approximate the partial derivatives in Eqs. (1)-(4). Typical values for the space and time steps used in our simulations were below 1 μm and below 1 second, respectively. All simulations considered the initial conditions $[C] = C_0$ and $[I] = 0$ everywhere, and a viral concentration of $[V] = 9.3 \times 10^8$/ml in a small central region with a radius of 0.075 cm [111] (this region represents the initial inoculum starting the focal infection).

In this paper we have studied infections of both VSV and T7 viruses (including mutants for the latter). VSV infections infect mammalian cells, whereas T7 viruses infect bacteria. We have used VSV and T7 infections because these are the only ones for which front speeds have been measured experimentally [56, 58]. Table 1 contains the parameter values used to compute the invasion speed.

For VSV, the parameter values in Table 1 are the same as in Ref. [102] (to the best of our knowledge, no experimental data on the adsorption rate of the VSV are available, but the front speed is independent of the value of k_1 for several orders of magnitude [102]). For the wild type of T7, we use the values of k_1, k_2 and Y derived in Ref. [10] from experimental data. Using the same procedure as in Ref. [10], we have computed k_2 and Y for the T7 p005 mutant from the experimental data in Ref. [56] (the other parameter values are the same as for the wild T7 strain). The last column in Table 1 corresponds to a low-yield hypothetical case of the T7 wild strain, which

	VSV	**T7 (wild)**	**T7 (p005)**	**T7 (low-yield hypothesis)**
D (cm^2/hr)	1.44×10^{-4}	$8.55 \cdot 10^{-5}$	$8.55 \cdot 10^{-5}$	$8.55 \cdot 10^{-5}$
k_1 (cm^3/hr)	1.4×10^{-10}	$7.74 \cdot 10^{-8}$	$7.74 \cdot 10^{-8}$	$7.74 \cdot 10^{-8}$
k_2 (hr^{-1})	2.47	83.4	44.5	83.4
Y	4389	34.5	63.6	5

Table 6.1: Parameter values applied to compute invasion speeds of VSV and T7 infections in the main text, using both analytical solutions and numerical integrations of Eqs. (1)-(4).

appears in Fig. 6.1 in the main text and is considered only to understand better the results there. The values of the diffusivity D in Table 1 are based on the diffusivity of the P22 virus in agar, $D = 1.44 \cdot 10^{-4}$ cm^2/hr [10]. Since the P22 virus is similar in size and shape to the VSV [102] and T7 viruses [10], it provides convenient approximations for the diffusivities of the viruses analyzed here. In Ref. [10] it was noticed that the presence of host cells in the medium actually hinders virus diffusion. To account for this effect, a convenient correction factor for the diffusivity of the virus must be computed (see Sec. V in [10]). In the present paper we consider the data from Ref. [56], so the bacterial concentration is $3 \cdot 10^6$ /ml, and the maximum possible bacterial concentration is 10^7/ml. Thus, after taking into account the hindered-diffusion correction factor in [10] we obtain $D = 8.55 \cdot 10^{-5}$ cm^2/hr for T7 viruses. In the case of VSV, experiments [58], there are no data indicating any hindered diffusion effect, hence in Table 1 we have considered free diffusion for VSV (as in Refs. [102, 111]). According to the data from Ref. [56], the speed range for the T7 is 0.016 - 0.027 cm/hr [from the minimum and maximum values in figs 4(b) and 4(c) in this reference]. Note that the range of speed of the mutant p005 [Fig 4(b) in Ref. [56]] widely overlaps with the range for the wild type [Fig 4(c) in Ref. [56]]. Thus, in our Fig. 6.1, we have used a single range for T7 viruses. In our previous paper [102] we estimated the experimental speed of VSV infections from the data in Fig. 2(b) in Ref. [58]. This led us to the experimental range of 0.066-0.08 cm/hr [102]. However, additional data on infection profiles of the same experiments are available in Fig. S3 in Ref. [111], so in Table 1 we take into account that a more realistic minimum experimental speed is 0.056 cm/hr (from the evolution of the experimental radial profiles in Ref. [111]). The maximum value for the experimental speed is the same we proposed in Ref. [102], namely 0.08 cm/hr.

6.6 Appendix B: Numerical simulations for the Neolithic transition

For the numerical simulations in Fig. 6.2, we have used a very simple model proposed in Ref. [30]. We consider a 2D square grid with the initial condition $p(x, y, t = 0) = p_{\max}$ at the central node, and $p(x, y, t = 0) = 0$ everywhere else in the square grid. Each time step in the simulations represents an interval time of $T = 1$ generation. At every

time step, the population density is equally distributed into the 8 nearest neighbors, so the mean-squared displacement is

$$< \Delta^2 >= \frac{1}{8} \sum_{j=0}^{1} 4 \left[d^2 + (jd)^2 \right], \tag{6.22}$$

where d is the distance between two neighboring nodes. Also, we compute the effect of population growth at each node and each time step by applying the solution for the logistic growth given by Eq. (6.11),

$$R_T[p(x,y,t)] = \frac{p(x,y,t) p_{\max} e^{aT}}{p_{\max} + p(x,y,t)\left(e^{aT} - 1\right)}. \tag{6.23}$$

Finally, the population density at each node for the next step $p(x, y, t+1)$ is computed as the sum of $R_T[p(x,y,t)]$ and the dispersive contribution described above.

6.7 Appendix C: Matrix elements, empirical data and numerical simulations for postglacial tree recolonizations

The following considerations have been applied to the matrices in the structured-population model for tree recolonizations in Sec. 6.3. The demographic matrix $\overrightarrow{\overrightarrow{A}}$ describes reproduction and aging of the population as follows. The elements of $\overrightarrow{\overrightarrow{A}}$ take into account that (i) each adult tree produces yearly a surviving number of seeds R_0 and (ii) individuals become one year older by switching its stage from j to $j+1$ at each time increment $t \dashrightarrow t+1$. Thus, $\overrightarrow{\overrightarrow{A}}$ is written as [106]

$$A_{ij} = \begin{cases} R_0 \text{ if } i = 1,\ j \geq T \\ 1 \text{ if } i = j+1 \\ 0 \text{ otherwise} \end{cases}, \tag{6.24}$$

where R_0 is the mean fecundity (i.e., number of seeds that survive into an adult tree) per parent tree and year.

The elements Φ_{ij} of the dispersal matrix $\overrightarrow{\overrightarrow{\Phi}}$ describe the rate of every possible conversion of $p_i(x + \triangle_x, y + \triangle_y, t)$ into $p_j(x, y, t+1)$. Since $\overrightarrow{\overrightarrow{\Phi}}$ must restrict dispersal to new individuals (trees do not move but only disperse seeds), the elements of $\overrightarrow{\overrightarrow{\Phi}}$ are [106]:

$$\Phi_{ij} = \begin{cases} \phi(\Delta_x, \Delta_y) \text{ if } i = 1,\ j \geq T \\ \delta_{2D}(\Delta) \text{ otherwise} \end{cases}, \tag{6.25}$$

where $\delta_{2D}(\Delta)$ is the 2-dimensional Dirac delta centered at $\Delta = 0$. The dispersal kernel $\phi(\triangle_x, \triangle_y)$ is the probability per unit area that a seed falling from a parent tree located at $(x + \triangle_x, y + \triangle_y)$ reaches the ground at (x, y)) [106].

For the computations in Figs. 6.3(a) and 6.3(b) in the present paper, we have considered the same isotropic kernel as in Ref. [106], i.e. that new seeds of the yellow poplar either grow in the same location as the parent tree (with probability $p_e = 0.99798$ [15]) or they are dispersed to a distance $r = \Delta$ (with probability $1 - p_e$). Moreover, the annual seed production f of the yellow poplar is of the order of 10^4 seeds dispersed / tree yr [18, 46]. According to field observations in sites close to those where the dispersal kernel was measured, the yellow poplar postdispersal seed-to-adult survival is in the range $0.00 - 0.06\%$ [18, 112]. In the present work we have considered the mean value of this survival rate, i.e., $s = 0.03\%$. Thus, we estimate the net reproductive rate, $R_0 = fs$, to be in the range of $3 - 30$ seeds / tree yr for the yellow poplar.

To the best of our knowledge, there is no available data on the long-distance dispersal kernel of the black alder. However, because of long-distance dispersals are usually driven by extreme climatological conditions (and they are independent of the usual dispersal agency of the seed) [16], we expect the persistence p_e of the black alder to be of the same order of magnitude than the one for the yellow poplar. Thus, we have used $p_e = 0.99798$ [15] in the isochrone map for the black alder in Fig. 6.3(c). The observed annual seed production f of this species is of the order of the order of 10^4 seeds dispersed / tree yr [47]. For the case of the black alder, we consider the survival probability $s = 0.03\%$ (i.e., the same considered for the seeds of the yellow poplar), since we are not aware of any specific observed range for the black alder. This yields an estimated net reproductive rate, $R_0 = fs$, in the range of $3 - 30$ seeds / tree yr for the black alder. Since our approximate speed $c = \sqrt{2D/T}$ assumes high values of the reproduction rate (see discussion above), in Fig. 6.3(c) we have considered the highest value in this range, i.e., $R_0 = 30$ seeds / tree yr.

Results from molecular dynamics simulations have been presented as empty symbols in Figs. 6.3(a) and 6.3(b). Our computer program considers a 2D grid where an age-structured population density is computed. Initially $p(x, y, 0) = 1$ at $(x, y) = (0, 0)$ and $p(x, y, 0) = 0$ elsewhere. At each time step, we compute the new number density of trees $p(x, y, t + 1)$ at all nodes. The main features of this model (immature individuals cannot reproduce, etc.) are properly taken into account (we refer the interested reader to Ref. [106] for further details about these molecular dynamics simulations).

6.8 Acknowledgements

Discussions with N. Isern and T. Pujol are acknowledged. This work was supported by the MICINN-FEDER (projects SimulPast-Consolider-CSD-2010-00034, FIS-2009-13050 and FIS-2012-31307) and by the Generalitat de Catalunya (Grup consolidat 2009-SGR-374).

Chapter 7

Effects of punishment in a mobile population playing the prisoner's dilemma game.

This chapter is an exact transcription of the contents of the following paper:

Amor, D. R. & Fort, J. 2011 Effects of punishment in a mobile population playing the prisoner's dilemma game. *Phys. Rev. E* 84, 066115.

Abstract We deal with a system of prisoner's dilemma players undergoing continuous motion in a two-dimensional plane. In contrast to previous work, we introduce altruistic punishment after the game. We find punishing only a few of the cooperator-defector interactions is enough to lead the system to a cooperative state in environments where otherwise defection would take over the population. This happens even with soft nonsocial punishment (where both cooperators and defectors punish other players, a behavior observed in many human populations). For high enough mobilities or temptations to defect, low rates of social punishment can no longer avoid the breakdown of cooperation.

PACS numbers: 89.75.Fb, 89.65.-s, 87.23.Kg

7.1 Introduction

The appearance and maintenance of cooperation is one of the most important enigmas set out by evolutionary biology [113]. A problem of utmost importance is that while an individual can benefit from mutual cooperation, it can often do even better by exploiting the cooperative efforts of others (and this, in turn, tends to destroy cooperation) [37]. Evolutionary game theory has proved to be a major formalization tool in this context, so different games have been used in many theoretical and experimental works, and the subject has rapidly jumped to other domains such as statistical physics and mathematics [114–118]. In order to model biological systems and human behavior [37, 113], the

prisoner's dilemma (PD) game has become especially well known and studied because in this game the best strategy for single players becomes the worst one for the community (see below).

The PD is a game between two individuals, where each one can choose from whether to cooperate (C) with or to defect (D) from his opponent. The corresponding payoff matrix of an interaction between two players is given by

$$\begin{pmatrix} R & S \\ T & P \end{pmatrix}, \tag{7.1}$$

where R denotes the payoff each player receives if both cooperate, S is what a cooperator receives when he is exploited by a defector (who gains T in this particular interaction), and P is the payoff for two defectors playing one against another. The payoffs are ordered as $T > R > P \geq S$, so rational players would always play defection (because it pays more regardless of the opponent's decision). But this rationality makes both players receive only P instead of the reward $R > P$ which both players would have accumulated by cooperating, hence the dilemma. With two individuals destined never to meet again, the only rational strategy is to defect [37].

The main idea of evolutionary game theory hinges on individuals playing multiple rounds. This simulates real-world interactions better than one-shot games and in some settings leads to the survival of cooperation. In 1981 the Axelrod computer tournaments [37] analyzed multiple strategies competing in the repeated PD game, with individuals remembering their previous interactions. They found defection is not the only stable strategy. In contrast, some strategies lead to higher average scores than defection (the most successful strategy was *tit for tat*, i.e. simply cooperating on the first move and then doing whatever the other player did in the preceding move). These results stimulated a wealth of work that still continues today [67, 119, 120]. In 1992 Nowak and May [39] introduced the repeated PD game into a simulated population with its individuals bound to lattice sites of a two-dimensional spatial array. They found cooperators and defectors both persist indefinitely (in shifting clusters), without the need to assume the use of complicated strategies because neither individual remembers previous interactions (each player was either C or D, and after each round each lattice site was occupied by the player with the highest payoff among the previous owner and its neighbors). A huge amount of work has been undertaken ever since concerning evolutionary games on graphs [114], exploring many diverse combinations of realistic network topologies (link dynamics) and strategy update rules that lead to the survival of cooperation [38, 121–128].

In a recent paper, Meloni *et al.* explored the effects of mobility in a population of PD players [44]. Moreover, the authors introduced an innovative kind of migration. In spite of the number of recent models that take into account migration processes in networks [124, 128–131], Meloni *et al.* noted that the continuous motion of individuals (in contrast to the discontinuous jump of individuals bound to lattice sites of a grid) was an unexplored situation of practical relevance. It could also be important in several applications, e.g. in designing cooperation-based protocols for wireless devices such as robots [132] and in modeling the dynamics of interacting human populations with

different cultural traits, e.g. in prehistoric transitions [1]. Therefore, in this paper we will deal with systems with continuous mobility, as proposed in Ref. [44]. Such systems exhibit only two stable attractors: those in which the whole population either cooperates or defects [44].

In addition to spatial structure, there exist other mechanisms that provide important aids to cooperators in their fight against free riders [121]. In this paper, we focus on the effects of punishing in a population with continuous motion. Punishment is a negative incentive by which some players (punishers) impose fines upon some of their coplayers. Punishers usually pay a cost to punish [42]. Why do then individuals choose to punish others [133, 134]? Although there is not an ultimate answer available, it is widely accepted that emotions and moral sentiments play an important role in human decisions that can go beyond the maximization of their income [45, 67, 71, 120, 133, 135–137]. Similarly, some humans also reward their cooperative partners [138]; thus several papers have dealt with positive incentives. Some recent models have shown, for example, that the appropriate dose of the carrot [139] or the convenient combination with the stick when agents are opportunistic [140] can notably enhance the triumph of cooperation.

Punishment can be very costly in pairwise interactions; thus in real life punishment is usually repressed by institutions holding law and order. But some pairwise interactions with punishment obviously exist in real life, both in small-scale and large-scale societies [42]. Still, in agreement with the relative rarity of pairwise punishment, traditionally, the cooperation-enhancing effects of punishment have been often analyzed within the public goods game [67, 71, 141, 142]. Very recently, this n-person game has provided the scenario where the following effects have been studied: (i) the strategy D punishes D (instead of the usual C punishes D) also helps to defeat free riders [116], (ii) small mutation rates accelerate the spreading of costly punishment [143], and (iii) spatial structure is responsible for several kinds of coexistence between cooperators, moralists (cooperators who punish defectors), defectors, and immoralists (defectors who punish other defectors) [144]. In this paper we have opted for a simpler setup and considered pairwise interactions only. Although less commonly used, two-person games also have been employed in punishment studies, especially in experimental work. One of the most representative examples is the ultimatum game [135, 145], where the rejection of an offer is indeed a kind of costly punishment. Rewarding and punishing human behavior has also been tested by using sequential PD games (often called gift exchange or trust games) [146]. In other cases, the payoff matrix of the PD game has been modified in order to include three types of players: cooperators, defectors, and punishers [147]. Moreover, the use of pairwise interactions is also present in models with incentive strategies [139].

Punishment is often considered a different strategy from pure cooperation or pure defection [116, 143, 144]. In this paper, we do not consider punishers to have a different strategy than other players. Players are either cooperators or defectors. After a given interaction, we introduce a probability to punish the corresponding coplayer. This is a simple way to model that a certain portion of the interactions is followed by negative incentives, but players do not become obsessed in punishing every partner they are not comfortable with (since it could be extremely costly for themselves). Besides social

punishment (C punishes D) we will also analyze what we call non-social punishment (C punishes C, D punishes C, or D punishes D), as suggested by recent experiments in many human populations around the world [45].

To summarize, in this paper we introduce social and nonsocial punishment effects into a model where players can move continuously in a two-dimensional (2D) world. Moreover, no punishment strategies are considered; instead, we deal with probabilities that different interactions between agents are followed by punishment. In particular, we find that social punishment helps to maintain cooperation in extreme environments, even with such a high mobility or temptation to defect that the system would otherwise be completely invaded by defectors. We shall also find that the benefits of social punishment are remarkable, even when some degree of non-social punishment is present in the game.

This paper is organized as follows. In Sec. 7.2 we present the main features of the model (including mobility rules, network of interactions, evolutionary dynamics, social punishment, and nonsocial punishment). Section 7.3 is devoted to explaining the main effects of considering a nonmobile population in our model. In Sec. 7.4 we present the general results of our simulations (phase diagrams showing the dependence on the relevant parameters of the model). Finally, our concluding remarks are presented in Sec. 7.5.

7.2 The model

In this section we explain the rules that drive the evolution of the system. We study a population of $N = 1000$ individuals living in a square plane of size L. As in Ref. [44], periodic boundary conditions are imposed at the ends of the square (this makes the square equivalent to a toroidal surface, thus avoiding border effects). Simulations are governed by three groups of rules concerning the motion rules, the network of interactions and the evolutionary dynamics. The first two groups of rules we use here have the same properties of the original model [44], but the evolutionary dynamics are notably different because we introduce a probability of punishing the opponent. Simulations perform sequentially the three sets of rules at each time step t. In the following three sections, we detail these three types of rules in the model.

7.2.1 Motion rules

At the beginning of each round, every player moves a fixed distance in a random direction. Hence, the position of a given individual i ($i = 1, 2, ...N$) is changed as

$$\mathbf{x}_i(t+1) = \mathbf{x}_i(t) + \mathbf{v}_i(t), \tag{7.2}$$

where $\mathbf{v}_i(t) = [v\cos\theta_i(t), v\sin\theta_i(t)]$ is the speed of the player i. The direction of the speed is determined randomly as

$$\theta_i(t+1) = \eta_i, \tag{7.3}$$

where η_i are N independent random variables chosen at each time with uniform probability in the interval $[-\pi;\pi]$.

As in Ref. [44], we consider that the module of the speed v is constant for all agents, so v is one of the relevant parameters of the system. At $t = 0$, both a random position in the square and a random initial direction of movement is assigned to every player.

7.2.2 Network of interactions

After movement, every player establishes its network of interactions. An agent i will consider the player j as his or her neighbor if j is within a certain radius of interaction r. First, the Euclidean distance d_{ij} between players is computed. Then, if $d_{ij} < r$, we say that i and j are neighbors (and will interact following the rules in the next section). Without loss of generality, in all the simulations presented here we have set $r = 1$. The instant network of contacts can be defined by a graph that links its nodes (individuals) with the current web of neighbors. Note that such a graph changes at every round t due to the motion and neighborhood updating of the agents. The mean degree of the graph is $\langle k \rangle = \rho\pi r^2 = \rho\pi$, where $\rho = N/L^2$ is the population density (see the work by Meloni *et al.* [44] for this and other topological features of the graph). The dependence of the system properties on the value of ρ was already analyzed in Ref. [44], Fig. 2 *. Therefore, in this paper we have used the value $\rho = 1.30$ (as in Ref. [44], Figs. 1, 3 and 4) †.

7.2.3 Evolutionary dynamics

In this section we summarize the rules regarding the interaction between agents and their strategy updates.

At each time step t, every individual plays once a PD game with each of his neighbors. The payoff matrix of the game is presented in Eq. (7.1). As usually done in recent studies (see, e.g., Ref. [44]), we choose $R = 1$, $P = S = 0$, and $T = b > 1$. The payoffs obtained from the multiple interactions are accumulated by each player during the round. In the first round ($t = 0$), the two possible strategies (C or D) are equally distributed among the population. Although in other works each individual can play different strategies against his multiple opponents, following Ref. [44] here we consider the simple case where agents can only choose to cooperate with or to defect from all of his neighbors. This will make it easier to focus our attention on the effect of punishment.

In contrast to Ref. [44], after every PD interaction is performed, we consider that each player has the opportunity to punish his opponent if he is not satisfied with the outcome of the game. In order to simulate this circumstance, in Sec. 7.2.4 we will allow cooperators to punish defectors with probability p_s, representing social punishment, i.e.,

*For too low values of ρ, cooperators cannot form clusters, and in the final state only defectors survive. For too high values of ρ the agent's neighborhoods resemble a well-mixed population in which cooperation is again eventually destroyed. See Fig. 2 in Ref. [44].

†See footnote *.

the intention to promote a cooperative society where defectors have a bad reputation. In Sec. 7.2.5, we will extend the model to allow a nonsocial type of punishment: with probability p_a, not only will defectors punish their coplayers (irrespective of their strategy) but cooperators will also act against other cooperators (representing other human motives like revenge or preventive strikes [45, 67]). When a punishment action occurs (either in the social or in the nonsocial case), the punisher pays a cost of 1 unit of his accumulated payoff in order to reduce the payoff of the punished player by 3 units (this rate has been used in previous human experiments, e.g., in Ref. [45], although harder rates where the punished player loses 4 units instead of 3 have been also studied [67]).

Finally, after all games have been played and the corresponding punishments have been executed, it is time for the agents to update their strategies. As in Ref. [44], every agent will compare his own payoff with that of a randomly chosen neighbor, and then he will decide whether he keeps playing the same strategy in the next round or not, as follows. If individual i and the chosen neighbor j use the same strategy, nothing happens. In the opposite case, and provided that j has accumulated higher gains in the current time step, individual i will adopt the strategy of j with the following probability [44]:

$$\Pi_{ij} = \frac{P_j - P_i}{\max\{k_j, k_i\}\, b}, \tag{7.4}$$

where P_j and P_i are the payoffs accumulated by players j and i, respectively. In Eq. (7.4) k_j and k_i stand for the instantaneous number of neighbors (i.e., number of players within the circle of radius r) that players j and i have, respectively. This updating process is done synchronously for all individuals in the system. Finally, the payoffs of all individuals are reset to zero, and the next round can start as explained above.

In our simulations, we have found that the system has only two stable states, as in the original model without punishment [44]. These two attractors are reached when either cooperation or defection is played by all agents. Moreover, high values of v or b destroy cooperation when no punishment is considered, in agreement with Ref. [44].

7.2.4 Social punishment

In order to introduce social punishment into our model, we have allowed cooperators to punish altruistically defectors as a separate action after the PD interaction. We do not assume that cooperators always punish their opponents, just that there is a probability of punishing socially after each cooperator-against-defector (C-D) interaction. With probability p_s the cooperator will incur a cost of 1 payoff unit to diminish the defector payoff by 3 units.

Figure 7.1 sheds some light on the implications of such a behavior acting directly against freeloaders. Figure 1(a) shows the evolution of the average level of cooperation $< c >$, defined as the average fraction of cooperators, for $v = 0.2$ and $b = 1.1$. The dashed line shows how a population where no punishment is allowed evolves to a completely defector system. However, the population can be driven to the maximum cooperation

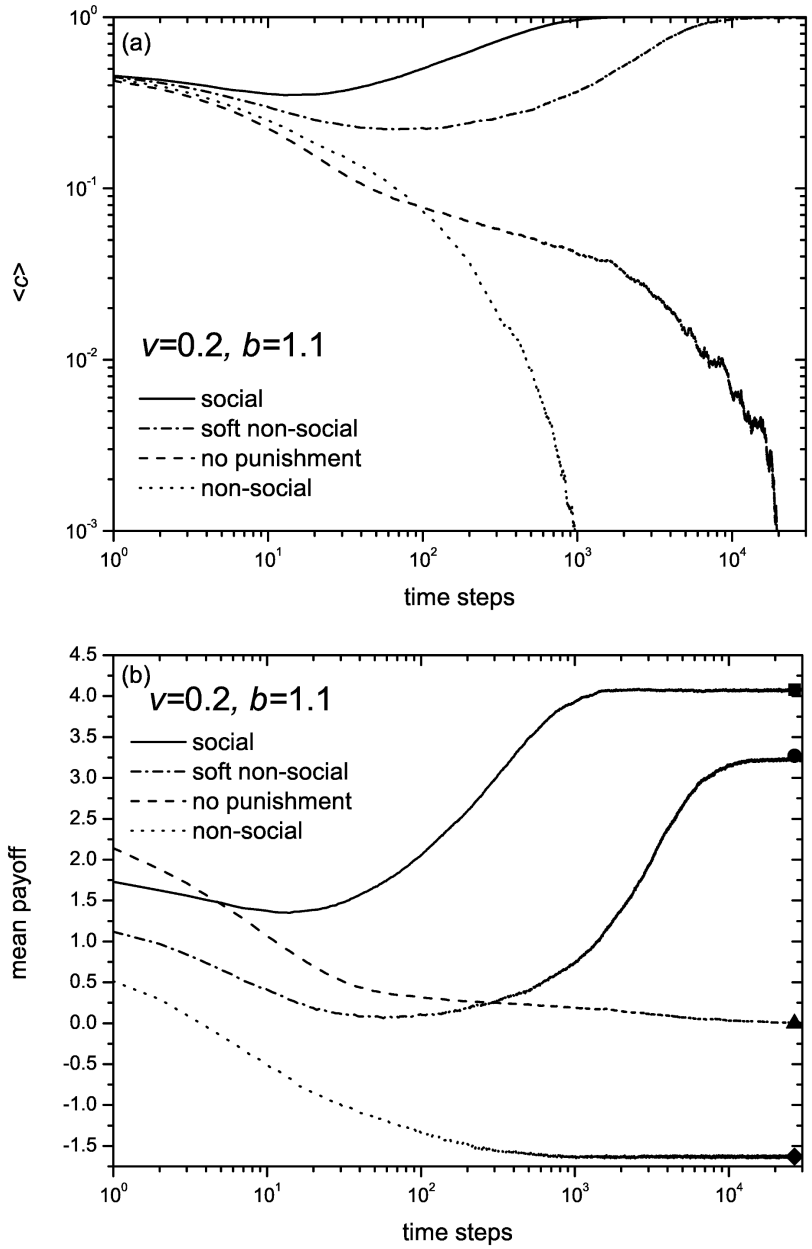

Figure 7.1: **(a)** Average level of cooperation $< c >$ (defined as the average fraction of cooperators) as a function of time (or rounds of the game). Simulations have been performed for a population of $N = 1000$ individuals, $\rho = 1.30$, $b = 1.1$, and $v = 0.2$. The solid line depicts the evolution for a population where social punishment is allowed (with $p_s = 0.1$). The dash-dotted line shows the evolution of the same population in a soft nonsocial environment, where $p_s = 0.1$ and $p_a = 0.05$. The dashed line stands for the case where punishment is not allowed at all. Finally, the dotted line shows a non-social system where $p_s = 0.1$ and $p_a = 0.1$. Results are averaged for 100 simulations. **(b)** Average payoff per player as a function of time for the same cases presented in Fig. 7.1(a). The symbols depict the asymptotic theoretical value for the average payoff. The square is for the social case, the circle stands for the soft nonsocial system, the triangle is for the case without punishment, and the rhombus is for the nonsocial system.

fraction if some degree of social punishment is present (solid line). Note that only a 10% of the C-D interactions are followed by a punishing action ($p_s = 0.1$) in this case. Hence, we have seen that a relatively low dose of social punishment can introduce critical advantages for cooperators.

7.2.5 Nonsocial punishment

Anger, revenge, and preventive strikes are only a few motives [45] that can inspire humans to punish, even if this action plays against the benefits of the community and the punisher himself. In this section, we will study the effects of this kind of punishment on the evolution of the population. We thus consider a type of punishment different from that explained in Sec. 7.2.3. We will call it nonsocial punishment.

Analogously to the social punishing probability p_s introduced above, we define the probability of punishing nonsocially as p_a. While p_s is the probability that a cooperator punishes a defector after a C-D interaction, p_a applies to any interaction different from a C-D interaction (see Sec. 7.2.3). This agrees with the definition of antisocial punishment in the paper of Herrmann *et al.* [45] that has especially inspired our work, but in other papers antisocial punishment is strictly defined as the punishment of cooperators [141]**. Because of this, we use the term nonsocial rather than antisocial. The dotted line in Fig. 7.1(a) depicts the evolution of the population in a highly nonsocial environment where $p_s = p_a = 0.1$: no matter which players are engaged, 10% of the interactions are followed by a punishing action. We can see how in this case the system favors defection, as this strategy is quickly adopted by the whole population. Therefore, nonsocial punishment works directly against the benefits of social punishment, as it would be expected intuitively [compare with the social case represented by the solid line in Fig 7.1(a)].

Although both social and nonsocial punishment are found in human communities, the first one is perceived to be more rational. Imposing a fine on someone who contributes less than you (social punishment) is easily justified because you find her or his behavior unfair. In contrast, punishing nonsocially means that you attack someone that has conducted himself (at least) as properly as you in the game; hence you do not tolerate your own behavior. As a result, human players are usually found to invest higher amounts in social punishment ‡,‡. To simulate this effect, we have performed

**The definition of nonsocial punishment in this article coincides with the definition of antisocial punishment in Ref. [45]. In the work of Herrmann *et al.* [45], punishing antisocially embraces penalizations against those who contributed equally or more than you in the game. The public goods game was used in Ref. [45]. Note that when playing the PD game, this definition covers only three possibilities: a cooperator who punishes another cooperator or a defector who punishes any coplayer (either another defector or a cooperator). These are the only three possibilities that embrace the nonsocial punishment defined in our paper.

‡See footnote **.

‡See, for example, Fig. 1 in Ref. [45]. Among the 16 comparable participant pools around the world presented there, 13 of them showed notably higher mean expenditures in social punishment than in nonsocial one. Indeed, 11 of those participant pools invested in social punishment more than twice that invested in nonsocial punishment (compare the first 11 participant pools in Ref. [45], Fig. 1, with

simulations with $p_s \neq p_a$. Note that this does not mean the total number of social punishing actions in the system exceeds the nonsocial one (because the first one is strictly dependent on the number of C-D interactions). The dash-dotted line in Fig. 7.1(a) depicts the evolution for $p_s = 0.1$ and $p_a = 0.05$. In this case, we find another victory of cooperation. As in the system containing only social punishers (solid line), the evolution starts with a soft fall of cooperators and then (after approximately 100 rounds) the population starts a constant progression to the maximum cooperation degree. The transient decline of cooperation is related to the defeat of those cooperators who were initially placed in a neighborhood with plenty of defectors. However, aggregates (clusters) of cooperators are able to survive and flourish in this notably changing ($v = 0.2$) environment, provided that the benefits of social punishment exceed those of nonsocial punishment. Indeed, the evolution of the nonsocial system [dotted line in Fig. 7.1(a)] is an example where these benefits are insufficient to lead the population to cooperation. Although here we focus on systems with mobile players, an analog to Fig. 7.1(a) for $v = 0$ is included in Sec. 7.3.

It could be sensible to think that the soft nonsocial case [dash-dotted line in Fig. 7.1(a)] models a system where social punishment dominates and, consequently, could be analogously represented by a system containing only social punishment. However, this case does not present the same features of the soft nonsocial system. Indeed, whereas in both cases the final state is a population composed by cooperators exclusively, the mean payoff per individual is notably lower in the nonsocial case. To see this, the mean payoff per individual in the final state can be predicted as

$$w = k\left(f_c R - p_a - 3p_a\right), \tag{7.5}$$

where f_c is the fraction of cooperators in the final stable state (in our system, either 0 or 1). The mean degree of the graph in all of our simulations is $k = \rho\pi = 4.08$. In Eq. (7.5), the mean number of neighbors that an individual has k is multiplied by the reward of an interaction R provided that the final state is all cooperators (i.e., $f_c = 1$) minus the mean costs of the punishments performed or received by the individual ($-p_a$ and $-3p_a$, respectively). Note that the social punishment probability p_s does not appear in Eq. (7.5) because C-D interactions are absent in the asymptotic state, in which all players are either C or D.

Figure 7.1(b) shows the evolution of the mean payoff per individual [for the same cases presented in Fig. 7.1(a)], and the symbols stand for the final-state values predicted by Eq. (7.5). The four curves tend asymptotically to the analytical value for the final stable state. In all the cases, the mean payoff shows a rapid decay during the first rounds of the game (every simulation ends or smooths this decay at a different moment before 100 rounds). Again, this transient effect corresponds to the defeat of those cooperators who have been initially placed in a neighborhood with many defectors. After this transient, the surviving cooperators are clustered and resist more efficiently the exploitation of the defector population. In the no-punishers and nonsocial cases (dashed and dotted lines, respectively), the environment is so extreme that even clusters of co-

the last 5 pools).

operators cannot endure the exploitation and the population continues its fall toward defection. When the final state is reached, the mean payoff is 0 in the no-punishers case, as there is no one that contributes any amount in the game. The situation is even worse in the nonsocial case, as nonsocial punishment makes the individuals accumulate negative payoffs. In contrast, the negative effect of social punishment on the mean payoff decreases as the number of C-D interactions decays. Hence the social punishers system (solid line) reaches the maximum payoff level available when the system is composed only of cooperators, namely, $w = k = 4.08$ (because $p_a = 0$ for social punishment, and we have chosen $R = 1$ as in, e.g., Ref. [44]). Therefore, social punishment is very effective for promoting cooperation. Finally, the soft nonsocial scenario allows the survival and maintenance of cooperation [as shown in Fig. 7.1(a)] but the average payoff is lower [compare the dash-dotted line with the solid line in Fig. 7.1(b)]. Below, we will present several figures that analyze the relevant parameters of the model. Although it will not be shown, the computational and the analytical results of Eq. (7.5) for the mean payoff agree as well as in Fig. 7.1(b) for all the simulations presented in this paper (when the corresponding steady state is reached).

Some of the major evolutionary characteristics of the system, detailed above, can be identified by looking a time series of snapshots for a single simulation. Figure 7.2 captures the snapshots at four times for a simulation with $v = 0.1$, $b = 1.1$, and the soft nonsocial environment used in Fig. 7.1 (i.e., $p_s = 0.1$ and $p_a = 0.05$). At $t = 0$ [Fig. 7.2(a)], both cooperator [green (light gray) dots] and defector [red (dark gray) dots] players are randomly placed in the system, with the same fraction ($< c >= 0.5$). In the left part of Fig. 7.2(a), we show a green (light gray) circle that represents the radius of interaction of a specific cooperator player who has been initially surrounded by several neighbors [during the first round, he will play the PD game with the eight coplayers who lie within the green (light gray) circle, with half of them being cooperators in this case]. In contrast, some other players may start the game completely isolated, as is the case of the defector in the center of the red (dark gray) circle [right in Fig. 7.2(a)]. Because of mobility, the number of connections for each player will change in time. Thus simulations with no mobility (i.e., $v = 0$) are essentially different from the ones where $v > 0$. Indeed, isolated players [like the one in the center of the red (dark gray) circle in Fig. 7.2(a)] will never play with other individuals in a simulation where $v = 0$, and consequently, the system will not reach a final all-C or all-D state (see Sec. 7.3 for further details of the case without mobility).

Figure 7.2(b) shows the state of the system after 100 iterations. At this time, the cooperation fraction has decreased to $< c > \simeq 0.35$ due to the defeat of those cooperators initially placed in hostile neighborhoods. As in Fig. 7.2(a), red (dark gray) dots correspond to defectors. In Fig. 7.2(b) we explicitly show those players who have punished socially at least once in the last round; hence cooperators have been divided in two types: green (light gray) dots show the players who have not punished socially in the last round, and blue stars indicate cooperators who punished at least one defector neighbor. We can see that the fraction of cooperators that punishes socially in a given round [blue stars in Fig. 7.2(b)] is relatively small. Nevertheless, we will see how the benefits provided by social punishment exceed the handicap due to nonsocial

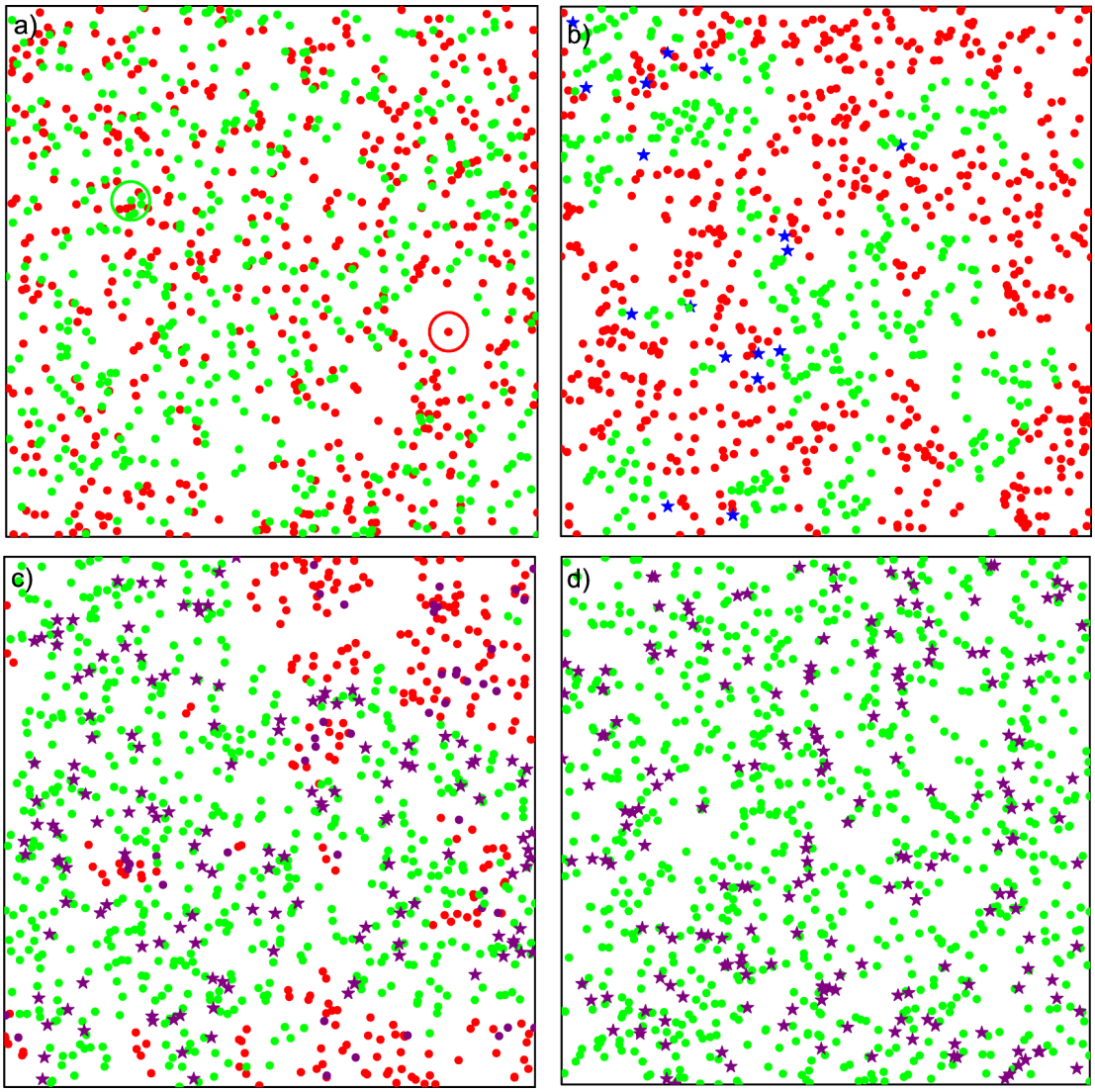

Figure 7.2: Spatiotemporal evolution of a soft nonsocial population where $p_s = 0.1$ and $p_a = 0.05$. This specific simulation has been performed for a population of $N = 1000$ individuals, $\rho = 1.30$, $b = 1.1$ and $v = 0.1$. Green (light gray) dots correspond to cooperator players, and red (dark gray) dots correspond to defectors. **(a)** Snapshot at $t = 0$. The population has been randomly distributed in the two-dimensional square. The two circles show the radius of interaction of a single cooperator [green (light gray) circle], and a single defector [red (dark gray) circle]. **(b)** Snapshot at $t = 100$. Blue stars correspond to cooperators that punished socially in the last round. **(c)** Snapshot at $t = 1000$. Purple stars (dots) correspond to cooperators (defectors) that punished nonsocially in the last round. **(d)** The stable all-C state is reached at $t = 5693$. Purple stars show the cooperators that still punish their partners when the whole population is cooperator.

punishment in this system, and the all-C state will be finally reached. In Fig. 7.2(c) we can see the state of the system at $t = 1000$. Here we explicitly identify the players who used nonsocial punishment in the last round: purple stars correspond to cooperators who punished at least one other cooperator, and purple (darkest gray) dots correspond to defectors who punished at least one coplayer. In this case, the fraction of cooperation is $< c > \simeq 0.7$, so clusters of cooperators have spread since $t = 100$ [compare to Fig. 7.2(b)]. Finally, Fig. 7.2(d) shows the final all-C state reached after 5693 iterations. In order to explicitly show that nonsocial punishment still takes place in the game, purple stars indicate those cooperators who still punish their cooperator partners. This has a direct effect on the mean payoff attained by players, as we have shown above [see the discussion of Fig. 7.1(a)].

7.3 The key role of mobility

In the model we have analyzed, a certain mobility rate of the players is present in most of the simulations. In the original model where punishment was not considered [44], an extended study concerning all the relevant parameters (including the mobility rate) of the corresponding model was presented. Roughly summarizing the conclusions by Meloni *et al.* [44], the authors noticed cooperation could flourish in their model when the parameters b and v were not too high. Moreover, they pointed out that the mobility led the system to only two stable states (i.e., all cooperators or all defectors). In contrast, when $v = 0$ the graph corresponds to a random geometric graph [148], so the stabilization of a population containing a mixture of the two strategies is expected.

The question of how punishment could affect the system when $v = 0$ arises. Thus in Fig. 7.3 we have rerun our simulations in Fig. 7.1(a) for a population that does not move ($v = 0$). In this case, clusters of cooperators manage to stabilize and survive in the system if no punishment is applied (the dashed line in Fig. 7.3 shows that the average cooperation in the system is above 20%). However, social punishment strongly supports cooperators in this immobile system, as shown by the solid line in Fig 7.3 (the cooperation fraction reaches 90% of the population in this case, where $p_s = 0.1$ and $p_a = 0$). Furthermore, the final outcome is much the same when the frequency of nonsocial punishment is increased up to $p_a = 0.05$ (the dash-dotted line depicts this soft nonsocial scenario, where the stable cooperation fraction is also high). Nevertheless, the stabilization of this latter case (dash-dotted line) comes later than in the social case (solid line) and remains at lower cooperation levels at any time. These results are no longer reached if we explore a nonsocial system where $p_s = p_a = 0.1$ (dotted line in Fig. 7.3) since in this case defection is practically extended to the whole population (the final cooperation fraction is above 3%).

If we compare the results of Fig. 7.1(a) ($v = 0.2$) with those presented in Fig. 7.3 ($v = 0$) we can draw similar conclusions regarding punishment. In both cases, social punishment helps cooperation to flourish. But this conclusion breaks down if sufficiently strong non-social punishment is present [in both Figs. 7.1(a) and 7.3, the soft nonsocial case with $p_a = 0.05$ leads to generalized cooperation, but the nonsocial

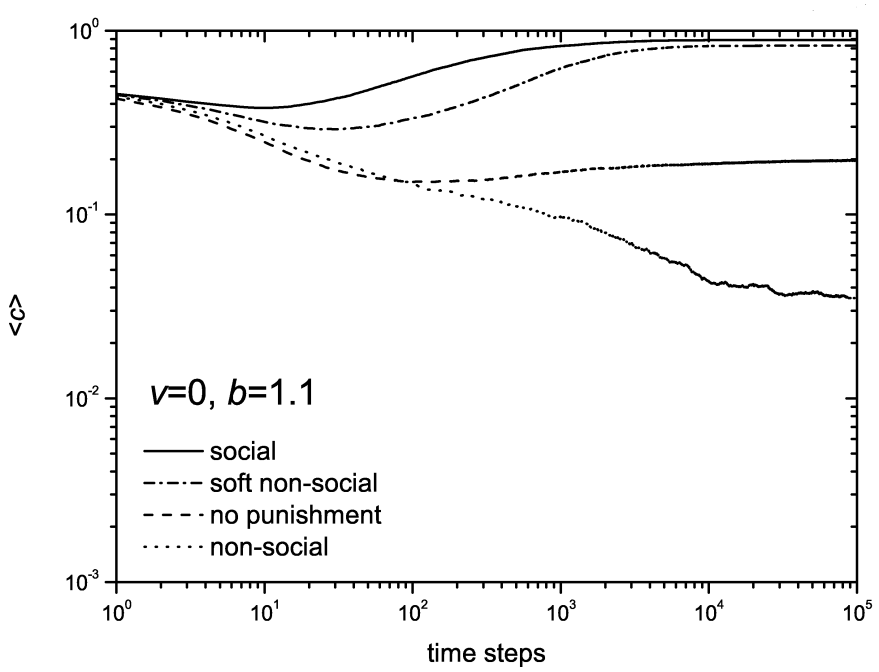

Figure 7.3: Average level of cooperation $< c >$ as a function of time for a population without mobility ($v = 0$) for $N = 1000$ individuals, $\rho = 1.30$, and $b = 1.1$. The solid line depicts the evolution for a population where social punishment is allowed (with $p_s = 0.1$). The dash-dotted line shows the evolution of the same population in a soft nonsocial environment, where $p_s = 0.1$ and $p_a = 0.05$. The dashed line stands for the case where punishment is not allowed at all. Finally, the dotted line shows a nonsocial system where $p_s = 0.1$ and $p_a = 0.1$. Results are averaged over 100 simulations.

case with $p_a = 0.1$ does not]. Furthermore, the comparison of Figs. 7.1(a) and 7.3 suggests that the effect of mobility can be very important in the case of nonsocial punishment. In the case of nonmobile and nonpunishing populations (dashed line in Fig. 7.3), the final stable state permits a coexistence of cooperators and defectors. The final fraction of cooperators depends on the value of b. While cooperators are able to survive in clusters for moderate values of b (as is the case represented by the dashed line in Fig. 7.3), only a few isolated cooperators remain in an almost all-defector population for high values of b (not shown). In contrast, in the case of mobile populations, the value of v influences the final outcome for a given value of b. Here we have shown how clusters of cooperators that survive in nonmobile populations (dashed line in Fig. 7.3) are not able to resist in a population with $v = 0.2$ [dashed line in Fig. 7.1(a)]. In this case the final population is composed exclusively by defectors. However, the system would have turned into a full cooperation state if we had chosen a slower velocity of $v = 0.01$ for the same value of $b = 1.1$ (see, for example, Fig. 1 in Ref. [44]).

In this paper, a huge number of configurations of the parameters v, b, p_s, and p_a has been tested. Generally, we have focused our work on mobile environments with $v > 0$.

However, the case $v = 0$ has been simulated and analyzed for all of the environments presented above (even if not shown in the figures). In every case, the conclusions from the simulations with $v = 0$ were very close to the conclusions from those with low speeds like $v = 0.01$ [and sometimes much higher values like $v = 0.2$, such as those presented above by comparing Figs. 7.1(a) and 7.3]. In Figs. 7.4, 7.5, and 7.6 we have taken care that the minimum speed presented does not sensibly differ from the results obtained for $v = 0$.

7.4 General results

This section is devoted to exploring the limits of punishment-enhanced cooperation. Hence, we will extend the results in order to analyze all of the relevant parameters of the model.

In addition to N and ρ (see Sec. 7.2.2), the model in Ref. [44] has two relevant parameters, namely, the mobility rate v and the temptation to defect b. Here we have extended that model to include punishment, so we will analyze the role of the parameters p_s and p_a in addition to v and b.

Figure 7.4 shows a phase diagram where the effects of the mobility v and the temptation to defect b are explored (for the same sets of values for p_s and p_a as in Fig. 7.1). The dashed line corresponds to the case where punishment is not present (i.e., $p_s = p_a = 0$). The region where simulations end up with a population of all-cooperators falls below the dashed line (whereas an all-D state is found above the dashed line). This limit agrees well with the results presented in Ref. [44]. The solid line in Fig. 7.4 indicates the frontier between cooperation and defection when social punishment is introduced with probability $p_s = 0.1$. Comparing the dashed line with the solid line, it follows that social punishment clearly expands the parameter region where cooperation is reached. When no punishment is allowed in the game (dashed line), the maximum temptation to defect that cooperation can endure is slightly under the value $b = 1.2$. In contrast, when social punishment is introduced (solid line), the transition from cooperation to defection occurs at a maximum b value of 1.45. These values of b remain approximately independent of the mobility rate when $v < 0.05$ (see Fig. 7.4). This indicates that the clustering of cooperators is easily attainable below $v \simeq 0.05$. Nevertheless, Fig. 7.4 shows that at higher speeds ($v > 0.05$) the parameter region where cooperation is available becomes smaller: both solid and dashed lines present a gradual decay (the higher the value of v is, the lower the temptation to defect b that cooperation can resist is). This is because agglomerations of cooperators are hard to maintain in highly mobile systems. Without punishment (dashed line), the system cannot achieve the full cooperation regime when $v \gtrsim 0.2$ (independently of the value of b), whereas in the social environment (solid line) full cooperation is possible up to $v \approx 0.7$.

Figure 7.4 also shows the transition from full cooperation to full defection for a soft nonsocial environment (dash-dotted line, i.e., $p_a = 0.05$ in addition to $p_s = 0.1$). For this parametrization, the cooperative region covers a higher area of v and b than in the case without punishment (dashed line) but smaller than in the social environment (solid

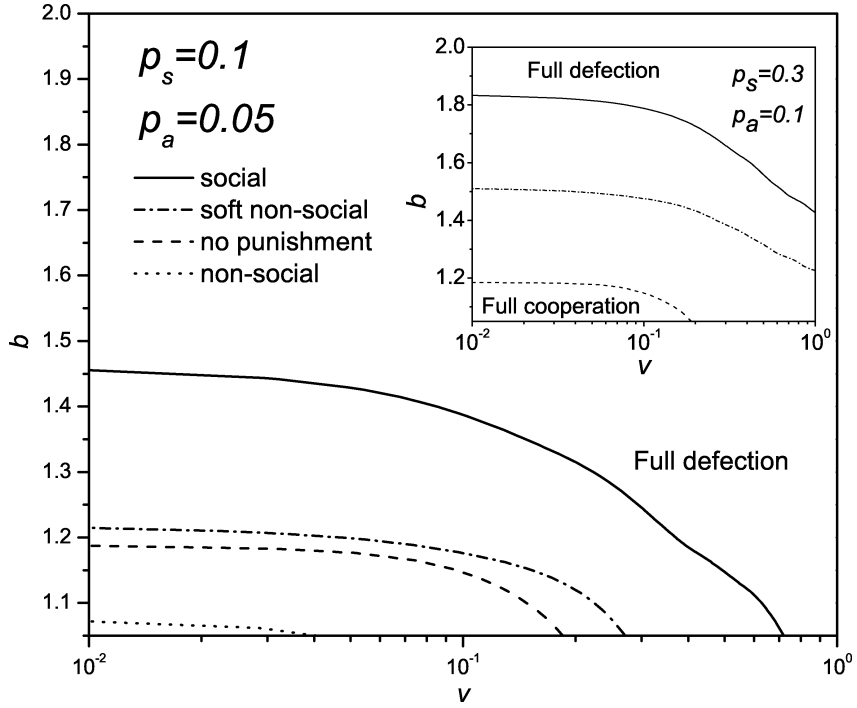

Figure 7.4: Phase diagrams for different versions of punishment as a function of v and b. Results have been obtained for a population of $N = 1000$ individuals, with $\rho = 1.30$. The solid line depicts the phase transition for a population where social punishment is allowed (with $p_s = 0.1$). The dash-dotted line corresponds to the case of a soft nonsocial environment, where $p_s = 0.1$ and $p_a = 0.05$. The dashed line stands for the phase transition where punishment is not allowed at all. Finally, the dotted line corresponds to a nonsocial system where $p_s = 0.1$ and $p_a = 0.1$. In the inset, the lines depict the transition phases for the following cases: the solid line corresponds to $p_s = 0.3$, the dash-dotted line corresponds to $p_s = 0.3$ and $p_a = 0.1$, and the dashed line corresponds to the case $p_s = p_a = 0$. No full cooperation phase was found for the non-social case where $p_s = p_a = 0.3$.

line). The last curve shown in Fig. 7.4 corresponds to a nonsocial environment where $p_s = p_a = 0.1$ (dotted line). In this case, nonsocial punishment plays an important role against cooperators: the majority of the parameter range explored is dominated by defection, whereas cooperation only manages to survive at very low values of v and b ($v < 0.03$ and $b = 1.05$).

The curves in Fig. 7.4 clearly show that the system is sensitive to the addition of both social and nonsocial punishment. Thus we now analyze what values of p_s and p_a drive the population to cooperation. Before an in-depth analysis, in the inset of Fig. 7.4 we consider the case in which social punishment is as frequent as $p_s = 0.3$ and nonsocial punishment is not allowed (full line). Then cooperation wins for most values of b if the mobility is not high ($v < 0.1$). When increasing the mobility, the cooperative state displays its usual decay to more modest values of b. However, under a critical

value of the temptation to defect (in this specific case for $b < 1.45$) cooperation prevails at any speed in the range $v \in [0.1]$, indicating that the positive effects of such extended social punishment ($p_s = 0.3$) sustain cooperation even when the system is close to a well-mixed population. This behavior remains qualitatively the same if a moderate degree of nonsocial punishment is introduced in the system (dash-dotted line in the inset of Fig. 7.4, i.e., $p_a = 0.1$ in addition to $p_s = 0.3$). In this latter situation the range of b cooperation can endure is always below the case where only social punishment is present (solid line in Fig. 7.4, inset). For comparison, we have also included the system without punishment (dashed line in Fig 7.4, inset). Finally, the nonsocial environment $p_s = p_a = 0.3$ has also been explored, but no full cooperation phase has been found in the parameter ranges explored. This indicates that increasing the value of p_a leads to a harsher effect against cooperation (compare to the case $p_s = p_a = 0.1$ in Fig. 7.4 where a small cooperative region is found). Summarizing, we have shown in Fig. 7.4 that social punishment enhances notably the v-b region available for the cooperative phase. Furthermore, social punishment produce benefits for cooperation even if some degree of nonsocial punishment is considered. However, when nonsocial punishment becomes substantially frequent, it leads to the triumph of freeloaders.

In order to further analyze the role of p_s and p_a, Fig. 7.5 shows their effect on the transition between cooperative and defective regimes (for $b = 1.5$). The solid line in Fig. 7.5 shows computational results for a mobility rate $v = 0.01$. Note that cooperation is not possible below a critical social punishment probability ($p_s \lesssim 0.15$). For $p_s > 0.15$, the all-C stable state is reached provided that p_a takes moderate values (full cooperation is reached if $p_s > p_a$). It follows that the more extended nonsocial punishment is in the system, the more frequent the social punishment has to be in order to sustain cooperation. There is an interesting region ($0.15 < p_s < 0.4$) where social punishment seems to resist better the presence of nonsocial punishment. The dashed line depicts the case $v = 0.2$, where in response to the higher mobility, the system is more sensible to nonsocial punishment in the region $0.15 < p_s < 0.4$. The dotted line corresponds to a substantially higher mobility, $v = 0.6$. Now the system needs more frequent social punishment to make cooperation successful. Indeed, whereas for $v < 0.2$ cooperation is found at $p_s \gtrsim 0.15$ (solid and dashed lines), for $v = 0.6$ no cooperation phase exists below $p_s = 0.25$ (dotted line). Furthermore, there is again a region where social punishment is more efficient against nonsocial punishment (dotted line, $0.25 < p_s < 0.5$). Finally, the dash-dotted line in Fig. 7.5 displays a highly mobile system ($v = 0.8$), which is closer to a well-mixed population than the case $v = 0.6$ (dotted line). Under very high mobility, the enhanced efficiency of social punishment in the region $0.25 < p_s < 0.5$ disappears, and cooperation is not sustainable below more frequent social punishment ($p_s = 0.35$).

Although the solid line in Fig 7.5 depicts the phase transition for the case $v = 0.01$, we have also performed simulations for several values in the range $v \in [0, 0.01]$, and the corresponding phase transitions are independent of v in this range. On the other hand, the outcome of simulations performed for $v > 0.8$ agree well with the case $v = 0.8$.

Whereas in Fig. 7.5 we have shown the dependence of the phase transitions on the parameters p_s and p_a for different mobilities and a fixed value of $b = 1.5$, in Fig.

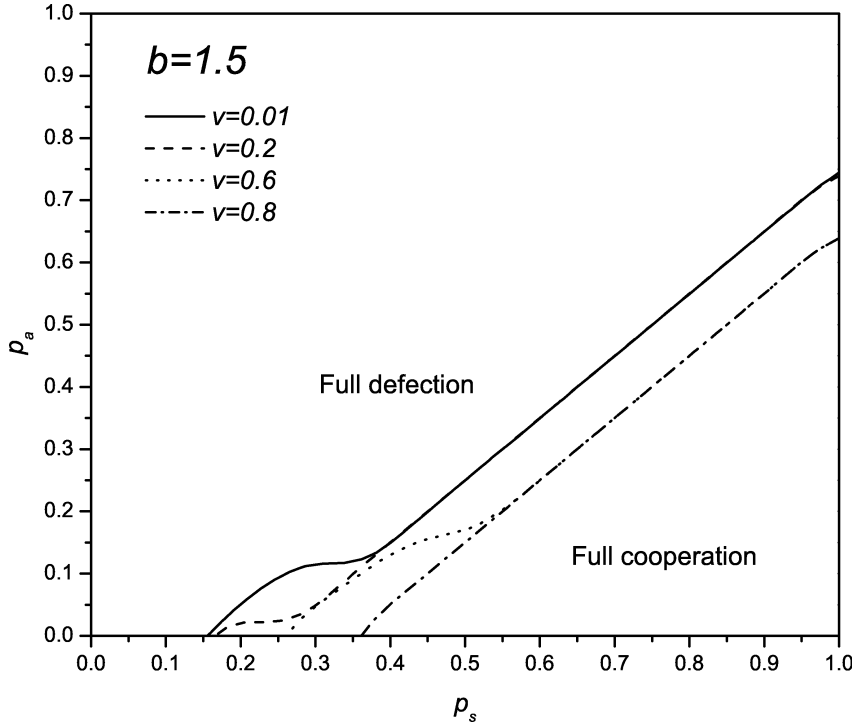

Figure 7.5: Phase diagrams for different mobility rates as a function of p_s and p_a in the specific case with $b = 1.5$. Results have been obtained for a population of $N = 1000$ individuals, with $\rho = 1.30$. The solid line depicts the phase transition when the mobility of the agents is $v = 0.01$, the dashed line stands for the case $v = 0.2$, the dotted line is for $v = 0.6$, and the dash-dotted line represents the case of $v = 0.8$.

7.6 we vary the temptation to defect b for a fixed value of v ($v = 0.1$). The dashed line in Fig. 7.6 ($b = 1.5$, as in Fig. 7.5) shows similar behavior to the solid line in Fig. 7.5 ($v = 0.01$), including a region where social punishment is especially effective ($0.15 < p_s < 0.30$). On the other hand, the solid line in Fig. 7.6 represents a much more social environment since the temptation to defect is now $b = 1.1$ (cooperation is available even in the absence of punishment, $p_s = p_a = 0$). The dotted line in Fig. 7.6 corresponds to a high temptation to defect ($b = 2$). In this case, the region available for cooperation is limited to high values of social punishment (cooperation is not sustainable for $p_s < 0.45$), similar to what happens under high mobility (dash-dotted line in Fig. 7.5).

In Figs. 7.5 and 7.6, we have shown that for very high values of v or b, defection is the dominant strategy, and cooperation is only possible for extreme social punishment frequencies (in contrast, for low values of v and b cooperation is more sustainable). This extends the results by Meloni *et al.* [44] to systems under social and nonsocial punishment, as observed in many human populations [45]. Moreover, when v and b take moderate values, low doses of social punishment are especially effective in counteracting the effects of nonsocial punishment. This is an important result because it means that

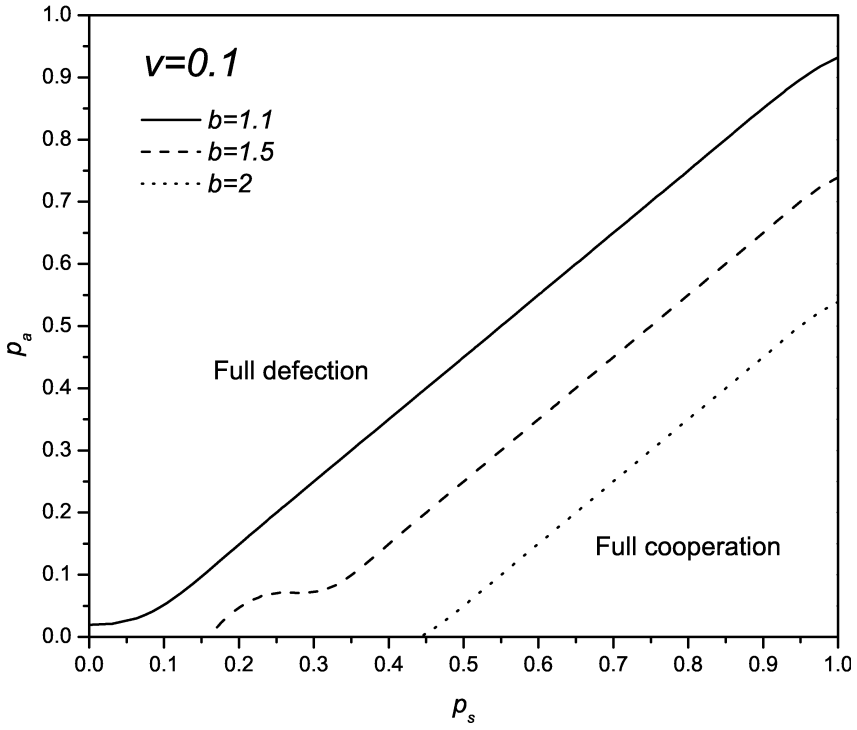

Figure 7.6: Phase diagrams for several temptation to defect values as a function of p_s and p_a, and $v = 0.1$. Results have been obtained for a population of $N = 1000$ individuals, with $\rho = 1.30$. The solid line depicts the phase transition when the temptation to defect is $b = 1.1$, the dashed line stands for the case $b = 1.5$, and the dotted line presents the case $b = 2.0$.

players do not need to be rude punishers in order to promote cooperation; thus in the fight against defection, lower mean expenditures on altruistic punishment are necessary.

7.5 Conclusions

We have built a model that introduces altruistic punishment options in a population with mobile players of the PD game. Players move continuously in a two-dimensional world, a case of practical relevance with potential applications, such as the design of cooperation-based protocols for communication [132] and the modelization of transitions in human prehistory [1]. In our model, punishment is not a strategy but an action that players may perform against their partners with a certain probability after each round of the game. We have found that punishing after only 10% of the cooperator-defector interactions is enough to lead the system to a world of cooperation, in some environments where otherwise defection would take over the population. Furthermore, this conclusion holds even if some degree of nonsocial punishment (an action that is commonly performed by human players) is present in the system. Our analytical predic-

tions for the mean payoff of the final state agree with simulations. We have also found that, although soft nonsocial punishment can lead to a cooperative state, it yields lower payoffs than social punishment.

We have extensively analyzed the role of the relevant model parameters: the mobility of the players v, the temptation to defect b, the social punishment probability p_s, and the nonsocial one p_a. The phase diagrams have shown that social punishment increases the values of v and b where cooperation is available. We have found that this result resists some degree of nonsocial punishment. Moreover, the full-cooperation region is sensible to the increment of p_a. Finally, we have shown that the benefits of social punishment are limited, and defection asymptotically prevails in harsh environments for cooperation (represented here by high mobilities, high temptation to defect values, and extended practices of nonsocial punishment).

The model in this paper takes into account simple mobility rules and strategies. Additional degrees of complexity could be added in order to closely study human abilities to face defector (or cooperator) neighbors. For example, success-driven migration could be studied (this has been recently proposed in square lattices [124] but not yet for continuous motion).

7.6 Acknowledgements

This work was funded by the Ministry of Science (Grants No. SimulPast-Consolider-CSD-2010-00034 and No. FIS-2009-13050) and the Generalitat de Catalunya (Grant No. 2009-SGR-374). D.C.[1] was supported by the Ministry of Education under the FPU program.

[1]In the published version of this work there is a typographical error in this sentence; the right abbreviation is D.R.A, rather than D.C.

Chapter 8

Results and discussion

The main work in this thesis has been presented as the collection of papers in chapters 4-7. This chapter provides a unified discussion on the main conclusions of the papers. Furthermore, some assumptions on the models are reviewed in order to present interesting alternatives, and brief guidelines for potential future work are mentioned. Although the following discussion may deliberate back and forth between the different models and their methods, for clarity the sections below indicate which model is being principally considered.

8.1 2D structured populations model

The overlapping generations model in chapter 4 specially focuses on tree population fronts. Nevertheless, the model establishes the physical and mathematical bases for the 2D analysis of structured populations dynamics in general. Noteworthy, it is simple to relax or modify the specific assumptions for the tree population (e.g., dispersal of seeds immediately follows reproduction), in order to describe any different biological population. Generally, such new assumptions are not expected to alter the two main methods to obtain analytical results, namely: *i)* the creation of the reaction-dispersal matrix $\overrightarrow{\overrightarrow{H}}$ (which contains the Bessel function $I_0(\lambda\Delta)$ if isotropic 2D spread is considered), and *ii)* the derivation of the front speed from the largest real eigenvalue of $\overrightarrow{\overrightarrow{H}}$.

In the model in chapter 4, every year during the lifetime of the individual determines a specific stage. Typically, structured populations have been described by stages which represent longer periods or phases [19, 107]. For example, a very simple, three-stage model could assume that yellow poplar individuals are classified into young, adult and old trees. This would lead to the following demographic matrix:

$$\overrightarrow{\overrightarrow{A}} = \begin{pmatrix} 1-\alpha & R_0 & 0 \\ \alpha & 1-\beta & 0 \\ 0 & \beta & 1-\gamma \end{pmatrix}, \tag{8.1}$$

where α is the fraction of young individuals that survive to become adults, β the corresponding fraction for the transition from the adult stage to the old stage, and γ

the mortality of old individuals. The population structure defined by the matrix (8.1) assumes that only adult individuals produce seeds (R_0 is the net reproductive rate per tree and year, as in chapter 4). Analytically, a model involving a few number of phases (such as the above three stages example) is far less complex to solve than the age-structured model in chapter 4. However, the year-associated stages in the overlapping generations model in this thesis allow for yearly age dependencies of R_0 and the dispersal kernel [see, e.g., Eq. (4.7)]. Nevertheless, the use of high order matrices is required, and this notably increases the complexity of the evolution equations. Fortunately this is not an important handicap, since the computation times to obtain the front speed are not excessive[1].

Chapter 4 has shown analytical results from both CSRW and DSRW, as well as the front speed from numerical integrations. When dealing with integrodifference equations [such as Eqs. (4.1) and (4.25)], analytical expressions allow the analysis of multiple features of the system (e.g., the sensitivity of the front speed to the parameter R_0). Such analyses become usually simpler to perform by means of analytical approximations than developing numerical simulations. Moreover, integrodifference equations can be easily adapted to examine many different hypotheses (e.g., continuous space versus discrete space). However, analytical solutions are subject to several assumptions (see Sec. 3.2.1 and 3.2.2) on the population density at the front edge, such as the marginal stability assumption. On the other hand, numerical simulations are not based on such assumptions and provide very useful checks of the front speed. Nevertheless, the main drawback of numerical integrations is that they necessarily consider discrete spaces. This can affect the results because of relevant approximations on the dispersal kernel and a compulsory feedback between the resolution of the spatial grid and the computation time. Concerning the structured model in chapter 4, the front speeds from numerical simulations corroborate the approximations used in the analytical approach, since perfect agreement between DSRW and numerical integration results is observed. In contrast, the differences (of about 5%) between the front speed from CSRW and numerical simulations (or DSRW) show that the discretization of the space can significantly influence the results.

When considering parameter values for the yellow poplar species, the overlapping generation model exhibits two important features. On the one hand, the spread rates from the overlapping model are substantially higher than those from the nonoverlapping theory (except in the limit $R_0 \to \infty$, see Sec. 8.3). Admittedly, both the nonoverlapping and the overlapping models are able to predict spread rates which could explain Reid's paradox, provided that long-distance dispersals are considered for the yellow poplar. On the other hand, taking into account multiple reproduction events allows to analyze some extreme situations in which the nonoverlapping model fails. For example, the nonoverlapping model predicts extinction if $R_0 < 1$, whereas considering the structure of the population in the same situation can reveal the survival of the species (see in Fig. 4.2). This suggests the structured model is specially suitable for further analysis and applications. For example, it would be interesting to introduce stochasticity in the

[1] See footnote ** in chapter 4.

parameter values, representing periods in which the population is affected by plague, extreme meteorological conditions, etc. Such studies are not suitable for a nonstructured model in which the population cannot resist transitory harsh conditions (e.g., $R_0 \to 0$).

In agreement with analogous conclusions for nonstructured populations in Ref. [15], considering a 2D structured populations model leads to lower spread rates than the corresponding 1D analysis (Table 4.2 in chapter 4 shows differences above 14% between 1D and 2D results). Because the majority of biological invasions take place in two dimensions, the 2D model in chapter 4 provides a more reasonable approach than previous 1D structured populations studies [19].

8.2 Reaction-diffusion equations for multiple species systems: focal infections

Chapter 5 in this thesis has focused on the equations for focal infection systems, in which viruses and their host cells interact.

In this thesis the reaction-diffusion equations in Ref. [10] have been revised. In agreement with recent considerations on the partial derivatives of the HRD equation (1.2) [43], the effect of the virus growth function has been properly computed. The front speed from the new equations has been compared with observed infection speeds of both VSV and T7 viruses.

Analytical results have been checked by comparing to infection speeds from numerical simulations. Mainly, the front speed from analytical solutions to the differential equations for virus infections presents the same advantages and drawbacks as analytical methods for integrodifference equations (see discussion in section 8.1). Noteworthy, for the numerical integrations of the virus infections systems, very short time steps and high definition spatial grids have been used (see section 5.4). Consequently, exact analytical results (which consider continuous space) closely agree with the front speed from numerical integrations (that consider discrete space), as shown in Figs. 5.2 and 5.3, as well as Fig. 6.1. Moreover, numerical integrations allow to monitor the evolution of the concentration profiles of the different species in the system (see Fig. 5.1). This is an additional advantage of numerical simulations with respect to analytical solutions for the front speed.

Chapter 5 has clearly shown the critical role of the lag time on VSV infections. Realistic lag time values have lead to predicted front speeds which agree with those observed in VSV focal infection experiments (see Fig. 5.2). Instead, a clear mismatch with the experimental front speeds is obtained when considering $\tau = 0$ (which corresponds to non-delayed models, such as that in Ref. [23]).

The model in chapter 5 aims to avoid the use of unnecessary adjusted parameters. Noticeably, the predicted front speed has been shown to be independent of the adsorption rate k_1 for several orders of magnitude (see Fig. 5.3). Moreover, dimensionless equations have been used to derive both analytical and numerical solutions, and the diffusivity D affects only relative speeds because it is only relevant when switching to the dimensional expression of the front speed from the relation $c = \overline{c}\sqrt{k_2 D}$. Admit-

tedly, the relative independence of the dimensionless front speed on both D and k_1 strongly supports the usefulness of the results in chapter 5, since they are the only two parameters of the model for which an experimental measure has not been found.

Due to the complex equations driving the dynamics of focal infections [see Eqs. (5.11)-(5.13)], the exact infection front speed can only be computed numerically. Because of this, simpler approximate expressions are very useful to better understand the results of the model. Assuming a high virus yield and a low value of κ [2], the following approximate front speed is obtained:

$$\overline{c} = \sqrt{\frac{1}{\beta}} = \sqrt{\frac{2}{\overline{\tau}}}. \tag{8.2}$$

The above approximate solution presents a remarkably good agreement with exact results (as shown in Figs. 5.2 and 5.3). Moreover, it indicates that the dimensionless lag time $\overline{\tau}$ is the only relevant parameter to compute the dimensionless front speed of VSV infecting BHK cells. For the derivation of Eq. (8.2), $\beta >> 1$ was assumed, which is equivalent to assume $\tau >> 0.81$h for VSV in chapter 5. Not only this condition is satisfied by the experimental observations ($5 < \tau < 10$h for VSV infecting BHK cells, see Fig. 3.2), but also the approximate speed is very close to the exact results for $\tau > 0.5$h (see Fig. 5.2).

The model for virus infections has specially focused on the front speed. Future works could target further characteristics which are observable in focal infection experiments. For example, additional terms in the reaction-diffusion equations could account for an immune response of the cells, or stochastic anisotropic dispersion (see the experimental images in Ref. [58]). In Ref. [23] the authors attempted to model such observable phenomena, but their model completely neglects the lag time τ and makes use of a large number of adjusted parameters.

To summarize, the model in chapter 5 shows the lag time τ plays a critical role on VSV infections. Instead, other parameters (specially k_1) become irrelevant for the computation of the spread rate, if the lag time τ of the virus is large enough. When this conclusions were reached, the question arose if the approximate speed (8.2) could be useful to describe other focal infections. Rather surprisingly, a deep analysis of several time-delayed reaction-diffusion models revealed that the approximate speed (8.2) is also appropriate for a variety of biological fronts (see the next section).

8.3 Approximate front speed for time-delayed spreading populations

The lag time has been shown to be of utmost importance for several virus species. When applying the approximate Eq. (8.2) to the spread of T7 mutants infecting bacteria (see chapter 6, specially Fig. 6.1), the approximate results are as close to the exact theory as in the case of VSV infections (see also section 8.2). Concerning the assumptions on

[2] In chapter 4 we defined this parameter as $\kappa \equiv k_1 C_0/k_2$.

the parameter values under which Eq. (8.2) was derived (see section 8.2), remarkably, these assumptions are not very limiting for virus infection systems. For example, all of the viruses analyzed in this thesis display values of the yield $Y > 30$, which is enough to obtain useful approximate front speeds that perfectly agree both with exact theoretical solutions and with experimentally measured spread rates. This suggests the approximate Eq. (8.2) could describe a general trend in virus focal infections. For the case of human invasions, instead, the high reproductive rate assumption is appreciably more restrictive than for virus invasions (see below).

For single-species systems driven by the HRD equation (1.2), the approximate speed $c = \sqrt{2D/T}$ is obtained when considering the limit of high reproduction rates. In chapter 6 the Neolithic transition front has been analyzed in order to check the usefulness of the approximate speed. Significant differences (above 15%) are observed between the approximate speed and the exact solution of the HRD equation, if a realistic value for the Neolithic human reproduction rate (namely, $a = 2.8 \cdot 10^{-2}$ yr^{-1}) is considered (see Fig 6.2). Nevertheless, the approximate speed reasonably agrees with observed spread rates of the Neolithic in Europe, indicating the speed $c = \sqrt{2D/T}$ is a useful estimation of the speed of the Neolithic front.

The overlapping generations model for tree populations presents the mathematically most complex equations in this thesis. The high order of the matrices involved in the reaction-diffusion equations of the model makes it impractical to derive an exact explicit equation for the front speed. Fortunately, if high (but realistic) reproduction rates are considered, both the nonoverlapping generations and the overlapping generations models tend to the same asymptotic front speed (see section 8.1). Thus, the nonoverlapping generations assumption has been considered when deriving the approximate front speed for postglacial recolonizations (details on this derivation appear in chapter 6). As with focal infections and the Neolithic invasion, the approximate speed $c = \sqrt{2D/T}$ has also been shown to be useful to explain observed spread rates of postglacial recolonizations. Its results are closer to the exact front speed from the structured populations model when high (but realistic) reproduction rates are considered (see Fig 6.3).

The generational reproduction rate R_{0g} is a very relevant parameter in order to obtain front speeds from the nonoverlapping generations theory that closely agree with the predictions of the overlapping generations model. In chapter 6, the approximation $R_{0g} = TR_0$ has been used, as it provides a more reasonable assumption than those in previous attempts [15, 108]. However, other approaches to R_{0g} could be studied in order to obtain more realistic results from the approximate theory. In Fig. 8.1 the front speed from the nonoverlapping generations equation is analyzed for several values of the generational reproduction rate, which in this case is assumed to be an integer multiple of R_0. For comparison, the dashed line and the dotted curve in Fig. 8.1 show the nonoverlapping generations results for the cases $R_{0g} = R_0$ (as in Ref. [15]) and $R_{0g} = TR_0$ (chapter 6), respectively. It can be observed the front speed from the nonoverlapping theory better reproduces the behavior of the overlapping theory if $R_{0g} = TR_0$ is considered instead of $R_{0g} = R_0$ (see specially the rapid decay of the dashed line for $R_0 < 30$). However, the overlapping results seem to correspond to an intermediate case between the nonoverlapping speeds with $R_{0g} = TR_0$ and $R_{0g} = R_0$.

This seems reasonable intuitively, because only seed produced during the first few years (after the first tree produces seeds at a previously empty location) could be reasonably expected to affect the colonization speed. Indeed, the nonoverlapping generations front speed is specially close to the overlapping generations speed for $R_{0g} = 4R_0$ (full triangles in Fig. 8.1). Fig. 8.1 reveals that the evaluation of the generational reproduction rate (which was introduced in chapter 6) still remains an open question. Forthcoming studies could focus on convenient ways to estimate the generational reproduction rate of tree species, and then theoretical analyses would possibly be able to reveal why $R_{0g} = 4R_0$ provides such close approach between the two models presented in Fig. 8.1.

The above conclusions on the application of the approximate speed to three rather different biological invasions (virus infections, the Neolithic transition and postglacial tree recolonizations) suggest that the expression $c = \sqrt{2D/T}$ could describe a general trend in front propagation. Future work could report further applications of the approximate front speed $c = \sqrt{2D/T}$. For example, the approximate front speed could be compared with results from cohabitation equations for human invasions (such as the Neolithic transition) [30]. Moreover, it would be interesting to check the validity of the approximate speed in other biophysical systems (such as cancer tumors [66]) and in nonbiological systems presenting delay times (such as crystallization fronts [109] or combustion fronts [110]).

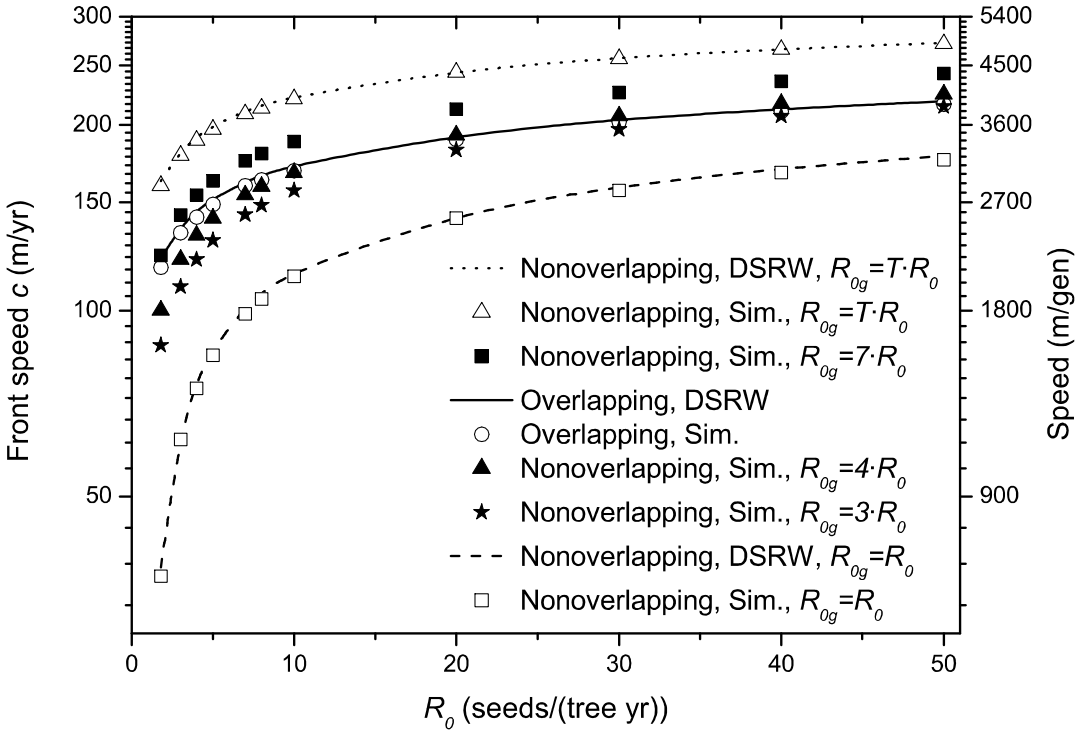

Figure 8.1: Front speed in two dimensions versus net reproductive rate per year. The solid line (empty circles) stand for the exact analytical solution (numerical simulations) from the overlapping generations model. The dotted line (empty triangles) and the dashed line (empty squares) correspond to the exact analytical solution (numerical simulations results) from the nonoverlapping model when $R_{0g} = TR_0$ and $R_{0g} = R_0$, respectively. Full squares, full triangles and full stars show the front speed from the nonoverlapping model for the cases $R_{0g} = 7R_0$, $R_{0g} = 4R_0$ and $R_{0g} = 3R_0$, respectively. The same parameter values used in chapter 5 for the yellow poplar species have been used, i.e., $\Delta = 6000$ m, $p_e = 0.99798$, $T = 18$ yr, and a lifespan of 130 yr (which is only applied in the overlapping generations model).

8.4 Cooperation and probabilistic punishment

The paper in chapter 7 has gone beyond spatial population dynamics (chapters 4-6) by analyzing evolutionary dynamics in a spatial context. To this end, chapter 7 has been devoted to the evolution of cooperation when agents move continuously and punishment upon coplayers can be applied. The type of punishment rules which have been explored is specially innovative: instead of conceiving punishment as an additional strategy in the game, players engage themselves in punishment actions with a certain probability. Thus, facing twice the very same conditions after a Prisoner's Dilemma interaction, a cooperator (or a defector) can behave differently when asked to punish his/her coplayer. This simple probabilistic punishment not only represents the occasional human disposition to punish opponents, but it also prevents individuals to bear the unreasonable cost of punishing every partner they confront. To the authors knowledge, such probabilistic form of punishment has not previously been studied. Furthermore, punishment has been seldom studied in environments where players move continuously.

Both time series and snapshots (Figs. 7.1 and 7.2, respectively) of several representative punishment scenarios have shown the cooperation enhancement effect of social punishment. Low doses (such as a 10% probability) of social punishment are enough to lead the population to the full cooperation state, in some environments where otherwise defectors would win. It has also been shown that these benefits to cooperators can resist moderate doses (e.g., $p_a = 0.05$) of nonsocial punishment, though such nonsocial practices necessarily involve a certain decay of the average payoff per player.

In order to reach robust conclusions on the effects of mobility, nonmobile scenarios have been also analyzed (see specially Fig. 7.3). In general, the outcome of a nonmobile system ($v = 0$) is roughly the same than that of analogous societies undergoing low mobilities (e.g., $v = 0.01$). Nevertheless, in the case $v = 0$ neither the full cooperation nor the full defection state can be reached because of agents that are unable to update their strategy (because they were randomly isolated at the start of the simulation).

In the absence of punishment, low mobilities (v) promote cooperation, but the full cooperation state can only be reached for moderate values of the temptation to defect (b) (these conclusions are in agreement with the previous work by Meloni et al. [44], who did not include any kind of punishment). In general, the practice of social punishment results in higher v and b values that cooperation can resist, whereas the extended practice of nonsocial punishment has the opposite effect (Fig 7.4). Remarkably, for moderate values of v, b and p_a (the three parameters which promote defection), the phase diagrams show that social punishment is specially efficient in counteracting nonsocial punishment (Figs. 7.5 and 7.6).

The model in chapter 7 on the spread of cooperation relies on some simple assumptions on both mobility and punishment. Future work could be addressed to study further player abilities such as success-driven migration, the effect of network topology, etc. Admittedly, punishment has been typically analyzed within the Public Goods (PG) game. Forthcoming versions of the PG game could report further conclusions on the practice of probabilistic punishment. Moreover, it could be interesting to explore similar situations considering positive incentives, thus assigning to agents a probability

of offering rewards (rather than punishment) to their coplayers.

Chapter 9

Conclusions

This thesis has studied both population and evolutionary dynamics of several spatial systems. Reaction-diffusion equations have been used to model biological fronts, and the evolution of cooperation has been studied in mobile populations where players can punish.

Concerning tree population fronts, the fact that generations of different individuals overlap has been shown to remarkably increase the invasion speed (specially, when reproduction rates are not high). Further, taking into account overlapping generations can lead to predict survival instead of extinction in some cases. This result has been attained from the structured populations model in chapter 4. The matrix equations in the model are able to represent the structure of the population in general, not only that of tree populations. Hence, the model is useful to analyze other two-dimensional invasions. The models in chapter 4 are consistent with the observed speeds of tree recolonizations after the last glaciation.

In chapter 5, reaction-diffusion equations have been used to analyze the evolution of several-species systems. We have considered the case of Vesicular Stomatitis Virus infections. The delay time (i.e., the time interval during which the virus is inside the host cell) is critically important in VSV infections. Moreover, the delay time and the diffusivity are the only two relevant parameters in order to compute the front speed, as it has been indicated by approximate results that closely agree with the exact theory, numerical simulations and experimental data.

The approximate front speed solution $c = (2D/T)^{1/2}$ has been derived from several time-delayed reaction-diffusion models in chapter 6. This approximate expression provides more accurate results when the populations display high reproduction rates. Remarkably, the approximate speed provides results which explain the observed spread rates of several virus infections, the Neolithic transition in Europe, and postglacial tree recolonizations. Thus, it could be a general trend in front propagation.

In chapter 7 the evolutionary dynamics of cooperation has been studied. Two specific mechanisms affecting the population have been considered: continuous motion and punishment. Simulations show that cooperation is favoured by low mobilities and social punishment. Instead, free-riders succeed in the following scenarios: *i)* the temptation to defect is high, *ii)* highly mobile systems, *iii)* extended use of nonsocial punishment.

Bibliography

[1] Fort, J. & Pujol, T. 2008 Progress in front propagation research. *Rep Prog Phys* 71, 086001.

[2] Fisher, R. A. 1937 The wave of advance of advantageous genes. *Ann Eugen* 7**,** 355-369.

[3] Skellman, J. G. 1951 Random dispersal in theoretical populations. *Biometrika* 38, 196-218.

[4] Steele, J. 2009 Human dispersals: Mathematical models and the archaeological record. *Hum Biol* 81, 121-140.

[5] Bailey, N. T. J. 1975 *The Mathematical Theory of Infectious Diseases,* 2nd ed. London: Griffin.

[6] Traqui, P. 2009 Biophysical models of tumor growth. *Rep Prog Phys* 72, 056701.

[7] Merikoski, J., Maunuksela, J., Myllys, M., Timonen, J. & Alava, M. J. 2003 Temporal and spatial persistence of combustion fronts in paper. *Phys Rev Lett* 90, 024501.

[8] Di Bartolo, S. J. & Dorsey, A. T. 1996 Velocity Selection for Propagating Fronts in Superconductors. *Phys Rev Lett* 77, 4442-4445.

[9] Fort, J. & Méndez, V. 1999 Time-delayed theory of the Neolithic transition in Europe. *Phys Rev Lett* 82, 867-870.

[10] Fort, J. & Méndez, V. 2002 Time-delayed spread of viruses in growing plaques. *Phys Rev Lett* 89, 178101.

[11] Fedotov, S. & Iomin, A. 2007 Migration and proliferation dichotomy in tumor cell invasion. *Phys Rev Lett* 98, 118101.

[12] Clark, J. S. 1998 Why trees migrate so fast: confronting theory with dispersal biology and the paleorecord. *Am Nat* 152, 204-220.

[13] Clark, J. S., Fastie, C., Hurtt, G., Jackson, S. T., Johnson et al. 1998 Reid's paradox of rapid plant migration. *BioScience* 48, 13-24.

[14] Reid, C. 1899 The origin of the British flora. London: Dulau.

[15] Fort, J. 2007 Fronts from complex two-dimensional dispersal kernels: Theory and application to Reid's paradox. *J Appl Phys* 101, 094701.

[16] Nathan, R., Schurr, F. M., Spiegel, O., Steinitz, O., Trakhtenbrot, A. et al. 2008 Mechanisms of long-distance seed dispersal. *Trends Ecol Evol* 23, 638-641.

[17] Willson, M. F. 1993 Dispersal mode, seed shadows, and colonization patterns. *Vegetatio* 107/108, 261-280.

[18] Nathan, R., Katul, G. G., Horn, H. S., Thomas, S. M., Oren, R. et al. 2002 Mechanisms of long-distance dispersal of seeds by wind *Nature* 418, 409-413.

[19] Neubert, M. & Caswell, H. 2000 Demography and dispersal: calculation and sensitivity analysis of invasion speed for structured populations. *Ecology* 81, 1613-1628.

[20] Ortega-Cejas, V., Fort, J., Méndez, V. & Campos, D. 2004 Approximate solution to the speed of spreading viruses. *Phys Rev E Stat Nonlin Soft Matter Phys* 69, 031909.

[21] Fort, J., Pérez-Losada, J., Ubeda, E. & García, J. 2006 Fronts with continuous waiting-time distributions: Theory and application to virus infections. *Phys Rev E Stat Nonlin Soft Matter Phys* 73, 021907.

[22] Yin, J. & McCaskill, J. S. 1992 Replication of viruses in a growing plaque: a reaction-diffusion model. *Biophys. J.* 61, 1540-1549.

[23] Haseltine, L., Lam, V., Yin, J. & Rawlings, J. B. 2008 Image-guided modeling of virus growth and spread. *Bull. Math. Biol.* 70, 1730-1748.

[24] Childe, V. G. 1925 *The Dawn of European Civilization.* London: Kegan, Paul, Trench & Trubner.

[25] Childe, V. G. 1942 *What happened in history.* Harmondsworth (UK): Penguin-books.

[26] Ammerman, A. J. & Cavalli-Sforza, L. L. 1971 Measuring the rate of spread of early farming in Europe. *Man (NS)* 6, 674-688.

[27] Ammerman, A. J. & Cavalli-Sforza, L. L. 1973 A population model for the diffusion of early farming in Europe. In *The explanation of culture change* (ed C. Renfrew), pp. 343-357. London: Duckworth.

[28] Ammerman, A. J. & Cavalli-Sforza, L. L. 1984 *The Neolithic transition and the genetics of populations in Europe.* Princeton (NJ): Princeton University Press.

[29] Vlad, M. O. & Ross, J. 2002 Systematic derivation of reaction-diffusion equations with distributed delays and relations to fractional reaction-diffusion equations and hyperbolic transport equations: Application to the theory of Neolithic transition. *Phys Rev E Stat Nonlin Soft Matter Phys* 66, 061908.

[30] Isern, N., Fort, J. & Pérez-Losada, J. 2008 Realistic dispersion kernels applied to cohabitation reaction–dispersion equations. *J Stat Mech: Theor Exp* 2008(10), P10012.

[31] Fedotov, S., Moss, D. & Campos, D.2008 Stochastic model for population migration and the growth of human settlements during the Neolithic transition. *Phys Rev E Stat Nonlin Soft Matter Phys* 78, 026107.

[32] Pinhasi, R., Fort, J. & Ammerman, A. J. 2005 Tracing the Origin and Spread of Agriculture in Europe. *PLoS Biol* 3, e410.

[33] Isern, N. 2011 *Front spreading in population dynamics models. Theory and application to the Neolithic transition.* Ph. D. Dissertation, University of Girona.

[34] Kropotkin, P. 1902 *Mutual aid: A factor of evolution.* New York: McClure Phillips & Co.

[35] Hamilton, W. D. 1964 Genetical evolution of social behavior I and II. *J Theor Biol* 7, 1-52.

[36] Maynard Smith, J. & Price, G. 1973 The logic of animal conflict. *Nature* 246, 15-18.

[37] Axelrod, R. & Hamilton, W. D. 1981 The evolution of cooperation. *Science* 211, 1390-1396.

[38] Perc, M. & Szolnoki, A. 2010 Coevolutionary games - A mini review. *Biosystems* 99, 109.

[39] Nowak, M. A. & May, R. M. 1992 Evolutionary games and spatial chaos. *Nature* 359, 826-829.

[40] Traulsen, A. & Nowak, M. A. 2006 Evolution of cooperation by multilevel selection. *Proc Nat Ac Sci USA* 103, 10952-10955.

[41] Nowak, M. A. & Sigmund, K. 1998 Evolution of indirect reciprocity. *Nature* 437, 1291-1298.

[42] Sigmund, K. 2007 Punish or perish? Retaliation and collaboration among humans. *Trends Ecol Evol* 22**,** 593.

[43] Isern, N. & Fort, J. 2009 Time-delayed reaction-diffusion fronts. *Phys Rev E* 80, 057103.

[44] Meloni, S., Buscarino, A., Fortuna, L., Frasca, M., Gómez-Gardeñes, J. et al. 2009 Effects of mobility in a population of prisoner's dilemma players. *Phys Rev E Stat Nonlin Soft Matter Phys* 79, 067101.

[45] Herrmann, B., Thöni, C. &. Gächter, S. 2008 Antisocial punishment across societies. *Science* 319, 1362-1367.

[46] Beck, D. E. 1990 Liriodendron Tulipifera L. In *Silvics of North America* (eds. R. M. Burns & B. H. Honkala), Agriculture Handbook 654, Vol. 2, pp. 406-416. Washington, DC: USDA, Forest Service.

[47] Harrington, A., Brodie, L. S., DeBell, D. S. & Schopmeyer C. S. 2008 Alnus P. Mill. In *The Woody Plant Seed Manual,* (eds. F. T. Bonner & R. P. Karrfalt). Agriculture Handbook 727, pp 232-242. Washington, DC: USDA, Forest Service.

[48] Nathan, R. 2001 The challenges of studying dispersal. *Trends Ecol Evol* 16, 481-483.

[49] Birks, H. J. B. 1989 Holocene isochrone maps and patterns of tree-spreading in the British Isles. *J Biogeography* 16**,** 503-540.

[50] Davis, M. B. 1976. Pleistocene biogeography of temperate deciduous forests. *Geoscience and Man* 13, 13-26.

[51] Huntley, B. & Birks, H. J. B. 1983. *An atlas of past and present pollen maps for Europe 0-13,000 years ago.* Cambridge: Cambridge University Press.

[52] Delcourt, P. A., & Delcourt, H. R. 1987. *Long-term forest dynamics of the temperate zone.* New York: Springer.

[53] MacDonald, G. M. 1993. Fossil pollen analysis and the reconstruction of plant invasions. *Advances in Ecological Research* 24, 67-110

[54] Stollar, D. & Levine, L. 1949 Two-Dimensional Immunodiffusion *Methods Enzymol* 6, 848-854.

[55] Ware, B. R., Raj, T., Flygare, W. H., Lesnaw, J. A. & Reichmann, M. E. 1973 Molecular weights of vesicular stomatitis virus and its defective particles by laser light-scattering spectroscopy. *J Virol* 11, 141-145.

[56] Yin, J. 1993 Evolution of Bacteriophage T7 in a Growing Plaque. *J Bacteriol* 175, 1272-1277.

[57] Shishido, K., Watarai, A., Naito, S. & Ando, T. 1975 Action of Bleomycin on the bacteriophage T7 infection. *J Antibiot (Tokio)* 28, 676-680.

[58] Lam, V., Duca, K. A. & Yin, J. 2005 Arrested Spread of Vesicular Stomatitis Virus Infections In Vitro Depends on Interferon-Mediated Antiviral Activity. *Biotech Bioeng* 90, 793-804.

[59] Delbrück, M. 1946 Bacterial viruses or bacteriophages. *Biol Rev Proc Cambridge Philos Soc* 21, 30-40.

[60] Stauder, J. 1971 *The Majangir: Ecology and Society of a Southwest Ethiopian People.* Cambridge: Cambridge University Press.

[61] Fort, J., Jana, D. & Humet, J. 2004 Multidelayed random walks: Theory and application to the neolithic transition in Europe. *Phys Rev E Stat Nonlin Soft Matter Phys* 70, 031913.

[62] Fort, J. & Méndez, V. 2002 Wavefronts in time-delayed reaction-diffusion systems. Theory and comparison to experiment. *Rep Prog Phys* 65, 895-954.

[63] Fort, J., Pérez-Losada, J., Suñol, J. J., Escoda, L. & Massaneda, J. M. 2008 Integro-difference equations for interacting species and the Neolithic transition. *New J. Phys.* 10, 043045.

[64] Méndez, V., Fort, J. & Farjas, J. 1999 Speed of wave-front solutions to hyperbolic reaction-diffusion equations. *Phys Rev E Stat Nonlin Soft Matter Phys* 60, 5231-5243

[65] Press,W. H., Teukolsky, S.A., Vetterling,W. T. & Flannery, B.P. 1992 *FORTRAN numerical recipes*, 2nd ed. Cambridge: Cambridge University Press.

[66] Murray, J. D. 2002 *Mathematical Biology*, 3rd ed. Berlin: Springer-Verlag.

[67] Dreber, A., Rand, D. G., Fudenberg, D. & Nowak, M. A. 2008 Winners don't punish. *Nature* 452, 348-351.

[68] Rand, D. G., Dreber, A., Ellingsen, T., Fudenberg, D. & Nowak, M. A. 2009 *Science* 325, 1272-1275.

[69] Egas, M. & Riedl, A. 2008 The economics of altruistic punishment and the maintenance of cooperation. *Proc R Soc B* 275, 871-878.

[70] Henrich, J., McElreath, R., Barr, A., Ensminger, J., Barrett, C. et al. 2006 Costly punishment across human societies. *Science* 312, 1767-1770.

[71] Fehr, E. & Gächter, S. 2002 Altruistic punishment in humans. *Nature* 415, 137-140.

[72] Gintis, H., Bowles, S., Boyd, R. & Fehr, E. 2003 Explaining altruistic behavior in humans. *Evol Hum Behav* 24, 153-172.

[73] van Saarloos, W. 2003 Front propagation into unstable states. *Phys. Rep.* 386, 29-222.

[74] Vladimirova, N. & Rosner, R. 2003 Model flames in the Boussinesq limit: The effects of feedback. *Phys. Rev. E* 67, 066305.

[75] Pujol, T., Fort, J., González, J. R., Montoro, L. & Pelegrí, M. 2008 Bounds for the speed of combustion flames: effect of mass diffusion. *Physica A* 387, 1987-1998.

[76] Caswell, H. 1989 *Matrix Population Models.* Sunderland: Sinauer.

[77] Van den Bosch, F., Metz, J. A. J. & Diekmann, O. 1990 The velocity of spatial population expansion. *J. Math. Biol.* 28, 529-565.

[78] Mollison, D. 1991 Dependence of epidemic and population velocities on basic parameters. *Math. Biosci.* 107, 255-287.

[79] Lui, R. 1982 A Nonlinear Integral Operator Arising from a Model in Population Genetics I. Monotone Initial Data. *SIAM J. Math. Anal.* 13, 913-937.

[80] Lui, R. 1982 A Nonlinear Integral Operator Arising from a Model in Population Genetics II. Initial Data with Compact Support. *SIAM J. Math. Anal.* 13, 938-953.

[81] Hosono, Y. 1995 Travelling Waves for a Diffusive Lotka-Volterra Competition Model II: A Geometric Approach. *Forma* 10, 235-257.

[82] Hosono, Y. 1998 The minimal speed of traveling fronts for a diffusive Lotka-Volterra competition model. *Bull. Math. Biol.* 60**,** 435-448.

[83] Fort, J., Pérez-Losada, J. & Isern, N. 2007 Fronts from integro-difference equations and persistence effects on the Neolithic. *Phys. Rev. E* 76**,** 031913.

[84] Weinberger, H. F. 1978 Asymptotic behavior of a model in population genetics. In *Nonlinear Partial Differential Equations and Applications (*ed J. Chadam), pp. 47-96. Berlin: Springer.

[85] Caswell, H., Lensink, R. & Neubert, M. 2003 Demography and dispersal: life table response experiments for invasion speed. *Ecology* 84, 1968-1978.

[86] Horn, R.A. & Johnson, C. R. 1985 *Matrix Analysis.* Cambridge (UK): Cambridge University Press.

[87] Müller, J. 1998 Optimal Vaccination Patterns in Age-Structured Populations. *SIAM J. Appl. Math.* 59, 222-241.

[88] Müller, J., Schönfisch, B., & Kirkilionis, M. 2000 Ring vaccination *J. Math. Biol.* 41, 143-171.

[89] Müller, J., Kretzschmar, M. & Dietz, K. 2000 Contact tracing in stochastic and deterministic epidemic models. *Math. Biosci.* 164, 39-64.

[90] Huerta, R. & Tsimring, L. S. 2002 Contact tracing and epidemics control in social networks. *Phys. Rev. E* 66**,** 056115.

[91] Tsimring, L. S. & Huerta, R. 2003 Modeling of contact tracing in social networks *Physica A* 325, 33-39.

[92] Fort, J. 2002 A comment on amplification and spread of viruses in a growing plaque. *J. Theor. Biol.* 214, 515-518.

[93] Brown, S. P., Cornell, S. J., Sheppard, M., Grant, A.J., Maskell, D.J. et al. 2006 Intracellular Demography and the Dynamics of Salmonella enterica Infections. *PLoS Biol.* 4, e349.

[94] Abedon, S. T. & Culler, R. C. 2007 Bacteriophage evolution given spatial constraint. *J. Theor. Biol.* 248, 111-119.

[95] Los, J. M., Golec, P., Wegrzyn, G., Wegrzyn, A. & Los, M. 2008 Simple Method for Plating Escherichia coli Bacteriophages Forming Very Small Plaques or No Plaques under Standard Conditions. *Appl. Environ. Microbiol.* 74, 5113-5120.

[96] Kaliniene, L., Klausa, V. & Truncaite, L. 2010 Low-temperature T4-like coliphages vB_EcoM-VR5, vB_EcoM-VR7 and vB_EcoM-VR20. *Arch. Virol.* 155, 871-880.

[97] Jou, D., Casas-Vázquez, J. & Lebon, G. 1996 *Extended Irreversible Thermodynamics.* Berlin:Springer-Verlag.

[98] Ebert, U. & Van Saarloos, W. 2000 Front propagation into unstable states: universal algebraic convergence towards uniformly translating pulled fronts. *Physica D* 146, 1-99.

[99] You, L. & Yin, J. 1999 Amplification and spread of viruses in a growing plaque. *J. Theor. Biol.* 200, 365-373.

[100] Ackermann, H. W. 1976 Classification of tailed enterobacteria phages. *Pathol. Biol. (Paris)* 24, 359.

[101] Draper, N. R. & Smith, H. 1981 *Applied Regression Analysis,* 2nd. ed. New York: Wiley.

[102] Amor, D. R. & Fort, J. 2010 Virus infection speeds: Theory versus experiment. *Phys. Rev. E* 82, 061905.

[103] Birdsell, J. B. 1957 Some Population Problems Involving Pleistocene Man. *Cold Spring Harb. Symp. Quant. Biol.* 22, 47-69.

[104] Roberts, D. F. 1968 Genetic Effects of Population Size Reduction. *Nature* 220, 1084-1088.

[105] Lotka, A. J. 1956 *Elements of mathematical biology,*pp. 64-69. New York: Dover.

[106] Amor, D. R. & Fort, J. 2009 Fronts from two-dimensional dispersal kernels: Beyond the nonoverlapping-generations model. *Phys. Rev. E* 80, 051918.

[107] Buckley, Y. M., Brockerhoff, E., Langer, L., Ledgard, N., North, H., et al. 2005 Slowing down a pine invasion despite uncertainty in demography and dispersal. *J Appl Ecol* 42, 1020-1030.

[108] Clark, J. S., Lewis, M. & Horvath, L. Invasion by extremes: population spread with variation in dispersal and reproduction. *Am. Nat.* 157, 537-554.

[109] Galenko, P. K. & Danilov, D. 2000 Selection of the dynamically stable regime of rapid solidification front motion in an isothermal binary alloy. *J. Cryst. Growth.* 216, 512-536.

[110] Kashiwagi, T., McGrattan, K. B., Olson, S. L., Fujita, O., Kikuchi, M. et al. 1996 Effects of Slow Wind on Localized Radiative Ignition and Transition to Flame Spread in Microgravity. In: *26th Symposium (Int.) on Combustion,* Vol. 1, pp 1345-1352. Pittsburgh: The Combustion Institute.

[111] Haseltine, L., Lam, V., Yin, J. & Rawlings, J. B. 2008 Image-Guided Modeling of Virus Growth and Spread. *Bull. Math. Biol.* 70, 1730-1748.

[112] De Steven, D. 1991 Experiments on mechanisms of tree establishment in old-field succession: seedling survival and growth. *Ecology* 72, 1076-1088.

[113] Nowak, M. A. 2006 *Evolutionary Dynamics.* Cambridge (MA):Harvard University Press.

[114] Szabó, G. & Fáth, G. 2007 Evolutionary games on graphs. *Phys. Rep.* 446, 97-216.

[115] Roca, C. P., Cuesta, J. A. & Sánchez, A. 2009 Effect of spatial structure on the evolution of cooperation. *Phys. Rev. E* 80, 046106.

[116] Helbing, D., Szolnoki, A., Perc, M. & Szabó, G. 2010 Punish, but not too hard: how costly punishment spreads in the spatial public goods game. *New J. Phys.* 12, 083005.

[117] Ule, A., Schram, A., Riedl, A. & Cason, T. N. 2009 Indirect Punishment and Generosity Toward Strangers. *Science* 326, 1701-1704.

[118] Li, X. & Cao, L. 2009 Largest Laplacian eigenvalue predicts the emergence of costly punishment in the evolutionary ultimatum game on networks. *Phys. Rev. E* 80, 066101.

[119] Traulsen, A., Semmann, D., Sommerfeld, R. D., Krambeck, H. & Milinski, M. 2010 Human strategy updating in evolutionary games. *Proc. Natl. Sci. U.S.A.* 107, 2962-2966.

[120] Rockenbach, B. & Milinski, M. 2006 The efficient interaction of indirect reciprocity and costly punishment. Nature 444, 718-723.

[121] Nowak, M. A. 2006 Five Rules for the Evolution of Cooperation. *Science* 314, 1560-1563.

[122] Hauert, C. 2001 Fundamental clusters in spatial 2×2 games. *Proc. R. Soc. Lond., Ser. B* 268, 761-769.

[123] Pacheco, J. M., Traulsen, A. & Nowak, M. A. 2006 Coevolution of Strategy and Structure in Complex Networks with Dynamical Linking *Phys. Rev. Lett.* 97, 258103.

[124] Helbing, D. & Yu, W. 2009 The outbreak of cooperation among success-driven individuals under noisy conditions. *Proc. Natl. Sci. U.S.A.* 106, 3680-3685.

[125] Van Segbroeck, S., Santos, F. C., Lenaerts, T. & Pacheco, J. M. 2009 Reacting Differently to Adverse Ties Promotes Cooperation in Social Networks. *Phys. Rev. Lett.* 102, 058105.

[126] Killingback, T., Doebeli, M. & Knowlton, N. M. 1999 Variable investment, the Continuous Prisoner's Dilemma, and the origin of cooperation. *Proc. R. Soc. Lond., Ser. B* 266, 1723-1728.

[127] Fu, F., Wu, T. & Wang, L. 2009 Partner switching stabilizes cooperation in coevolutionary prisoner's dilemma. *Phys. Rev. E* 79, 036101.

[128] Yang, H. X., Wu, Z. X. & Wang, B. H. 2010 Role of aspiration-induced migration in cooperation. *Phys. Rev. E* 81, 065101.

[129] Aktipis, C. A. 2004 Know when to walk away: contingent movement and the evolution of cooperation. *J. Theor. Biol.* 231, 249-260.

[130] Vainstein, M. H., Silva, A. T. C. & Arenzon, J. J. 2007 Does mobility decrease cooperation? *J. Theor. Biol.* 244, 722-728.

[131] Jiang, L. L., Wang, W. X., Lai, Y. C. & Wang, B. H. 2010 Role of adaptive migration in promoting cooperation in spatial games. *Phys. Rev. E* 81, 036108.

[132] Srivastava, V., Neel, J., Mackenzie, A. B., Menon, R., DaSilva, L. A. et al. 2005 Using game theory to analyze wireless ad hoc networks. *IEEE Commun. Surv. Tutorials* 7, 46-56.

[133] Boyd, R., Gintis, H., Bowles, S. & Richerson, P. J. 2003 The evolution of altruistic punishment *Proc. Natl. Sci. U.S.A.* 100, 3531-3535.

[134] Colman, A. M. 2006 The puzzle of cooperation. *Nature* 440, 744-745.

[135] Gintis, H., Bowles, S., Boyd, R. & Fehr, E. (eds) 2005 *Moral Sentiments and Material Interests: The Foundations of Cooperation in Economic Life.* Cambridge (MA): MIT Press.

[136] Milinski, M. & Rockenbach, B. 2008 Human behaviour: Punisher pays. *Nature* 452, 297-298.

[137] Szolnoki, A., Szabó, G. & Perc, M. 2011 Phase diagrams for the spatial public goods game with pool punishment. *Phys. Rev. E* 83, 036101.

[138] Andreoni, J., Harbaugh, W. & Vesterlund, L. 2003 The Carrot or the Stick: Rewards, Punishments, and Cooperation. *Am. Econ. Rev.* 93, 893-902.

[139] Szolnoki, A. & Perc, M. 2010 Reward and cooperation in the spatial public goods game. *Europhys. Lett.* 92, 38003.

[140] Hilbe, C. & Sigmund, K. 2010 Incentives and opportunism: from the carrot to the stick. *Proc. R. Soc. B* 277, 2427-2433.

[141] Gächter, S. & Herrmann, B. 2009 Reciprocity, culture and human cooperation: previous insights and a new cross-cultural experiment. *Phil. Trans. R. Soc. B* 364, 791-806.

[142] Boyd, R., Gintis, H. & Bowles, S. 2010 Coordinated Punishment of Defectors Sustains Cooperation and Can Proliferate When Rare. *Science* 328, 617-620.

[143] Helbing, D., Szolnoki, A., Perc, M. & Szabó, G. 2010 Defector-accelerated cooperativeness and punishment in public goods games with mutations. *Phys. Rev. E* 81, 057104.

[144] Helbing, D., Szolnoki, A., Perc, M. & Szabó, G. 2010 Evolutionary Establishment of Moral and Double Moral Standards through Spatial Interactions. *PLoS Comput. Biol.* 6, e1000758.

[145] Hammerstein, P. (ed) 2003 *Genetic and Cultural Evolution of Cooperation.* Cambridge (MA):MIT Press.

[146] Fehr, E. & Gächter, S. 1992 Reciprocity and economics: The economic implications of Homo Reciprocans. *Eur. Econ. Rev.* 42, 845-859.

[147] Wu, J., Zhang, B., Zhou, Z., He, Q., Zheng, X. et al. 2009 Costly punishment does not always increase cooperation. *Proc. Natl. Sci. U.S.A* 106, 17448-17451.

[148] Dall, J. & Christensen, M. 2002 Random geometric graphs. *Phys. Rev E* 66, 016121.